博士論文

Gas-permeable organic electrochemical transistor used as on-skin active electrode

(皮膚上のアクティブ電極として利用される通気性のある有機電気化学トランジスタ)

令和３年６月１日　提出

指導教員：染谷隆夫　教授

東京大学大学院工学系研究科

電気系工学専攻

３７－１８７１８４

王嘉斌

Table of contents

Abstract

Daily-life health monitoring using comfortable on-skin electronics is highly demanded for improving the quality of life. Using high-performance on-skin electrodes to acquire high-quality signals can improve the stability and accuracy of health monitoring. This study developed the gas-permeable organic electrochemical transistor (OECT) as on-skin active electrodes for acquiring and simultaneously amplifying the electrophysiological signals. The gas-permeability of the electrodes eliminated the risk of irritation to the skin caused by the accumulation of moisture between the sensor and skin. The superior electrical characteristics of the OECT were utilized to acquire high-quality signals. The fibrous organic nanomesh formed by electrospinning was used as the substrate for fabricating the gas-permeable nanomesh organic electrochemical transistor (NMOECT). Gas-permeable porous solid-state polymer electrolyte (SPE) was developed to be embedded with the NMOECT.

This study firstly developed the active elements onto the ultra-soft nanomesh substrate. The NMOECT used as on-skin active electrodes to locally amplify the electrocardiographic signal was demonstrated. The superior electrical characteristics of the NMOECT enable it to acquire high-quality signals with higher amplitude and smaller output resistance was achieved. This research expanded the function of the ultra-soft nanomesh electronics, also making the OECT applicable for continuously wearing on-skin.

All details of the development of the gas-permeable OECTs are discussed in this thesis, including the fabrication process, electrical characterization, numerical model, and the application as an on-skin active electrode.

Chapter 1: Introduction and purpose of this research

1.1 Gas-permeable on-skin electronics for health monitoring

The demand for relieving the pain of healthcare and improving quality of life is growing quickly[1, 2]. Using the non- or low invasive methods/devices to monitor health conditions in daily life is the most effective way to get the early disease warning and help people be informed about the body condition[3-8]. Skin is a suitable candidate to non-invasively acquire body information[2, 9]. There is a lot of human body information can be acquired from the skin surface, including the electric[10], physic[11-13], and chemical signals[2, 14, 15], as shown in Figure 1[1]. These signals can reflect the inside body's activities. On-skin electronics is an emerging technology that aims at developing flexible electronics that can conformably be wear on the skin surface and monitoring the body signals harmoniously.

Figure 1. On-skin physiological signals that can be used for daily life health monitoring. (Copied from the reference[1])

In recent years, the development of sensors is advancing a lot by incorporating the advances of materials, mechanical, and electronics. A lot of on-skin sensors with novel functions and better comfortability have been invented, as shown in Figure 2[2]. These efforts are trying to build smart skin that can monitor health conditions and improve the quality of life of human beings.

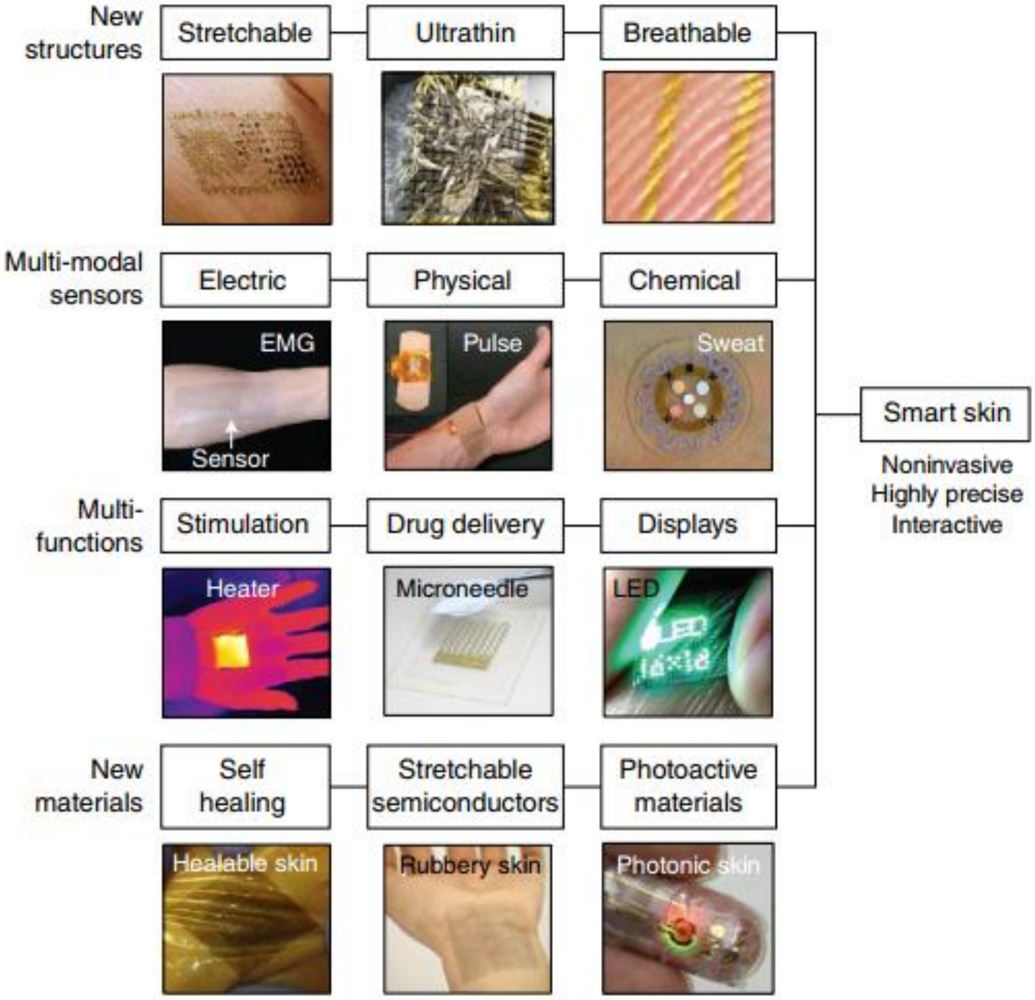

Figure 2. The research progress of the skin electronics. (Copied from the reference[2])

Among the signals from the skin surface, the electric signals are very informative to know the health condition or inside-body activities [16-18]. For example, the electrocardiographic (ECG) signal acquired from the skin is used to know the health condition of the heart, which is the most widely used heart monitoring or disease diagnosis method[18]. The electrophysiological signals can be loaded to the recording equipment by the electrodes that are attached to the skin surface. The electrophysiological signals from the skin surface are very weak with a tiny amplitude of less than

1 mV and a high output impedance of more than hundreds kilo-ohm[19]. The signals can be easily affected by noise such as environmental electromagnetic or motion artifact[19]. One method to reduce the output impedance of the signal is using relatively larger electrodes that increase the contact area with the skin[20], since the impedance is inversely proportional to the contact area. On the other hand, stable contact between the electrodes and skin can reduce the noise that comes from the motion artifact, which can also improve the signal quality[9, 19]. Conformal contact between the electrodes and skin can not only increase the contact area but also maintain a stable contact between electrode and skin, which is the advantage of using ultra-thin on-skin electrodes for signal acquiring[3, 6].

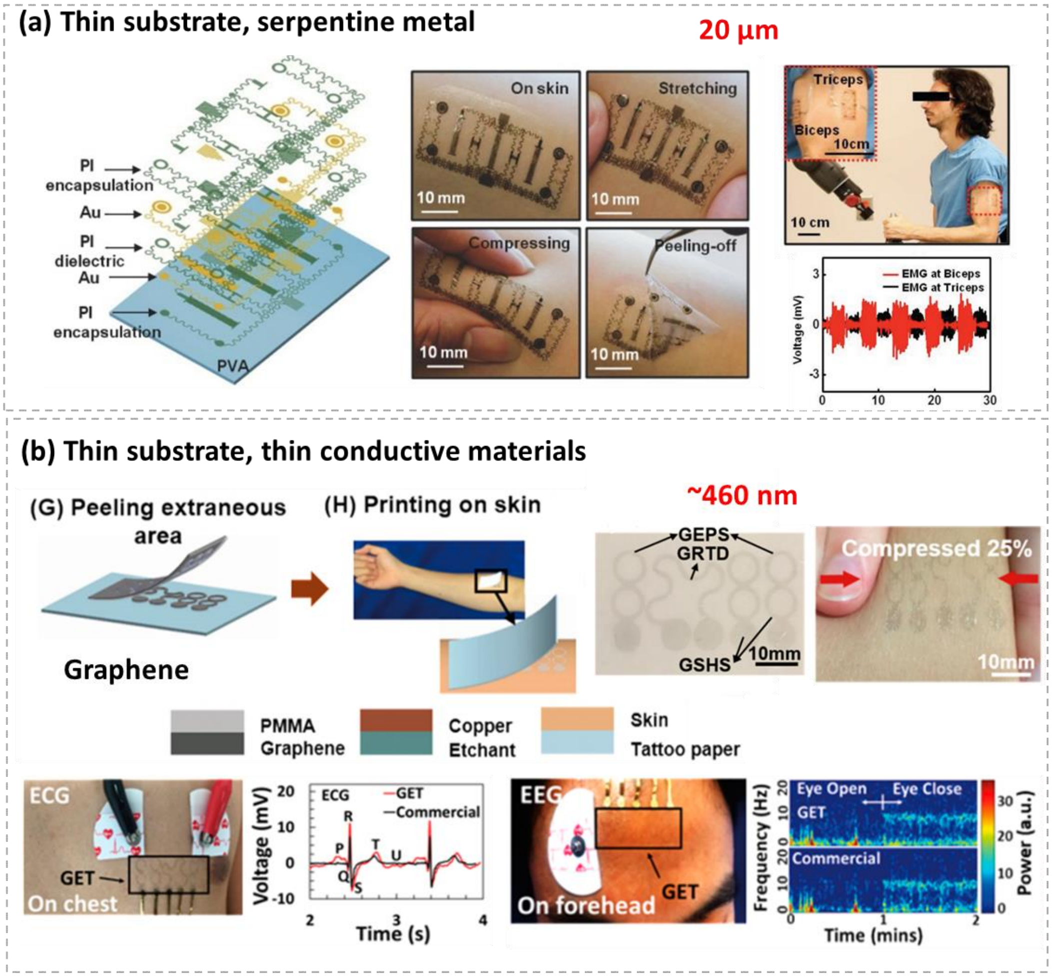

Figure 3 Strategies of making ultrathin and flexible on-skin electrodes. (a) Serpentine metal fabricated on thin substrate (copied from reference[21]). (b) Ultra-thin graphene based electrodes (copied from reference[22]).

The main strategy to achieve better conformability is decreasing the thickness of the electrodes. Researchers demonstrated that the electrodes with a thickness less than 10 μm can achieve a stable contact with the skin[23], which eliminates the mismatch between skin during the motion. A conformable contact between the electrodes and skin also increases the contacting area between with skin, which also reduces the contact impedance of the electrodes, rendering the improvement of signal quality. As shown in Figure 3(a), the ultra-thin electrodes are conformably laminated onto the skin surface, high-quality EMG signals are acquired and utilized to control the robots[21]. Much thinner materials, such as graphene was also used, as shown in Figure 3(b), which makes the electrodes even thinner and transparent, and highly reduces the influence to the normal daily activities[22].

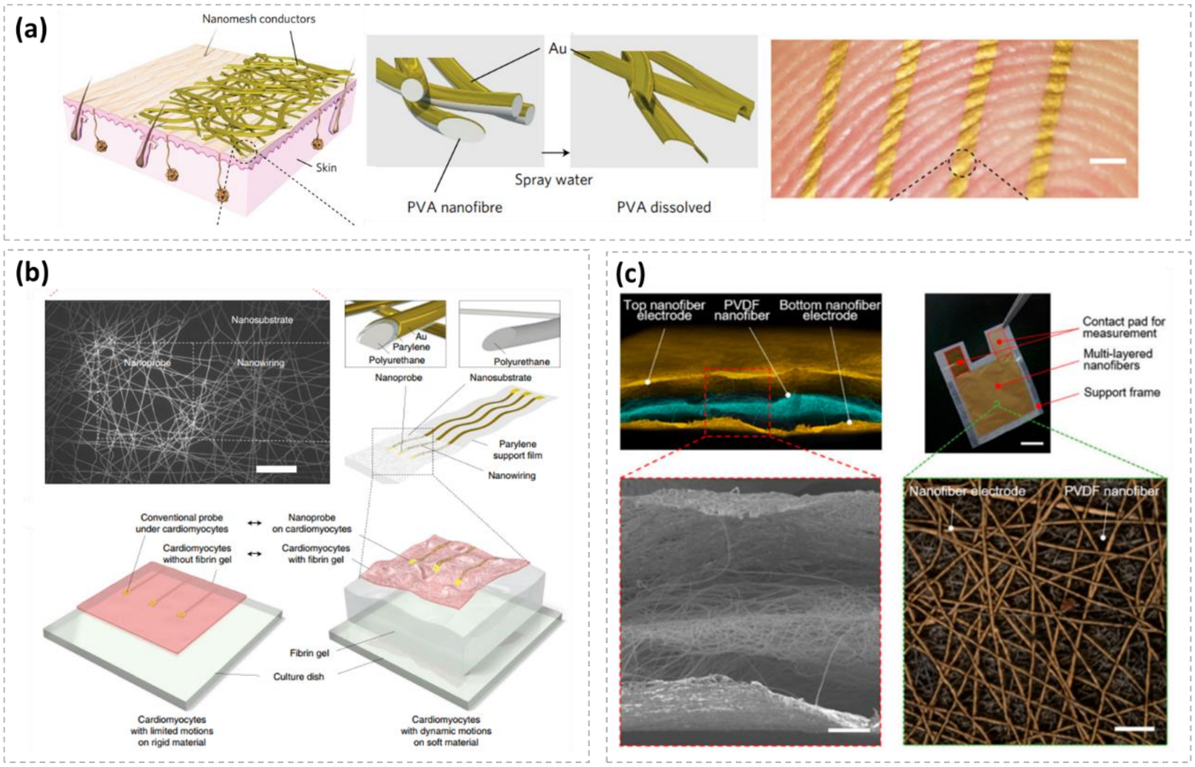

Figure 4 Gas-permeable on-skin electronics in nanomesh structure. (a) On skin nanomesh gas-permeable conductors (copied from reference [20]). (b) Nanomesh electrodes as in-vivo electrophysiological sensors (copied from reference[24]). (c) Nanomesh acoustic sensor for continuous on-skin heart sound monitoring (copied from reference[25]).

While a lot of researches are focusing on developing novel functional device on the ultra-thin substrate, and multi-modal signal acquisition from skin surface have been achieved, another important requirement of on-skin electronics is being concerned, which is the gas-permeability. The on-skin electronics are designed for long-term and continuous health monitoring. However, lack of gas-permeability will irritate the skin due to the accumulation of sweat between the skin and the electronic devices[26].

There are several structures of device structures to achieve the porous electronics enabling the gas-permeability, such as sponge-like polymer[27], fibrous network[20], and laser-etched film[27]. In recent years, ultrathin fibrous nanomesh on-skin electronics have been proposed to solve the gas-permeability issue[20]. The nanomesh is a fibrous network structure with thickness in hundreds of nanometers. Its porous structure allows the penetration of sweat while being used as on-skin electrodes. This kind of nanomesh structure is a very promising approach for practical on-skin electronics. Various nanomesh on-skin sensors have been developed, including electrophysiological electrodes[24], strain sensors[20], pressure sensors [28], and acoustic sensors [25]. Figure 4 shows the schematics and device structure of these gas-permeable nanomesh devices. The devices were fabricated using electro-spun fibrous polymers. The devices are substrate-free or the fibers are directly used as the substrate, rendering the gas-permeable structure of the devices.

1.2 Active on-skin electrophysiological electrodes

Although ultra-thin, gas-permeable on-skin electrophysiological electrodes have been developed to build a very good interface between the electrode and the skin, the improvement of the signal quality is limited. In the practical application, a pre-stage amplifier is usually used to further reduce the output impedance and improve the amplitude of the acquired signals[29], as shown in Figure 5(a). After the pre amplifier, the signal contains less output impedance, which can be easily processed by the following components, such as using filters to cut the signals that are not needed for health monitoring. Also, the signals after the amplifier have higher power, which can be strong enough against the influence of noise[30].

To further improve the quality of acquired signals, the active electrodes were proposed[31]. The on-skin electrophysiological electrodes integrated with the amplifying elements are called active electrodes. By using the active electrodes, the acquired signal can be immediately amplified before loading to the recording equipment, as shown in Figure 5(a). The active electrodes can acquire high-quality signals, which can be easily recorded and processed.

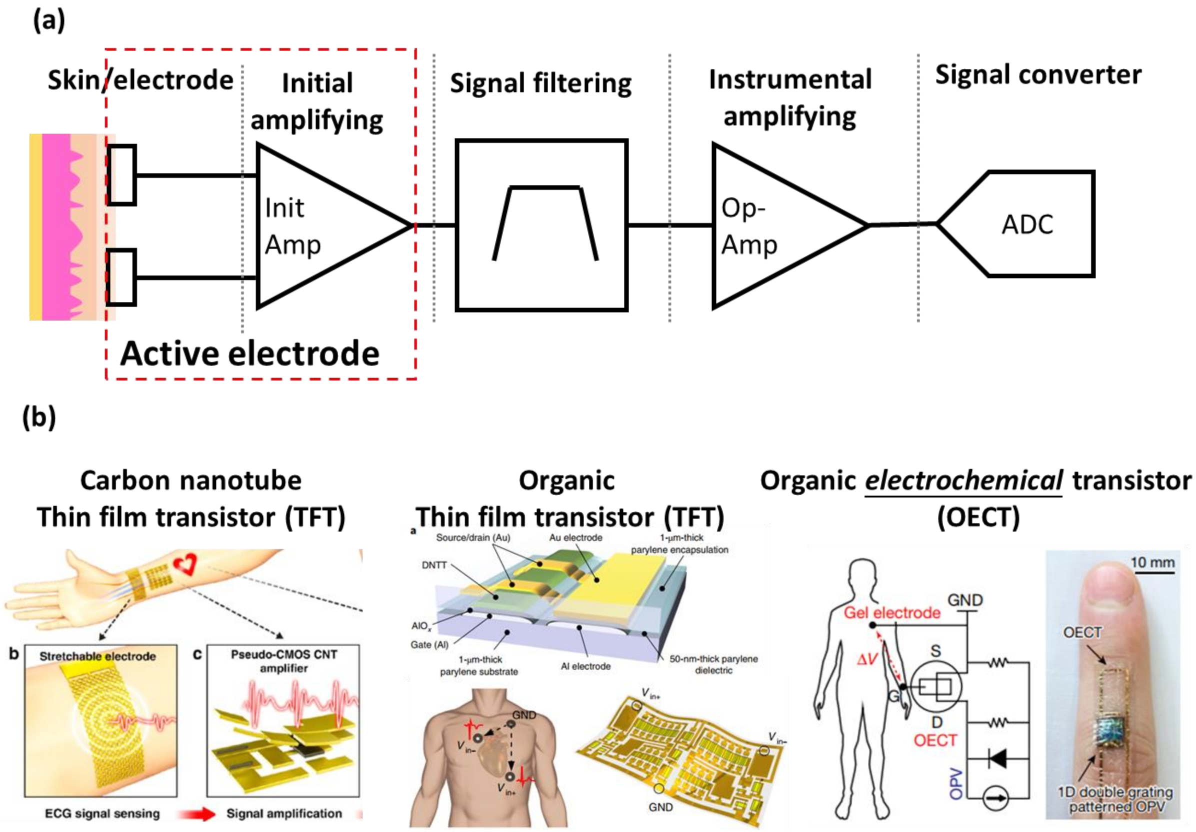

Figure 5 (a) The schematic of an electrophysiological signal acquisition elements. (b) The active electrodes using CNT-TFT (copied from reference[32]), OTFT (copied from reference[33]), and OECT (copied from reference[34]), respectively.

To achieve comfortable on-skin active electrodes, active elements such as transistors should be flexible, so a good interface between skin can be formed. With the development of flexible electronics technologies, many ultra-thin flexible transistors technologies have been implemented for active electrophysiological electrodes. The representative flexible transistor technologies include carbon nanotube-based thin-film transistor (CNT-TFT)[32, 35-37], organic thin-film transistor (OFTF)[33, 38, 39], and organic electrochemical transistor (OECT)[40-42], as shown in Figure 5(b). A comparison of the basic electric characteristics of these technologies is shown in Table 1. Among these technologies, the OECT utilizing electrochemical effect to achieve signal-transducing, shows extremely high transconductance ($g_m = \Delta V_G/\Delta I_D$) and low working voltage, besides, the OECT shows an easy fabrication process, rendering the OECT a promising candidate for the future on-skin active electrode.

Table 1. The comparison between the flexible transistor technologies.

	CNT-TFT [32]	**OTFT**[33]	**OECT**[43]
Semiconductor	CNT	DNTT	**PEDOT:PSS**
Mechanism	***Field effect***	***Field effect***	***Electrochemical***
Size	W:300 µm	W:10 µm	W:10 µm
	L: 10 µm	L: 1 µm	L: 5 µm
$\mathbf{V_D}$	-5V	-2 V	**-0.6 V**
$\mathbf{g_m = \Delta I_D / \Delta V_G}$	17.1 µS	12 µS	**2700 µS**
$\mathbf{g_m / \lvert V_D \rvert}$	3.42 µS/V	95 µS/V	**4500 µS/V**
Gas-permeability	**No**	**No**	**No**

As discussed in the above section, gas-permeability is essential for on-skin electronics. However, all the reported on-skin active electrodes are in film-type structure without gas-permeability, which could cause the inflammation of skin irritated by the accumulation of sweat. One challenge is that the fabrication of the transistors into the irregular structure might cause significant degradation to the device performance[44, 45]. On the other hand, the transistor fabrication process might not be compatible with the ultra-thin and soft substrate, which will damage the soft structure. Developing the gas-permeable soft active electrodes is still facing the problem.

1.3 Organic electrochemical transistor (OECT) as active electrophysiological electrodes

OECTs are mostly developed as electrophysiological sensors[16, 34, 40, 41, 46-48] and chemical sensors[49-54]. OECT has a similar structure as the conventional field-effect transistor (FET), with gate, drain, and source electrodes[55]. The gate and channel of OECT are coupled by electrolyte, which does not need the precise control of the thickness of the dielectric layer, improving the yield of device fabrication, and the robustness against mechanic deformation is also excellent. The most widely used channel materials for the OECT is poly(3,4-ethylenedioxythiophene) polystyrene sulfonate (PEDOT: PSS), which is a kind of semi-transparent p-type conductive polymer material. The chemical structure and illustration of the PEDOT:PSS chains are shown in Figure 6. The sulfonate anions of the PSS couple with the PEDOT, generating holes in the PEDOT. The generated holes make the PEDOT: PSS system conductive. The PEDOT: PSS is in very high conductance, usually used as a conductive layer for organic electronic devices [56, 57], or directly used as on-skin electrodes[34, 41, 58]. The anions of the PSS allow the doping of cations from the electrolyte, and the conductance decreased accordingly, enabling the PEDOT:PSS semi-conductive materials.

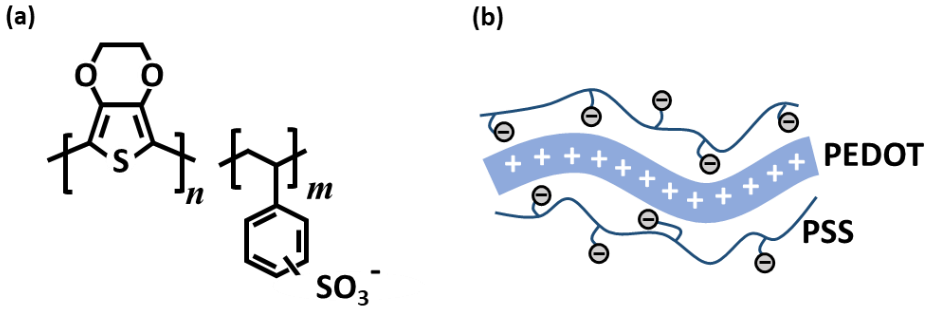

Figure 6. (a) Chemical structure of the PEDOT:PSS. (b) Illustration of the PEDOT:PSS chains.

A typical structure of the OECT is shown in Figure 7. The voltage signal from the gate electrode can control the movement of cations in the electrolyte. When a negative gate voltage was applied to the gate electrode, cations decoupled with PSS anions, and the holes in the PEDOT backbone increased, which made PEDOT more conductive, as shown in Figure 7(b). When a positive gate voltage was applied to the gate electrode, cations were injected and coupled with PSS anions, then the holes in the PEDOT backbone decreased, which made PEDOT less conductive, as shown in Figure 7(c). So, the change of gate voltage ΔV_G can change the conductivity of PEDOT:PSS channel. With a bias voltage V_D , the change of drain current ΔI_D can be observed.

The movement of the ions in the electrolyte can be controlled by a small voltage, so the OECT can work in a small voltage range. Besides, the doping of PEDOT: PSS happens in the whole polymer layer, rendering high controllability of the gate voltage. Another important advantage of the OECT over the FET is the independence on the thickness of the dielectric layer, which makes the fabrication of OECT easier. Usually, the high-performance FET relies on the thin dielectric layer to enhance the control of the gate[59]. However, the thin dielectric layer is easily broken during mechanical deformation. OECT can use much thick electrolyte that is stable and robust, rendering OECT durable against mechanical deformation.

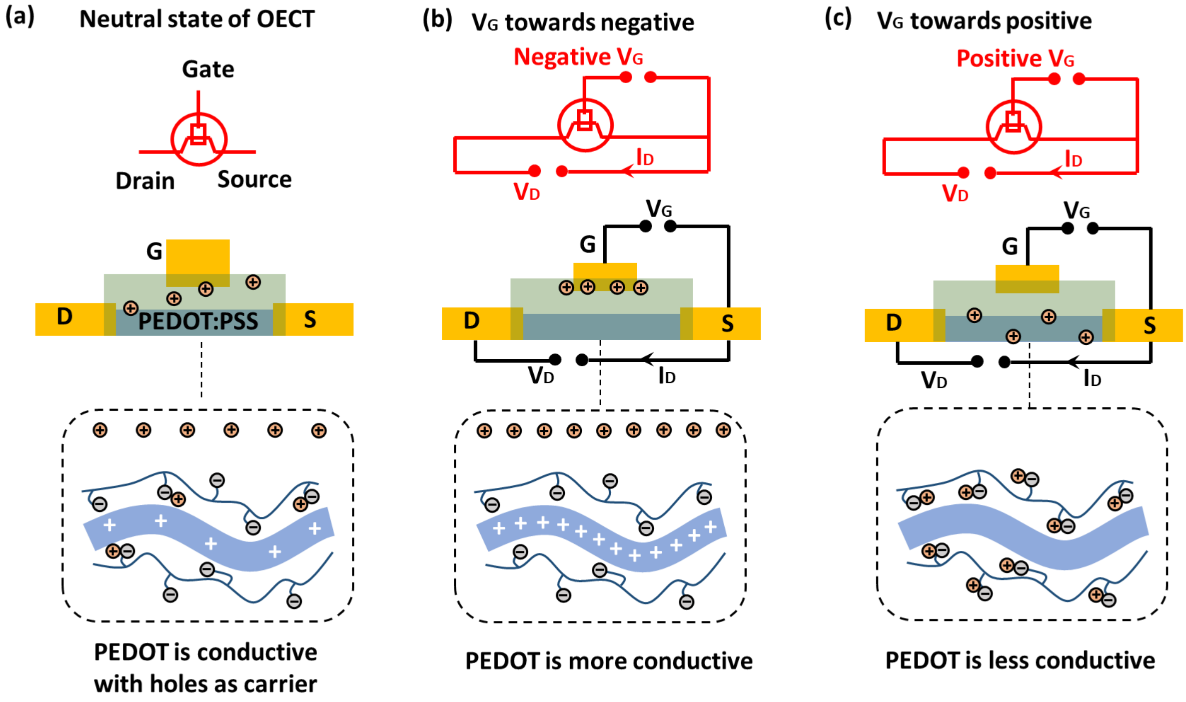

Figure 7. (a) Typical structure of an OECT device with a gate electrode, the cations in the electrolyte will couple with anions in PSS and decrease density of holes in PEDOT backbone. (b) The PEDOT:PSS becomes more conductive when a negative gate voltage is applied. (c) The PEDOT:PSS becomes less conductive when a positive voltage is applied.

The response time of OECT usually in the microsecond to millisecond range, which is in kilo hertz range in the frequency domain, and could be used in the bio signal range. Biological electrophysiological signals are usually in the hundreds hertz range [16]. The response of OECT is fast enough for acquiring the full waveform of the electrophysiological signals. Utilizing the OECT to amplify various electrophysiological signals has been demonstrated, such as electrooculography (EOG)[41], electroencephalogram (EEG)[48], and electrocardiogram (ECG)[34]. The output impedance of the signals significantly reduced after the amplification.

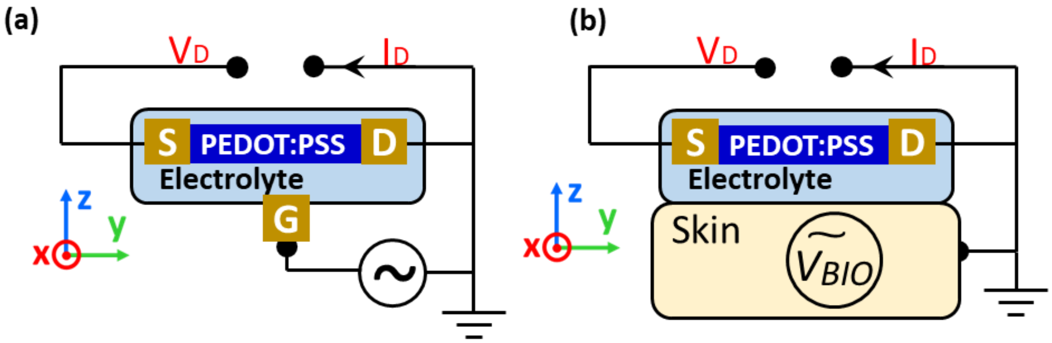

Figure 8. (a) Schematic of OECT. (b) Using the OECT as on-skin active electrode.

Figure 8 shows a schematic of using the OECT as the on-skin active electrophysiological electrode. In this case, the gate electrode is not used, instead, the bio tissue or human skin are directly coupled to the channel of OECT by the electrolyte, as shown in Figure 8(b). The potential change on the tissue's surface controls the doping of ions into the PEDOT: PSS channel; the electrophysiological signals are simultaneously acquired and amplified. High-quality signals can be read. The output resistance of the signal is decided by the resistance of the OECT channel. OECT is especially suitable for implanted in vivo measuring, where the fluids in the tissue can be used as an electrolyte to support the function of OECT. For the on-skin applications, the solid-state polymer electrolyte is needed to avoid the dysfunction caused by the dry of liquid electrolyte. However, the gas-permeable OECT for on-skin application has not been developed before this study.

1.4 Purpose of this research

The purpose of this research is to develop gas-permeable on-skin active electrodes, to simultaneously acquire and locally amplify the electrophysiological signals, enabling high-quality signal acquisition using ultra-soft and comfortable on-skin electrodes. The approach will make the recording of high-quality electrophysiological signals easier and more comfortable.

The conventional device fabrication processes are not compatible with the ultra-thin, flexible, and gas-permeable substrates. Exploring the novel approach for device fabrication, including the materials deposition, patterning, and characterization is needed. Understanding the difference between devices in gas-permeable structure and in film structure is also essential. These methods are meaningful for the future development of on-skin electronics. Besides, the proper design of signal processing circuits is needed to coordinate the signals with existing signal recording equipment.

The superior electrical characteristics of OECT is utilized to develop high-performance on-skin active electrode. The method to fabricate the OECT into the gas-permeable structure was investigated. Besides, the gas-permeable solid-state polymer electrolyte was developed to be embedded with the OECT for the on-skin application. The converting and processing of the signal acquired by the OECT were also investigated for practical applications.

This thesis is organized as follows:

In Chapter 1, the background of the on-skin gas-permeable electrodes and the active electrodes for electrophysiological signal acquiring are presented and discussed. The basic knowledge of the OECT is also introduced.

In Chapter 2, the development of the fibrous nanomesh organic electrochemical transistor (NMOECT) was discussed. The process of fabricating the device on the ultra-thin nanomesh substrate was discussed. The spray coating was utilized to coat the PEDOT:PSS polymer as the channel of the NMOECT. The thickness of the PEDOT:PSS could be controlled to several hundreds of nanometers. The process was optimized to maintain the gas-permeability of the nanomesh substrate. The steady-state and dynamic electrical performance of the NMOECT were characterized. We demonstrated the NMOECT is robust against mechanical bending, rendering it suitable for the on-skin application. The model used to better fit the electrical characteristics of the NMOECT was also proposed.

In Chapter 3, the demonstration of using the NMOECT as the on-skin electrocardiographic (ECG) electrode was investigated. The setup to make the signal read by NMOECT readable by the conventional equipment was designed. The ECG signals read by NMOECT electrodes were presented and analyzed. The amplifying characteristics of the NMOECT with various supply voltages and loading resistors were characterized. The locally amplified electrocardiography (ECG) signals acquired by the NMOECT electrodes were demonstrated, and analog filters were utilized to cut the DC voltage in amplified signals for the first time. The high signal-to-noise ratio (SNR) of 25.896 dB was achieved in the ECG signals acquired by the NMOECT. A feasible setup for wireless reading the electrophysiological signals acquired by the NMOECT was also proposed.

In Chapter 4, the porous chitosan-based electrolyte was developed to be embedded with the NMOECT, to make the gas-permeable electrolyte embedded OECT. The natural polymer chitosan-based porous SPE was developed using the freezing dry process. The composition of the SPE was optimized. We discussed the development of the fabrication process to form the porous structure of the SPE and the NMOECT embedded with the porous SPE, enabling the gas-permeability on-skin active electrodes. The composition of the porous SPE was optimized to form the porous structure, at the same time maintaining sufficient ion conductivity. The porous SPE embedded NMOECT fully utilizes the high humidity environment of the skin surface to achieve sufficient response speed for ECG signal acquiring.

In Chapter 5, we summarized the main achievement of this research and discussed the prospect of the research on the gas-permeable on-skin active electrodes. The possible approaches to further improve the performance of the on-skin active electrodes were proposed.

Chapter 2: Nanomesh organic electrochemical transistor (NMOECT)

As discussed in the last chapter, the conventional OECT consists of channel part (drain/source, and polymer channel), gate electrodes, and electrolyte. For on-skin application, the skin can be regarded as the gate. When the channel part is connected to the skin and loaded with electrolyte, the potential change on the skin surface can be recorded by measuring the current change in the channel with a drain voltage, as shown in Figure 8(b). The channel part of the OECT and the electrolyte form an on-skin electrode. In this study, we proposed fabricating the channel parts of OECT onto the fibrous nanomesh substrate, which allows the gas-permeability of the OECT. This chapter will discuss the details about the NMOECT, including the fabrication process, the basic electrical characterization, and the stability against mechanic deformation. In this chapter, the liquid electrolyte was used for device characterization. In chapter 4, the study of the gas-permeable solid-state polymer electrolyte will be discussed, which can be embedded with the NMOECT and be used as gas-permeable on-skin active electrodes.

2.1 Fabrication process of NMOECT

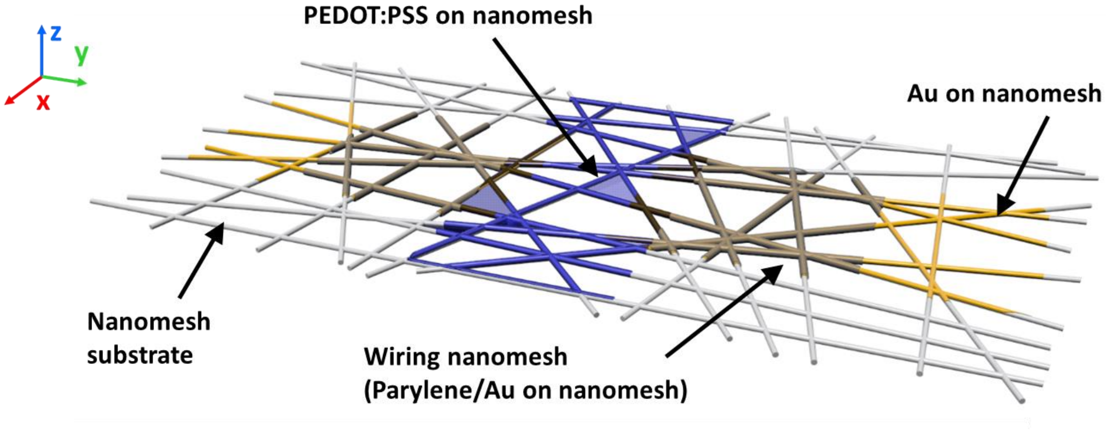

Figure 9. The conceptive schematic of the channel part of the NMOECT.

To fabricate the gas-permeable OECT electrode, the fibrous nanomesh substrate was implemented for device fabrication. The device structure was conceived as shown in Figure 9. In this structure, the Au was evaporated onto the nanomesh, forming a porous conductive fibrous nanomesh, being used as drain/source electrode. The parylene was coated onto parts of the Au, to encapsulate the Au and avoid the direct contact between electrolyte and conductive Au, which can reduce the leakage current. The PEDOT:PSS was coated onto the area between drain and source electrode, working as the channel of the NMOECT. The whole device is in a porous structure. The following parts will describe the details about the device fabrication.

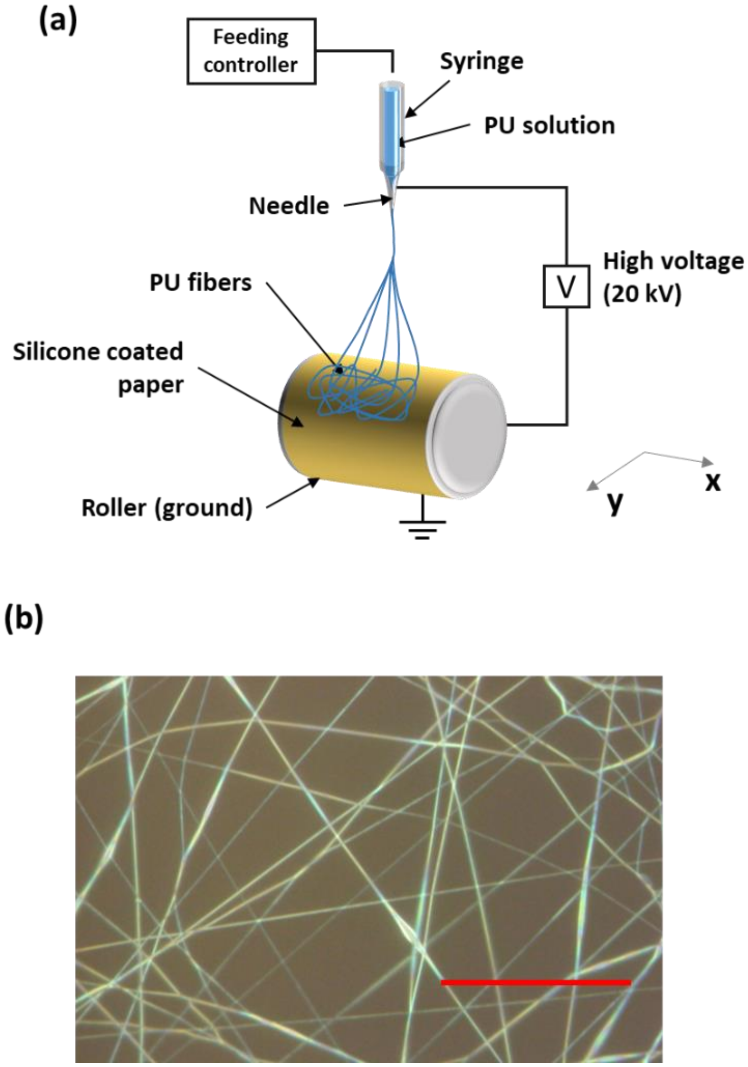

Figure 10. (a) Setup of an electrospinning equipment. (b) Optical image of the fabricated fibrous PU nanomesh. (scale bar: 30 μm)

First, the electrospinning was used to form the fibrous network sheet for device fabrication. The setup is illustrated in Figure 10(a). A 15% Polyurethane (PU) solution was made (Rezamin M-8115LP) with a solvent [N,N-dimethylformamide (DMF)/methyl ethyl ketone at a weight ratio of 7:3]. During electrospinning, the PU solution was placed in a syringe with a 27G needle, and a silicone-coated paper (TOYO ALUMINIUM EKCO PRODUCTS Co., Ltd.) was placed on the grounded counter electrode. A voltage of 20 kV was applied between the needle and the ground, then the PU fibers were formed and coated onto the silicone-coated paper. The feed rate of the syringe was 0.6 mL/h. The total electrospinning time was 4 min. After the process, a sheet of fibrous PU was formed on the surface of the silicone-coated paper. The optical image of the fabricated PU nanomesh is shown in Figure 10 (b).

The nanomesh is extremely soft and easily broken during the fabrication process. To temporarily holding the nanomesh, a 2 µm parylene on 125 µm polyimide (PI) frame was made and used as supporting film. The fabrication flow of the parylene/polyimide frame is shown in Figure 11 (a) to (c). A fluorescent layer of NOVEC was coated onto the PI film by spinning coating, which was used to reduce the adhesion between the PI film and the later coated parylene layer. Then the parylene layer was coated onto the PI film by chemical vapor deposition (CVD), which was used as the final support frame for manipulating the NMOECT. After that, an open window (5 mm x 4 mm) as shown in Figure 11 (c) was cut using a laser cutter. Later the PU fibrous sheet will be laminated onto the frame, forming a freestanding fibrous sheet on the open area.

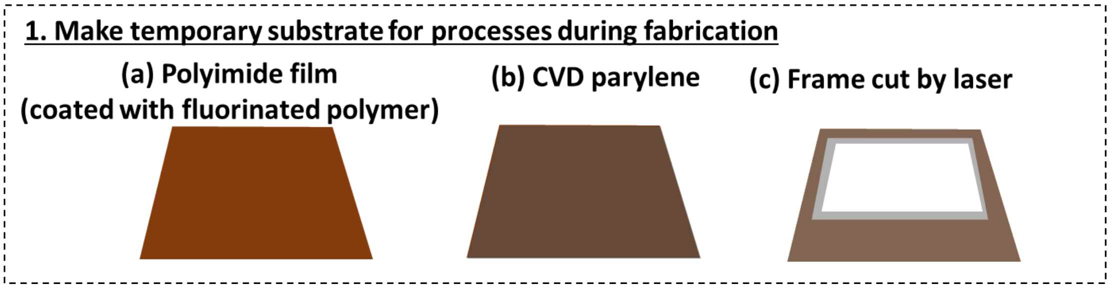

Figure 11. The process of making the supporting frame for device fabrication

Then, the PU fibrous sheet was coated onto the silicone-coated paper, using the electrospinning method as shown in Figure 10(a). The PU fibrous sheet can be easily peeled off from the silicone-coated paper.

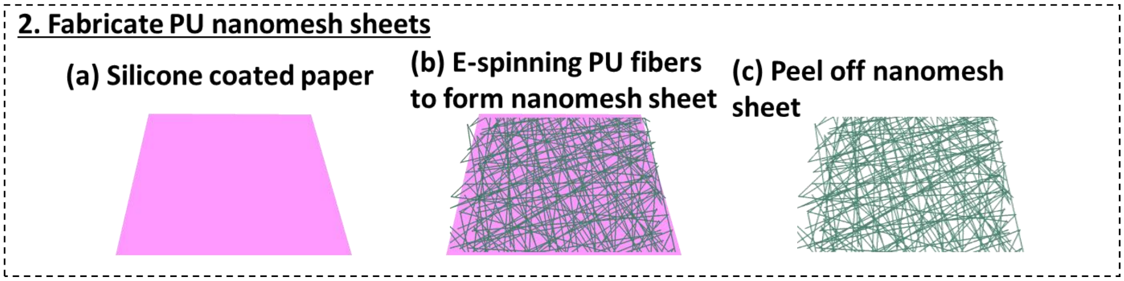

Figure 12. The process of making the fibrous PU sheet.

Next step, the peeled-off PU fibrous sheet was transferred to the frame that we made before. As shown in Figure 13 (a). To enhance the connecting junction between fibers, another 250-nm parylene was coated onto the nanomesh using chemical vapor depositing (CVD) system. The CVD can achieve the uniform coating of parylene around the fibers, as shown in Figure 13(b). Then the 100 nm Au drain/source electrodes and wires were coated by physical vapor deposition (PVD) and patterned by a shadow mask. The width and length of the transistor were designed to be 200 µm and 100 µm respectively. Then, to avoid the leakage current from the gate to the wires, a 250 nm parylene was coated by CVD as encapsulation. After that, the drain and source electrodes at the channel parts was exposed by reactive ion etch (RIE). Next, the channel polymer PEDOT: PSS was coated by the spray coating method. The coating of PEDOT:PSS will be discussed in the following parts. The fabrication steps are shown in Figure 13 (a) to (f).

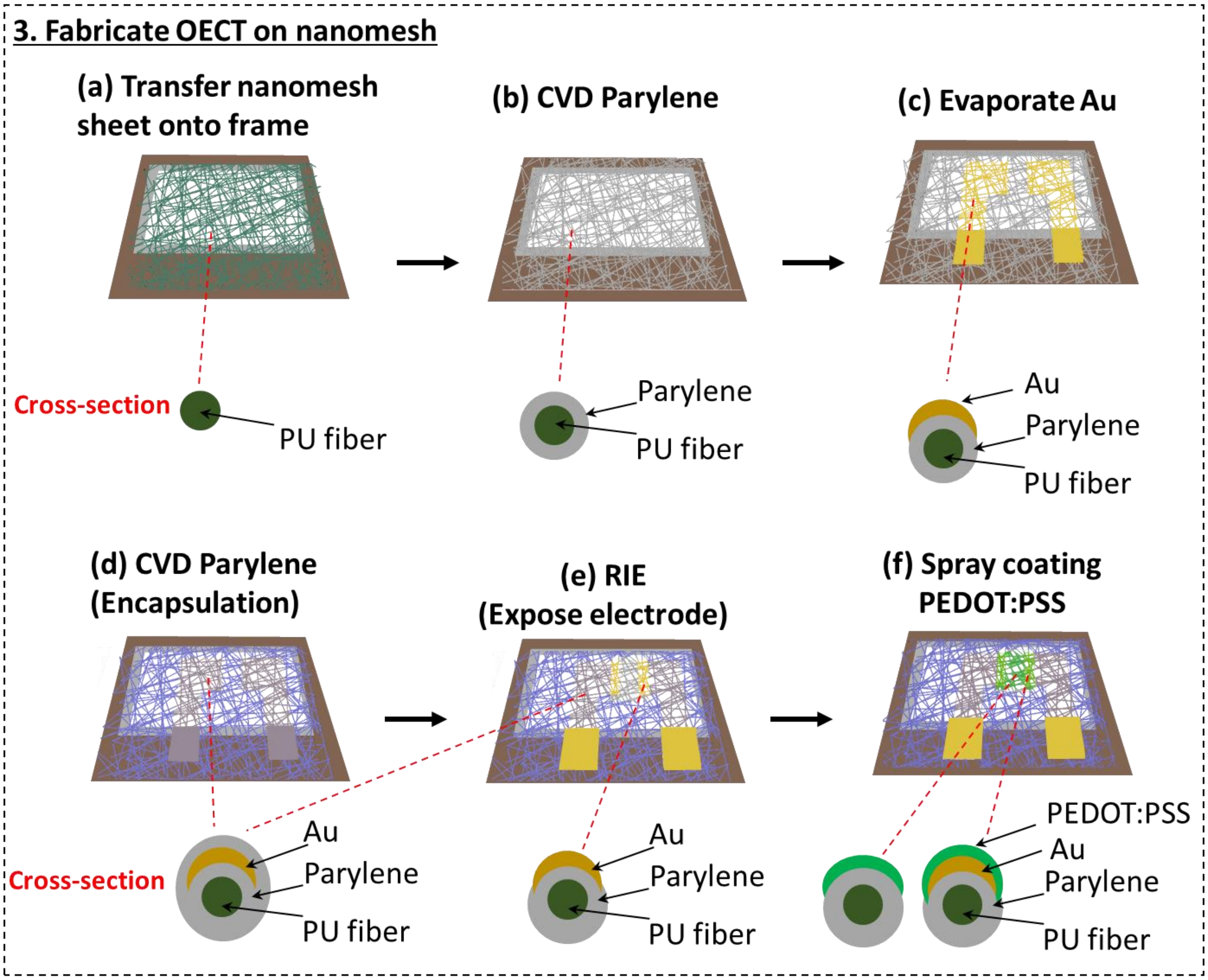

Figure 13. The process of fabricating the OECT on to the nanomesh substrate.

After the fabrication finished, the device was peeled off from the polyimide frame together with the 2 µm parylene, and the parylene was used as a supporting layer for the freestanding NMOECT. The thin parylene layer can release the mechanical mismatch between the nanomesh and the recording components of characterizing equipment, to avoid the damage of the NMOECT during the characterization, as shown in Figure 14.

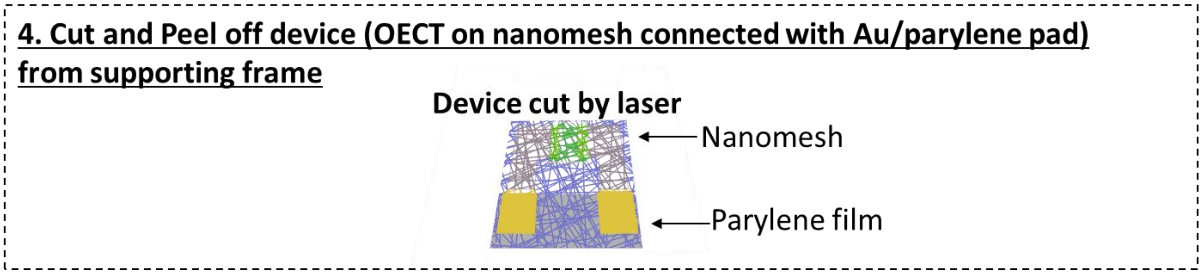

Figure 14. Peel off the NMOECT from the supporting frame.

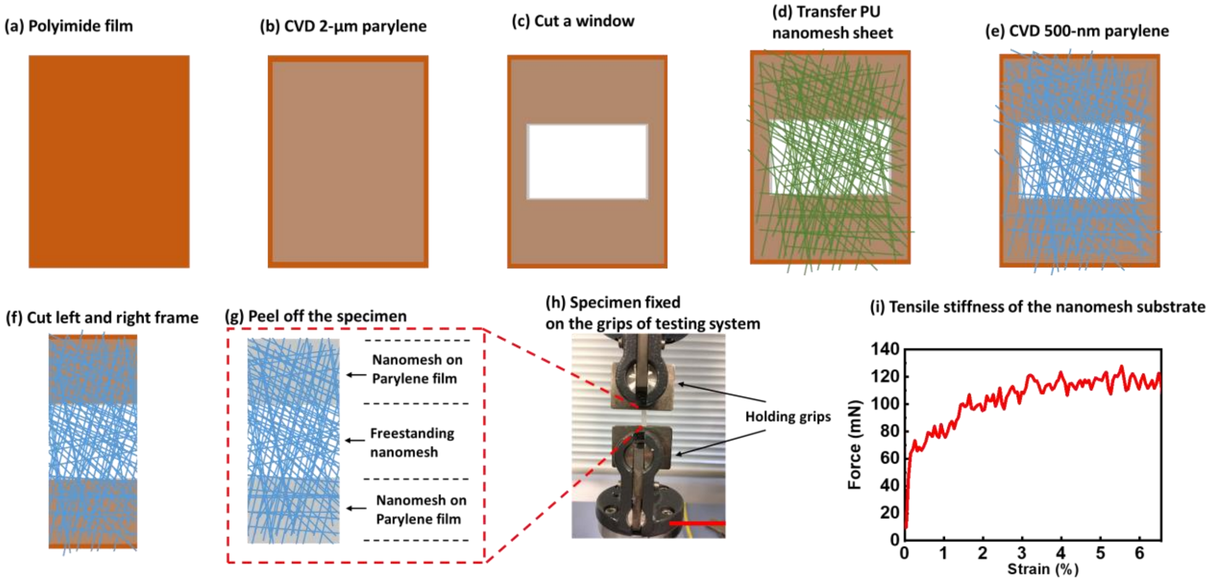

Figure 15. Specimen fabrication and tensile testing of the nanomesh substrate. (a) Polyimide (PI) film (125 µm) spincoated with a fluorinated polymer layer on top, as the supporting film, for easily holding during process. (b) Chemical vapor deposit (CVD) a 2-µm parylene film on the PI film. (c) Cut a window (5 mm x 3 mm) on the parylene/PI film using a laser, forming a window frame to make nanomesh freestanding. (d) Transfer the PU nanomesh onto the window frame. (e) Deposit 500-nm parylene on the PU nanomesh. (f) Cut the parylene/PI film. (g) Peel off the parylene from PI film, forming a freestanding nanomesh (3 mm x 3 mm) with two parylene film

holders on both sides. (h) The specimen is holding by grips of testing system, which extends the sample and measure the forces. (i) Results of the tensile testing.

The stiffness of the device was characterized by tensile testing. The experiment was performed in a high-precision mechanical system (AG-X, Shimazu) using a standard tensile testing method. The PU nanomesh was transferred to parylene (2 µm)/polyimide (125 µm) window frame film and then coated 500-nm parylene, identical with the nanomesh substrated used for the fabrication of NMOECT. Then the frame was cut and the parylene was peeled off to form the specimen for the test, as shown in Figure 15 (a) to (g). The schematic of the final specimen is shown in Figure 15(g), with two parylene films on the edges, between which is the nanomesh sample. Peeling of thin parylene window frame from polyimide film (125 µm) was done to avoid the damage caused by the mechanical mismatch between thin freestanding nanomesh (~1.2 µm) and the thicker polyimide film (125 µm). The two parylene films were fixed to the grips of the testing system. After that, the grips slowly extending the specimen, and the elongation (ΔL) between the grips was recorded against the applied force (Force) of the grips simultaneously, as shown in Figure 15 (h). The initial length of nanomesh was set to L_0, then the strain was calculated as $\frac{\Delta \mathrm{L}}{L_0}$. The tensile stiffness was plotted by Force versus strain, as shown in Figure 15(i).

Table 2. Comparison of PEDOT: PSS coating methods.

	Spin coating [60]	**Drop coating** [57]	**Spray coating** [60]
Thickness range	50 nm ~ 357 nm	~µm	***100 nm to ~µm***
Soft substrate	Difficult	Possible	***Possible***
Uniformity	Good	Limited	***Good***
Pattern method	Lift-off / Etch	Lift-off / Etch	***Shadow mask***

The PEDOT:PSS channel is the most important layer for the NMOECT. Properly control the coating of PEDOT:PSS is essential for controlling the performance of NMOECT and maintain the gas-permeable structure of nanomesh. As shown in Figure 16, without the proper control of PEDOT:PSS coating, the pores of the nanomesh will be blocked after coating, which eliminates the gas-permeability of the device, on the contrary with the target to make the gas-permeable NMOECT. Conventionally, for the film-type OECT, the spin coating is widely used, as it can coat a thin and uniform layer[60]. However, it cannot be used for depositing on the ultra-soft and gas-permeable nanomesh substrate. Here, the deposition of the PEDOT:PSS is going to be discussed.

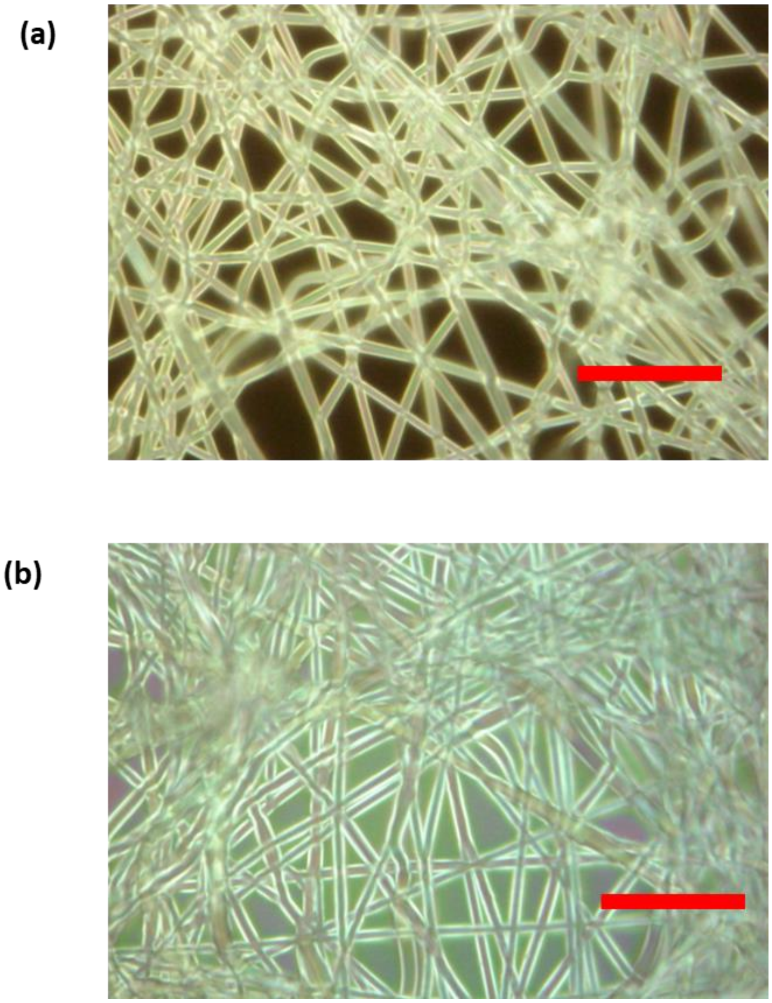

Figure 16. Coating of PEDOT:PSS on nanomesh without optimization. (a) The nanomesh substrate (scale bar: 20 µm). (b) The nanomesh after coated with PEDOT: PSS (scale bar: 20 µm).

Table 2 shows the typical coating method of PEDOT:PSS, including spin coating, drop coating and spray coating. The spinning coating is the most used method to coat the PEDOT:PSS for the fabrication of OECT[16, 47, 61]; a thin layer with a thickness of tens nanometers can be formed. However, the substrate should be uniform and smooth for coating high-quality film using spinning coating, which is not applicable for coating the PEDOT:PSS to the fibrous nanomesh substrate. Drop coating is easy and can coat the polymer materials to a broad type of substrate, but the drop coating is implemented to coat thick film with a thickness of hundreds of micrometers[57], which is too thick for the OECT operation. Thick PEDOT:PSS layer will block the pores of the nanoemsh, and also slow down the response of the OECT. In this study, the spray coating was picked to coat the PEDOT:PSS onto the nanomesh. The spray coating is suitable for coating materials on the irregular substrate and can deposit thin film with a thickness of hundreds of nanometer[60], and the patterning is also easier compare with the spin coating. The thin and small thickness of PEDOT:PSS layer can keep the porosity of the nanomesh, also it is essential to achieve high-speed OECT characteristics.

The following part will discuss the approaches to maintain the gas-permeable structure after coating the polymer materials. The electrical performance of the NMOECT after coated with PEDOT:PSS will also be discussed in the next section.

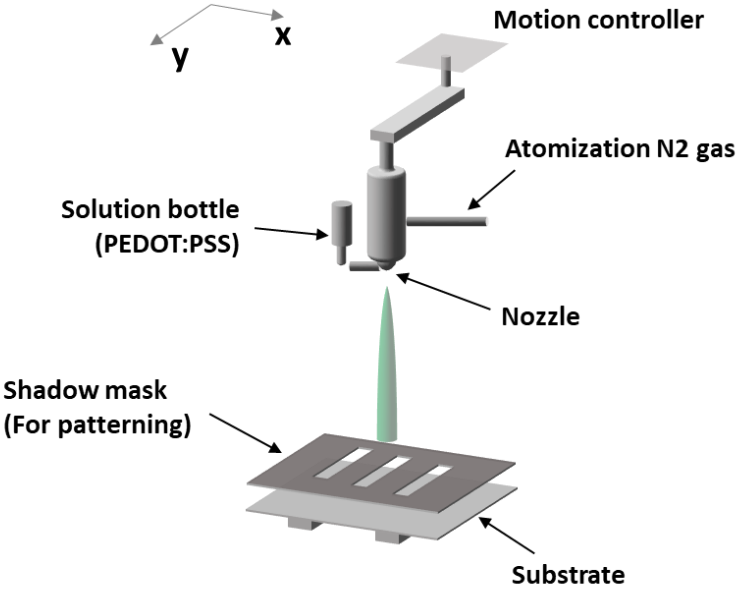

Figure 17. The schematic of the spray coating system.

A schematic of the spray coating system used in this study is shown in Figure 17. The atomized nitrogen gas was used to compress the PEDOT:PSS solution to be mist and eject from the nozzle at a high speed. The solution was split up to be a beam of solution spray and finally reach the substrate. The nanomesh with supporting frame was suspended by two 10 cm high holders underneath. During the coating process, the nozzle was moving in both the x-axis and y-axis direction with a speed of 200 mm/s. The coated solution was patterned by a shadow mask that defines the channel patterns. After coated with the solution, the sample was dried and annealed under 140 ℃ in the oven for 1 hour.

The thickness of the coated PEDOT: PSS was firstly characterized by using parylene coated glass as the substrate. We first optimized the movement speed of the nozzle, the pressure of the atomized gas, and the open area of the nozzle, to get a uniform layer. Then, the amount of PEDOT:PSS was controlled by controlling the spray coating cycles, which was increased with the increasing of coating cycles. The thickness is measured by the profiler. The resul is shown in Figure 18. The thickness can be varied from 80 nm to 500 nm for one-cycle coating to four-cycle coating respectively. The results reveal that the system can coat hundreds of nanometer level PEDOT:PSS film.

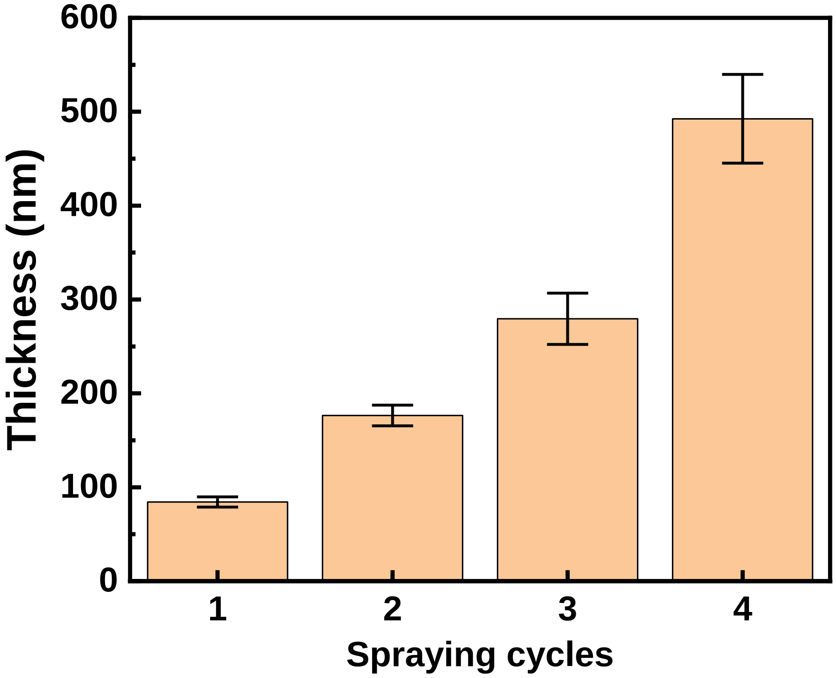

Figure 18. The thickness of PEDOT:PSS coated on parylene/glass with various coating cycles.

To maintain the gas permeability of the nanomesh after coating of the PEDOT:PSS. In this study, the fiber density of nanomesh and coated amount of PEDOT:PSS was optimized, to maintain the gas-permeable structure and keep the good electrical performance of the NMOECT.

Figure 19 shows results of coating PEDOT:PSS onto the high-density nanomesh and low-density nanomesh respectively. On the high-density nanomesh, most of the pores will be blocked, while on the low-density nanomesh, most pores can be maintained. To keep the gas-permeability of the NMOECT, low-density nanomesh was used in the fabrication.

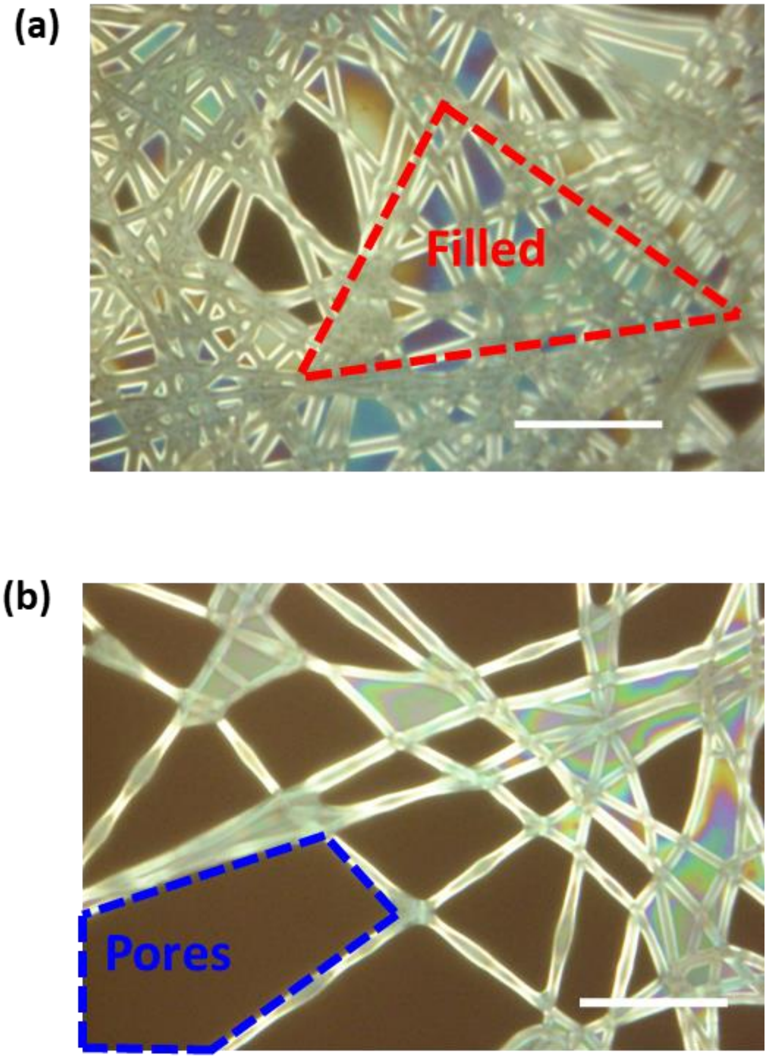

Figure 19. The PEDOT:PSS coated on to the nanomesh with (a) high fiber density and (b) low fiber density (scale bar: 20 μm).

Another optimization is the amount of coated PEDOT:PSS on the nanomesh. Even on the low-density nanomesh, coat a large amount of PEDOT:PSS will also result in the block of pores of the nanomesh, which reduces the gas-permeability of the device, as the result shown in Figure 20. The nanomesh coated with less PEDOT:PSS shows a better porous structure.

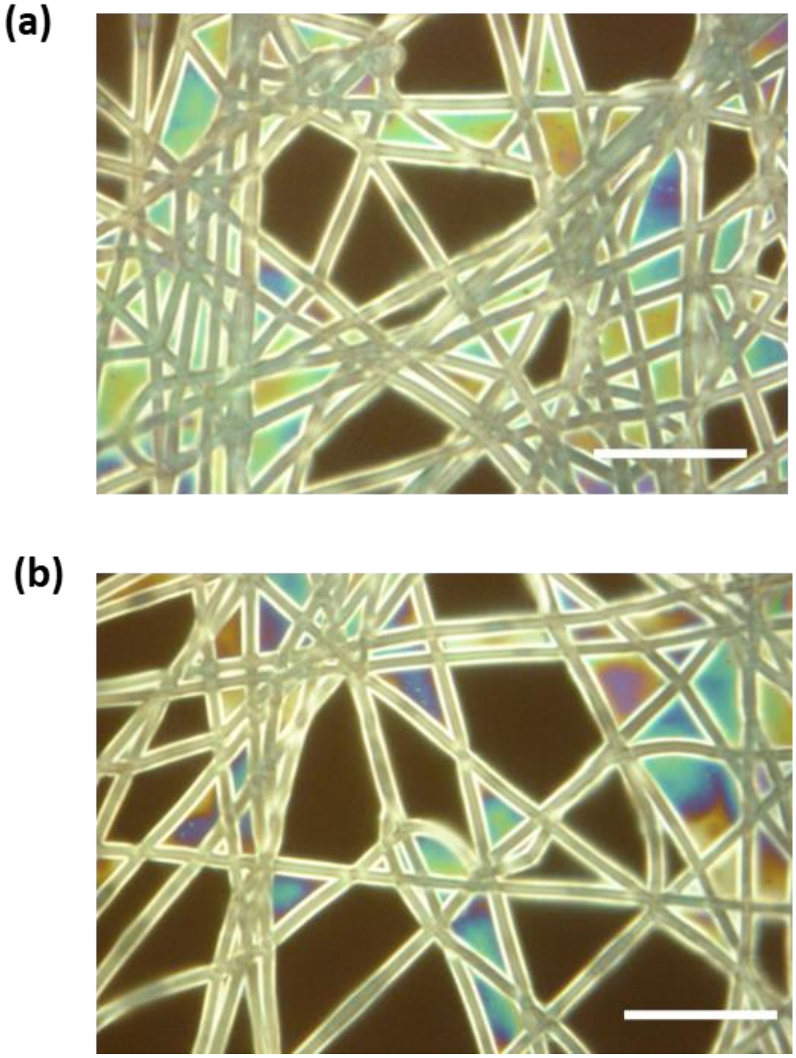

Figure 20. The PEDOT:PSS coated on to the nanomesh with different amount of PEDOT:PSS. (a) Four cycles spray coating. (b) Two cycles spray coating. (scale bar: 20 µm).

To maintain the gas-permeability of the device, and keep the NMOECT with adequate electrical performance, in this study, the fibrous sheet formed by four-minutes electrospinning was used as substrate. The spray coating was also optimized to coat the PEDOT:PSS less than 500 nm.

The microstructure with a smaller scale was checked by SEM image. The SEM image of a fabricated NMOECT is shown in Figure 21 (a). The drain/source electrodes, and the polymer channel are in a porous structure. The PEDOT:PSS is conductive, which is showing the white color in the SEM image. In the channel area, most parts are still porous that ensures gas-permeability, while some pores of the nanomesh are blocked by the PEDOT:PSS film, as shown in Figure 21(c) and Figure 21(d).

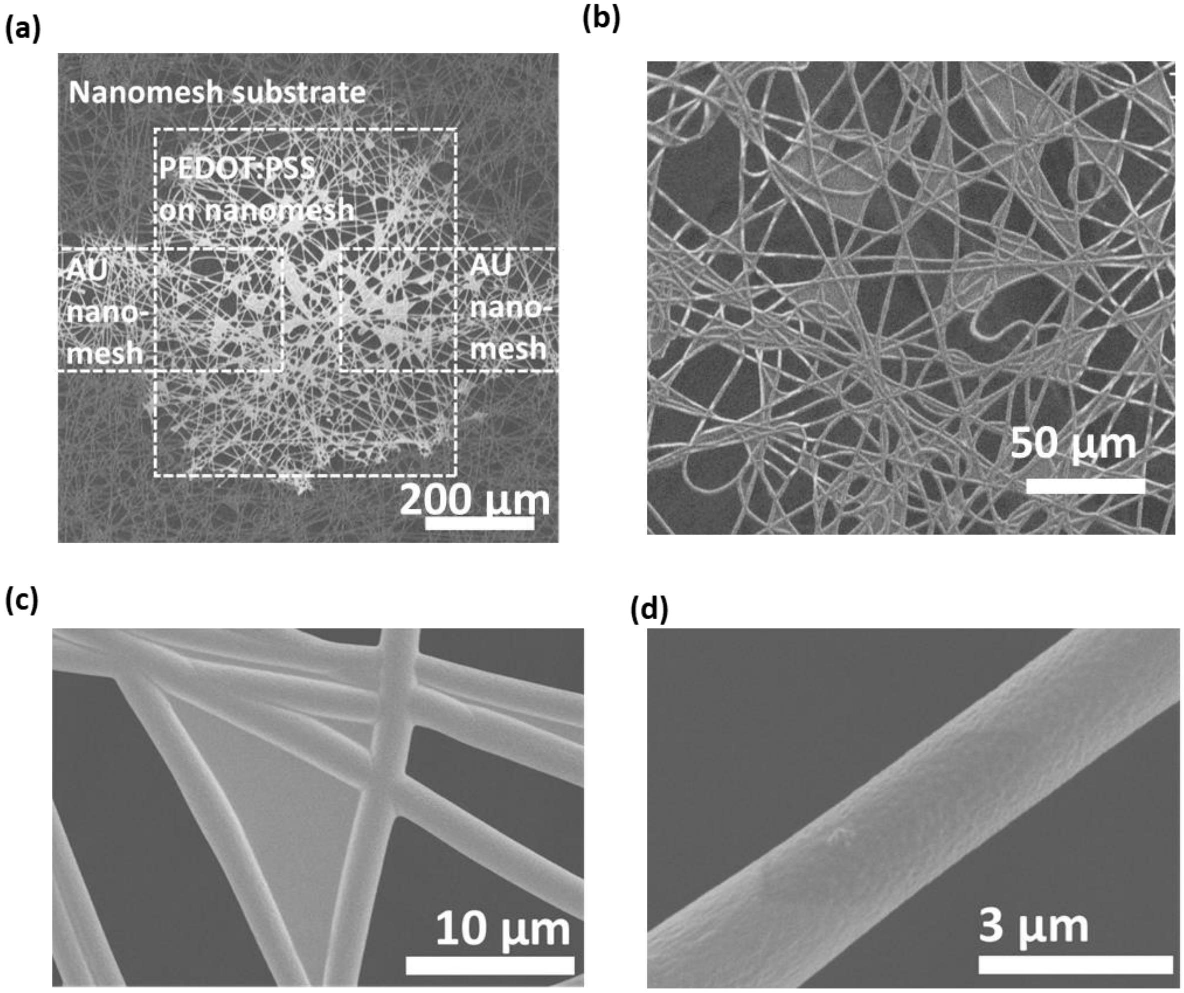

Figure 21. SEM image of the fabricated NMOECT with various scale bar values.

The image of a fabricated NMOECT electrode that is laminated onto the skin surface is shown in Figure 22. The NMOECT electrode is conformably attached to the skin surface. The Au electrodes on the parylene film are used for characterization in the research, to reduce the mechanical mismatch between the device and external cables, which can be replaced by the other gas-permeable wiring technologies[24] in future on-skin applications.

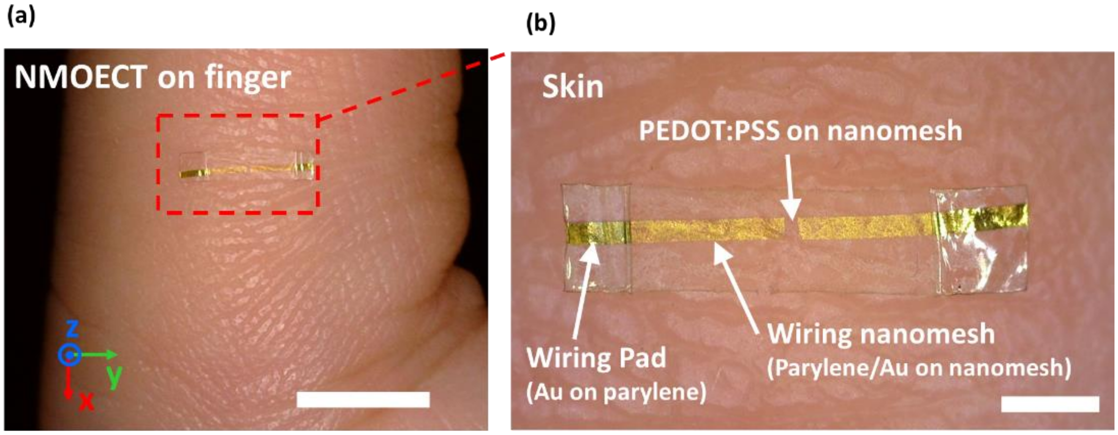

Figure 22. (a) A NMOECT electrodes on the skin of a finger. (Scale bar: 5 mm) (b) The enlarged NMOECT electrode. (Scale bar: 1 mm).

2.2 Electrical characteristics of the NMOECT

To characterizing the electrical performance of the NMOECT, a planer gate with PEDOT/Au structure was also coated and patterned during device fabrication. The gate was used for loading the controllable signals from the measurement equipement (semiconductor analyzer) to the NMOECT, which can be used to quantificational characterizing the device, such as transconductance, response speed, and so on. Two devices with different patterns are shown in Figure 23. The area of the gate is much larger than the channel size, and the PEDOT:PSS on the gate was used, to reduce the impedance between gate and electrolyte and avoid the voltage drop on the gate electrode[62]. The parylene frame was used to support and manipulate the device during characterization. The gold wires are extended from the nanomesh to the parylene frame, to reduce the mechanical mismatch between the characterizing cables and the NMOECT. The cables were connected with the pads by tapes. Phosphate-buffered saline (PBS) solution was used as the electrolyte. The PBS solution is widely used to simulate the liquid environment in the tissue, which is in good biocompatibility, can also be used for the on-skin application. The PBS solution has an ion conductivity around 0.01 S/m, which is sufficiently high for the operation of the OECTs, and the intrinsic performance of the NMOECT can be observed. In Chapter 4, the solid-state polymer electrolyte is developed and embedded with the NMOECT for the practice application.

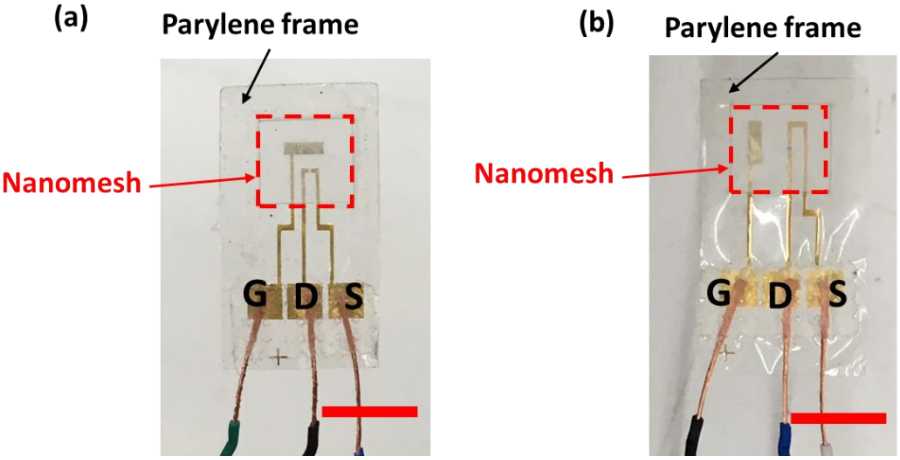

Figure 23. Two patterns of the fabricated NMOECT for electrical characterization (scale bar: 5 mm).

The setup for the characterization of the NMOECT is shown in Figure 24. The top-view schematic and real device are shown in Figure 24(b) and (c) respectively. As discussed in the section on device fabrication, the parylene/PI frame was used as the supporting layer during the fabrication and characterization. The NMOECTs were not peeled off from PI supporting film during electrical characterization, for easily handling the devices. A 5-μL PBS solution was dripped onto the channel part of NMOECTs that was suspended on glass beneath the edge of PI film, to avoid PBS solution contact with the surface beneath the device. The droplet of PBS solution was confined on the channel because of the surface tension of PBS solution, as shown in Figure 24(a). The PBS solution connected the gate electrode and the channel part. The gate, drain, and source wiring pads were connected to the copper wire using tapes to the semiconductor analyzer for inputting and outputting signals, as shown in Figure 24(c). The I–V electrical characterization of the NMOECT was conducted in a semiconductor analyzer (Keysight B1500) using a source measure unit (SMU) module. The time response of the NMOECT was measured by the waveform generator/fast measurement unit (WGFMU) module.

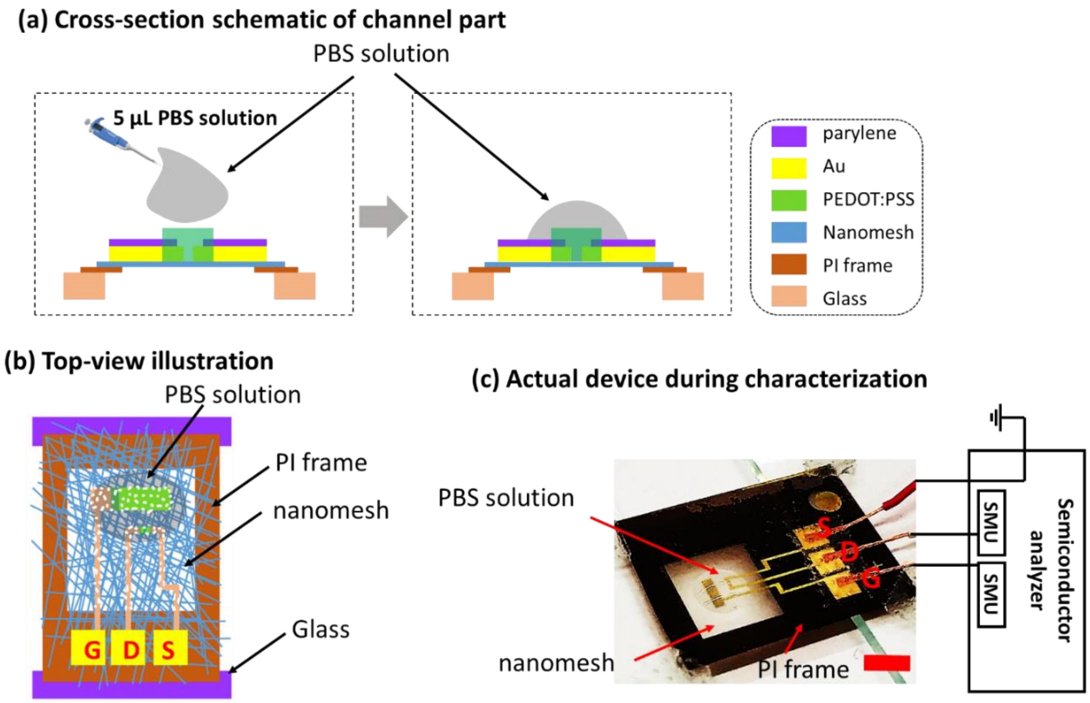

Figure 24. The device setup for electrical performance characterization. (a) Cross-section schematic of the channel part of NMOECT during characterization. (b) Top-view schematic of the NMOECT used for electrical characterization. (c) Photography of the actual device during the characterization (scale bar: 5 mm).

The electrical performance of NMOECT is dependant on the amount of PEDOT:PSS coated on the channel part. To characterize the electrical characteristics systematically, in this study, the NMOECT with various amounts of coated PEDOT:PSS were fabricated. All the fabrication processes were identical except for the coating of PEDOT:PSS. The amounts of coated PEDOT:PSS were controlled by varying the repeating times of the spray coating cycle from one to four times.

First is the measurement of the steady-state characteristics, including the transfer curves ($\mathrm{I_D} - \mathrm{V_G}$) and output curves ($\mathrm{I_D} - \mathrm{V_D}$), as shown in Figure 25. During the measurement, the source electrodes were connected to 0 V, while the gate and drain electrodes were applied with voltage signals. The transfer curves were measured under $\mathrm{V_D} = -0.6\ \mathrm{V}$ while the gate voltage ($\mathrm{V_G}$) was swept from -0.3 V to 0.3 V. The transfer curves are plotted in black solid lines. The NMOECT exhibits typical P-type depletion-mode transistor behaviors; the absolute value of the drain current decreases when the gate voltage was swept towards the positive direction.

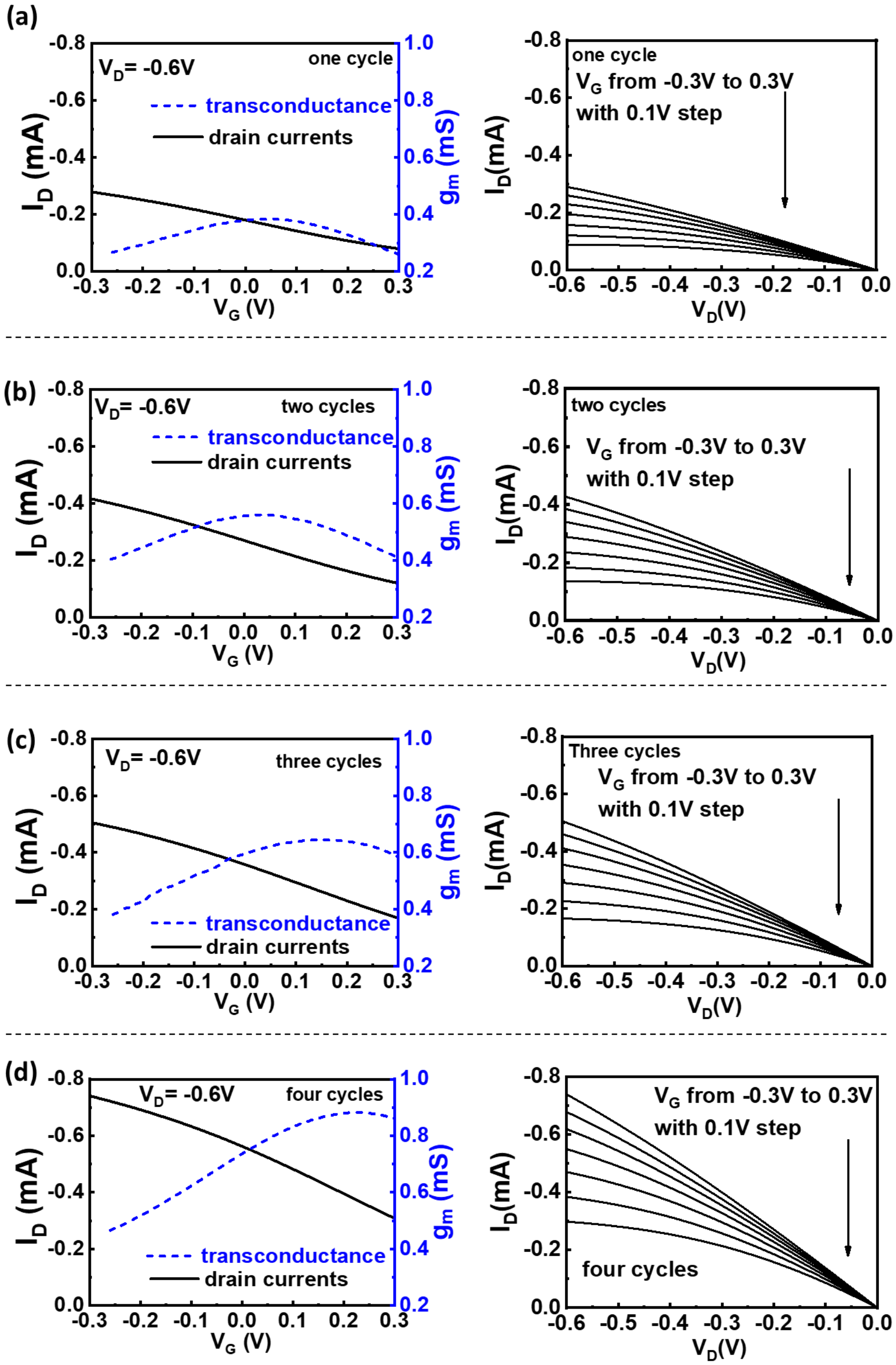

Figure 25. (a–d) Transfer curve (black) and corresponding transconductance (blue) and output curves of NMOECT with PEDOT:PSS spray coating for (a) one cycle, (b) two cycles, (c) three cycles, and (d) four cycles.

The transconductance in each figure was extracted from the transfer curve by the following equation:

$$g_m = \frac{\Delta I_D}{\Delta V_G} \tag{1}$$

The g_m represents the ability to transfer the change of gate voltage to the change of drain current. The transconductance values versus gate voltage are plotted using blue dashed lines in Figure 25.

For the output curves, the drain voltage V_D was swept from -0.6 V to 0 V, while the gate voltage V_G was biased from -0.3 V to 0.3 V with a step of 0.1 V. The output curves in Figure 25 show a good ohmic contact between the channel and drain/source electrodes. They also reveal that the PEDOT:PSS based OECT is rarely working in the saturation region. According to the theoretical equation fitting of the experimental results, a threshold voltage of 0.75 V can be extracted. So the pinch-off voltage is in the range of -1.05 V to -0.45 V corresponding to the gate voltage from -0.3 V to 0.3 V. So at $V_D = -0.6\,V$, only the $V_G > 0.15\,V$ is showing the pinch-off behavior or saturation region. The detail about the fitting of the characteristics of the performance of NMOECT will be discussed in the next section.

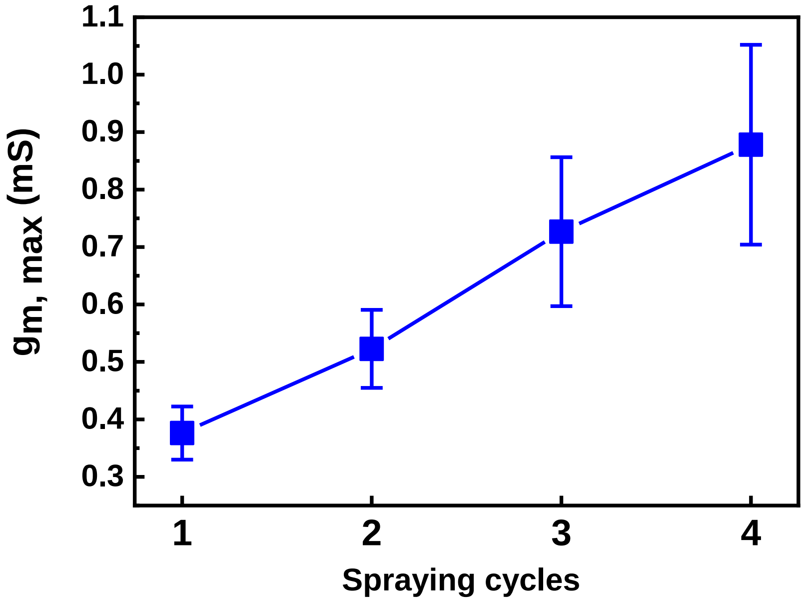

Figure 26. The maximum transconductance of NMOECTs with various amount of PEDOT:PSS.

To see the variation, the NMOECTs with various amount of PEDOT:PSS were fabricated multi times. The statistic results of the maximum transconductance ($g_{m,max}$) are plotted in Figure 26. The $g_{m,max}$ increased with the increasing amount of the PEDOT:PSS, while a larger variation was also observed. A maximum transconductance from 0.38 to 0.88 mS was observed in each figure.

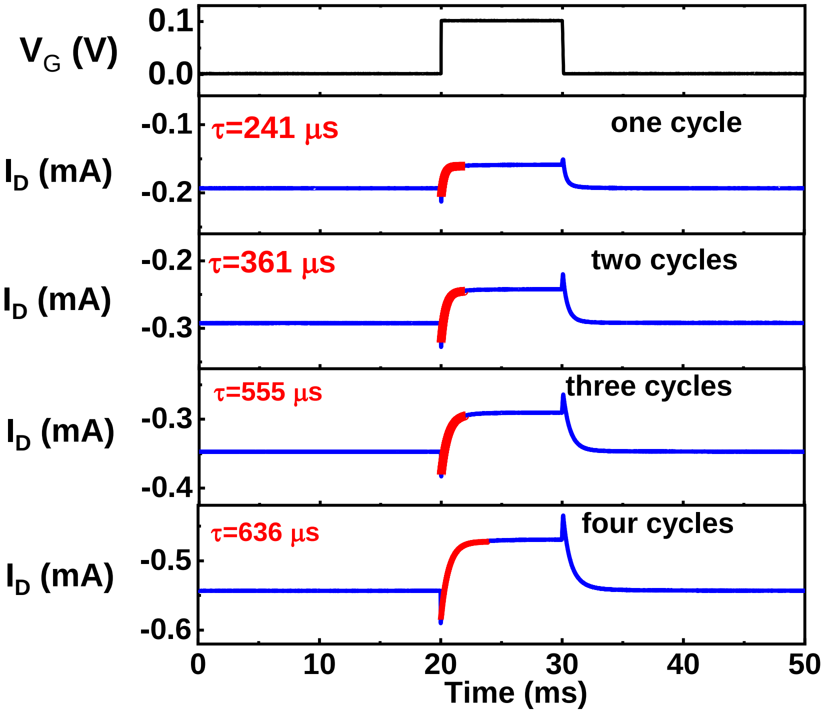

Figure 27. Results of response speed of the NMOECT with various amount of coated PEDOT:PSS.

The above characterizations are steady-state performance, which is using slow signal sweep to make sure that the NMOECT fully responds to applied signals. However, if the change of applied signal is too fast, the response of NMOECT might not follow the change. A NMOECT with enough fast response speed is necessary to fully acquire the electrophysiological signals. To investigate the dynamic response speed of the NMOECT, the response time was extracted from the change of drain currents caused by an applied gate pulse, as shown in Figure 27. A gate pulse of 10 ms with amplitude of 100 mV was applied to the gate, while the drain voltage was biased at -0.6 V. A current change could be observed. By fitting the current change using the following exponential decay equation, the time constant can be extracted.

$$\Delta \mathrm{I_D} = \Delta \mathrm{I}_{D,max}\left(1 - \mathrm{e}^{-\frac{\mathrm{t}-\mathrm{t_0}}{\tau}}\right) \tag{2}$$

$\Delta \mathrm{I_D}$ is the change of drain current, $\Delta \mathrm{I}_{D,max}$ is the change of drain current when the NMOECT fully responds to the gate pulse. $\mathrm{t_0}$ is the time when the gate voltage was applied. τ is the time constant and also the parameter used to define the response time of the NMOECT.

The results in Figure 27 show that with an increasing amount of PEDOT:PSS, the response times of the NMOECTs increased from 361 to 636 μs, revealing that the bandwidths of the NMOECTs are more than 1 kHz, which can fully cover all frequency ranges of bio-electrophysiological signals.

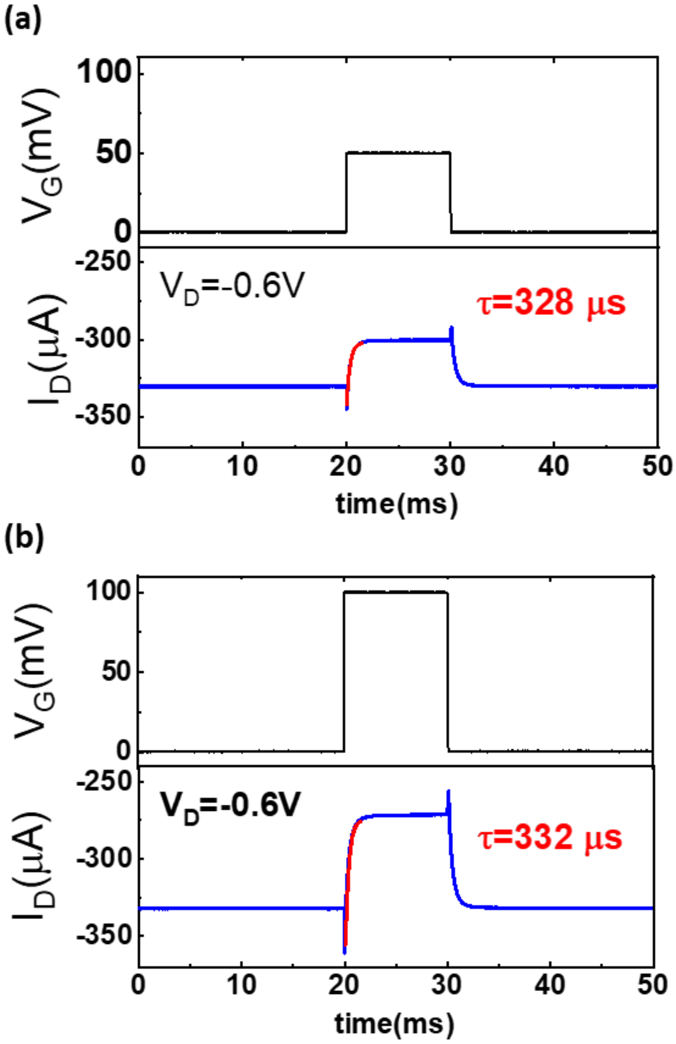

Figure 28. Dynamic drain current responses to a gate pulse with 10-ms width (top black curve) at $V_D = -0.6V$. The amplitudes of gate pulses are (a) 50 mV and (b) 100 mV respectively.

In the experiment of characterizing the response speed, the influence of the amplitudes of gate pulse can be neglected, as shown in Figure 28. The response times were measured by using 0.1 V and 0.05 V gate pulse respectively. The time constants were estimated to 332 μs and 328 μs respectively, with only a 1.2 % difference. According to the physics mechanism of OECT[63], the transient behavior of an OECT can be modeled by a charging ionic current between the gate and channel, using an equivalent circuit consisting of a resistor in series with a capacitor (RC circuit). This equivalent circuit implies that the time required for the channel current in an OECT to respond to a change in the gate voltage is characterized by an RC time constant defined by the ionic circuit between the gate and channel. For the RC charging model, the time constant is irrelevant to the applied voltage, so the applied voltage does not matter for the time constant.

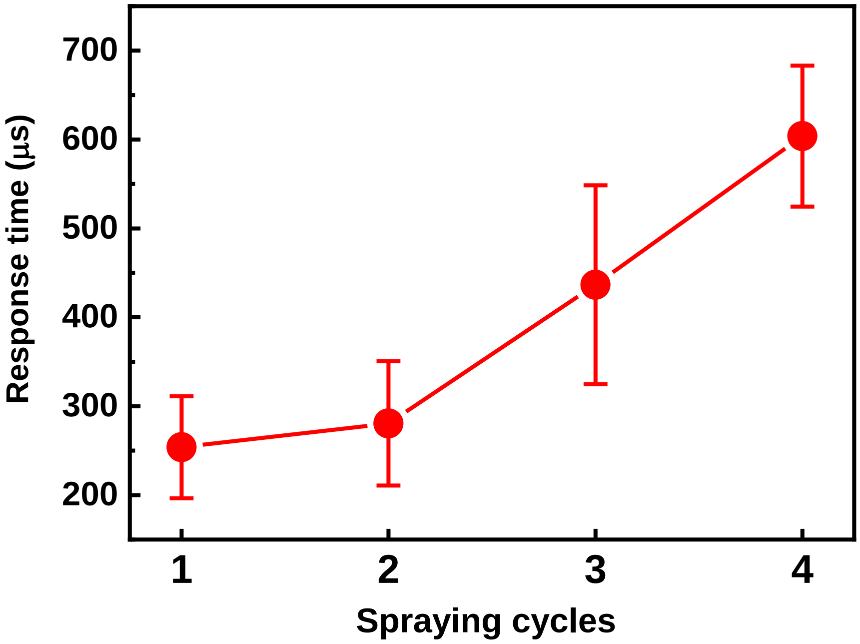

Figure 29. The response time of NMOECTs with various amount of PEDOT:PSS.

The statisctic results of the response time are also plotted versus spray-coating cycles, respectively, as shown in Figure 29, to show the relationship between the amount of the PEDOT:PSS and electrical performance. The response time increased with an increasing amount of PEDOT:PSS. A deviation of about 25.6% was observed due to the randomly distributed nanomesh structure and the formation of freestanding PEDOT:PSS film. Although the maximum transconductance increased with the increasing amount of PEDOT:PSS, the response time increased because more time was needed for fully doping or de-doping the ions into the PEDOT:PSS. A relatively large deviation was observed in this study. In the future, novel coating methods that can uniformly coat the PEDOT:PSS onto the surface of nanomesh fibers can be utilized for solving this issue. In the actual application as on-skin active electrodes, NMOECTs with two cycles of spray coating were chosen for experiments and demonstrations because they are more gas-permeable and have enough high transconductance, which is preferable for on-skin use.

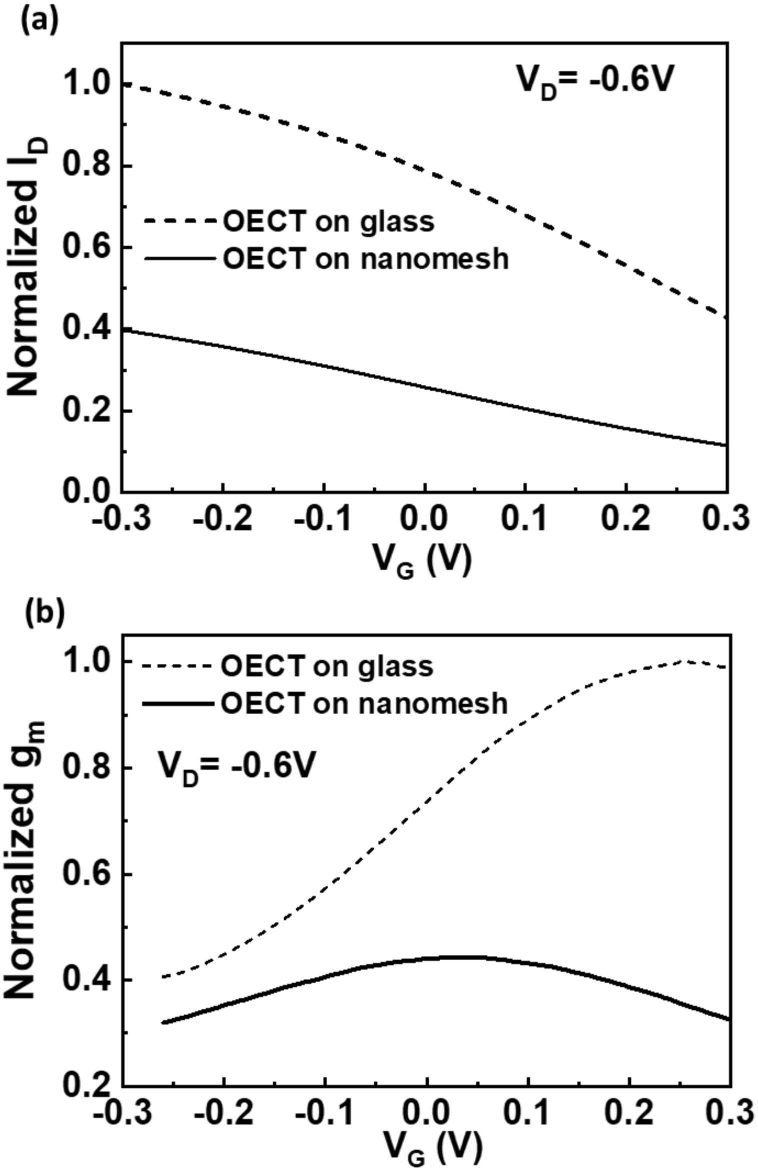

Figure 30. The comparison of OECT fabricated on glass substrate and nanomesh substrate. (a) transfer curves. (b) Transconductance.

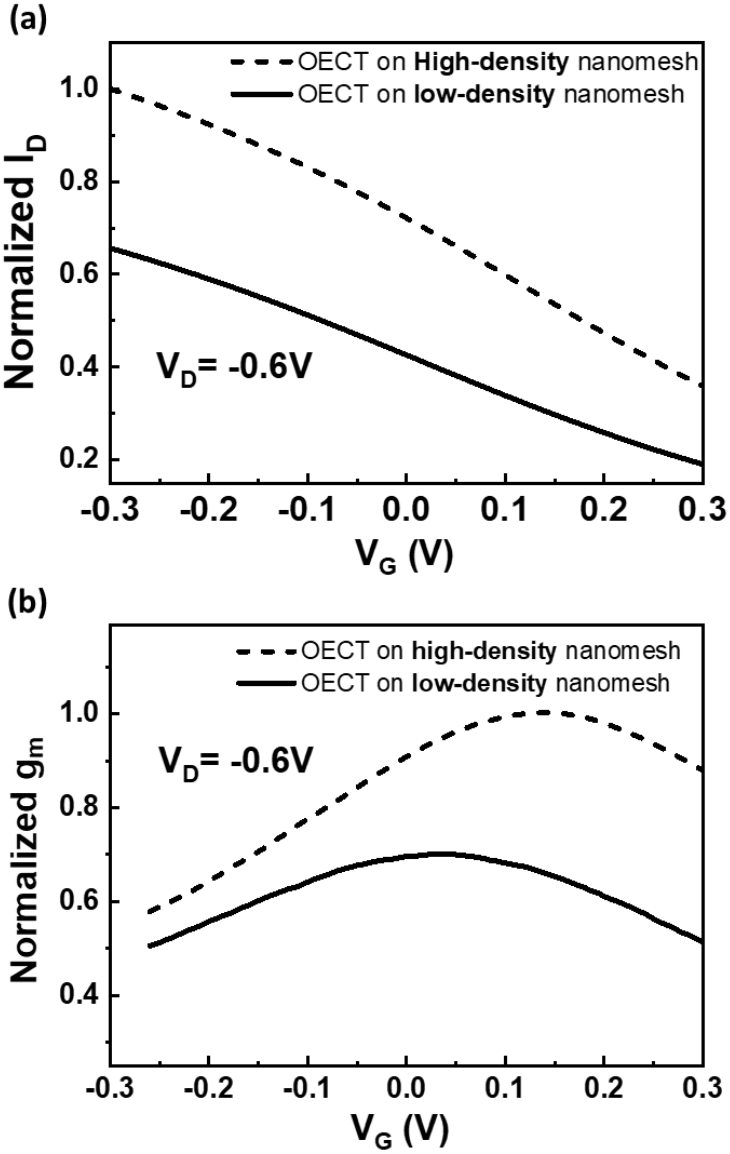

Figure 31. The comparison of OECT fabricated on high-density nanomesh and low-density nanomesh. (a) transfer curves. (b) Transconductance.

One concern of the NMOECT is the influence of the non-uniform structure comparing with the film-type device. To investigate the effect of the porous nanomesh structure on the performance of the NMOECT, we fabricated the OECT using the glass as the substrate and follow the identical fabrication process of the NMOECT. The steady-state electrical characteristics of the OECT on nanomesh and glass were compared. The results are shown in Figure 30. To make the comparison clear, the data were normalized. The OECT on nanomesh has smaller drain currents and less transconductance, which is about 40% of the OECT on glass. The porous nanomesh structure makes the polymer channel less continuous, resulting in higher channel conductance, so the drain current decreases. At the same time, the transconductance was also decreased.

The fiber density of the nanomesh substrate also affects the continuity of the coated PEDOT:PSS. On the high-density nanomesh, the PEDOT:PSS tends to fill more pores, forming more continuous film, which results in lower channel resistance. To exam this effect, the NMOECTs were fabricated on low-density nanomesh and high-density nanomesh with identical fabrication processes respectively. The densities of the fibers were controlled by controlling the electrospinning time. The time for forming low-density and high-density nanomesh were 4 minutes and 10 minutes respectively. The electrical performances of the NMOECTs were compared, as shown in Figure 31. The results were normalized to show easier comparison. From the results, we can see that the NMOECT on higher fibrous density shows a higher drain current and higher transconductance. However, the high-density nanomesh is less porous, as discussed before. For the NMOECT used as on-skin electrodes, a more porous structure is prepared because of its better gas-permeability. Therefore, the low-density nanomesh was used for the fabrication of our electrophysiological electrodes.

One limitation of the organic materials-based electronic device is the instability after repeating use. To check the stability, the cycling measurements of transfer curves and transconductances of NMOECT were performed. The transfer curves of the NMOECT were measured for 100 consecutive cycles, as shown in Figure 32 (a), with depicting every 25 cycles. The normalized transconductance at V_G=0 V for each cycle is plotted in Figure 32 (b). After 100 cycles, the transconductance of the PEDOT:PSS degraded to 88% of the initial device. The cycling stability is consistent with previously reported PEDOT:PSS based OECT[64].

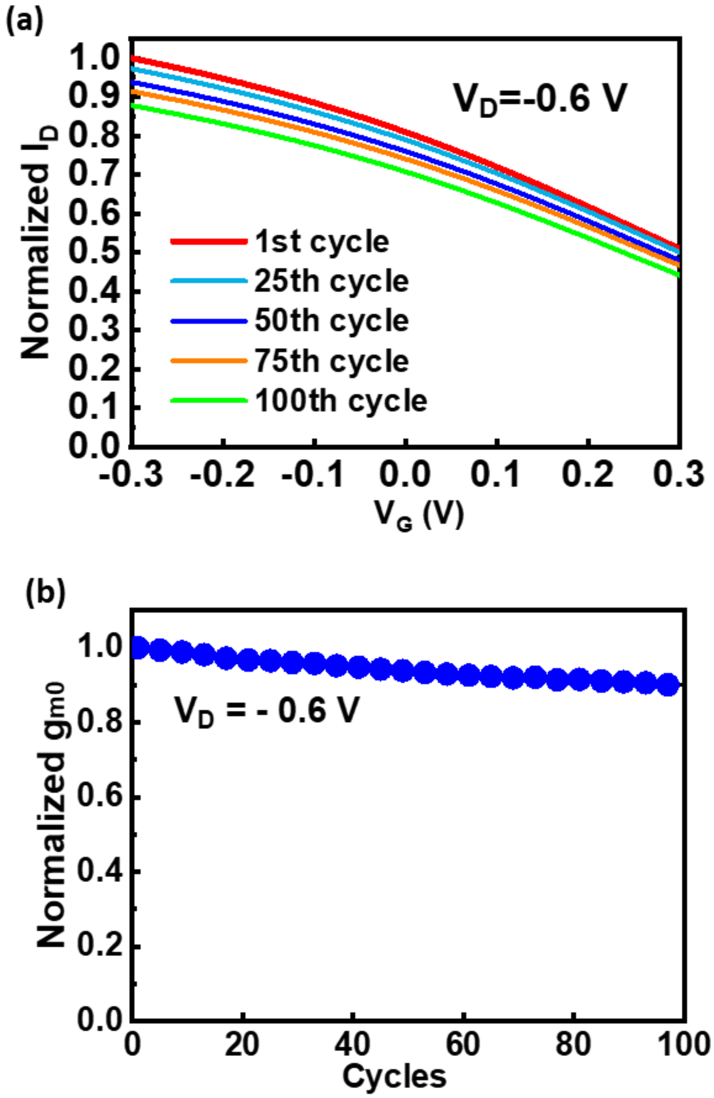

Figure 32. (a) Cycling measured transfer curves of NMOECT. The device was measured for 100 consecutive cycles at $V_D = -0.6$ *V, and the normalized transfer curves of* 1^{st}, 25^{th}, 50^{th}, 75^{th}, *and* 100^{th} *cycles are plotted. (b) The normalized transconductances at* $V_G=0$ *V of each transfer curves.*

2.3 Mechanical durability of the NMOECT

The human skin is not flat and can be stretched during daily-life activities[65]. The on-skin electrodes should be durable against mechanical deformation during real application. To investigate the durability against the mechanical deformation of the NMOECT, the mechanical bending was loaded to the NMOECTs. We measured the transfer curves of the NMOECTs after bending with various bending diameters. Repeating bending experiments were also performed.

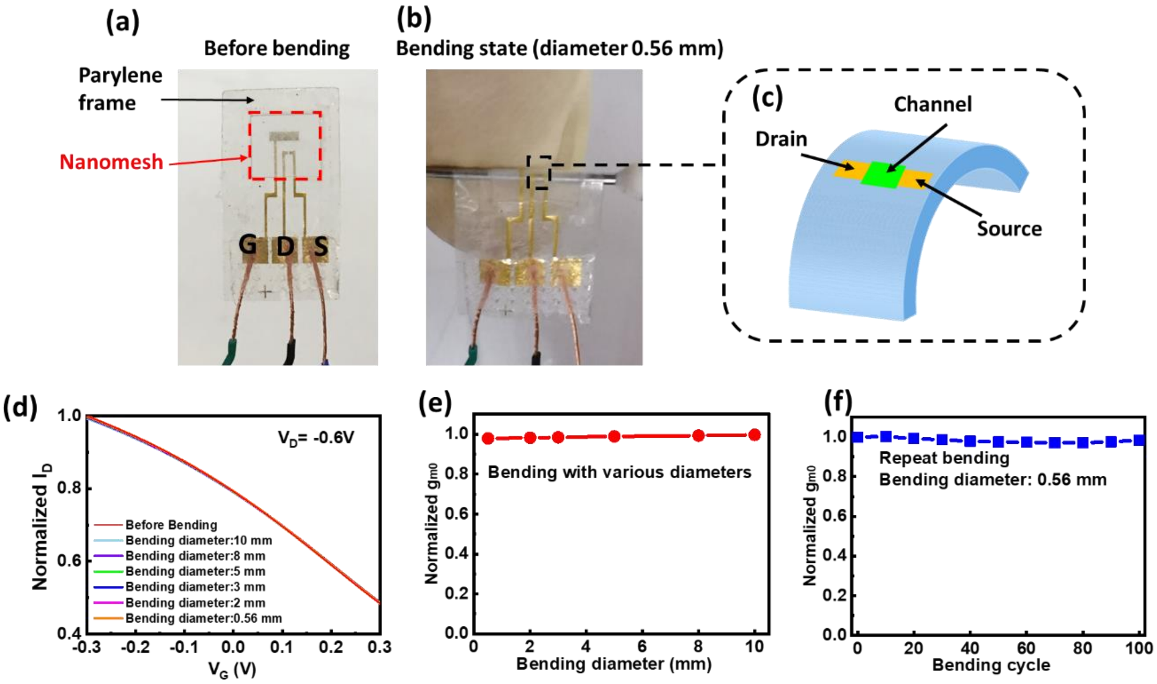

Figure 33. The mechanical bending characterization of the NMOECT with bending direction perpendicular to the channel. (a) The planer NMOECT with parylene frame before bending (scale bar: 5 mm). (b) The NMOECT is in bending state (The photo shows that the device is bent with diameter of 0.56 mm). (c) The schematic of bending state of the OECT. (d-e) The normalized transfer curves and transconductance at V_G*=0 V of the NMOECT in various bending diameter from 0.56 mm to 10 mm, respectively. (f) The normalized transconductances of NMOECT during 100 bending cycles at* V_G*=0 V, the transfer curves were measured after each 10 mechanical bend.*

The NMOECT is in a 2-D layout, so the bending direction could be either perpendicular or parallel to the drain-channel-source direction. To control the bending direction and bending area, two different patterns of NMOECTs were fabricated. As shown in Figure 33 (a) and Figure 34 (a). The device fabricated for bending experiments was in an in-plane gate structure, with gate electrodes close to the channel. To avoid the effect of rigid parts during bending (the connection wires), the wiring pads parts were kept stable and the bends were always in the same direction, while the channels were designed to be bent perpendicularly or parallel to the bending direction respectively, as shown in Figure 33 (b) (c) and Figure 34 (b) (c). First, the influence of the bending diameters was checked. The NMOECT was bent to various bending diameters from 10 mm to 0.56

mm, and the transfer curves were measured after each bending. To check the repeatability, the bending with a diameter of 0.56 mm is repeated for 100 cycles. The results are shown in Figure 33 (d) to (f) and Figure 34 (d) to (f). The transconductance of the NMOECT kept practically unchanged after bending in diameters from 10 mm to 0.56 mm, for both the parallel and perpendicular bending. After repeating bending in a diameter of 0.56 mm for 100 cycles, the degradation of the transconductance were less than 2.93 % and 3.67 % in the perpendicular or parallel direction respectively, revealing the good flexibility of the NMOECTs.

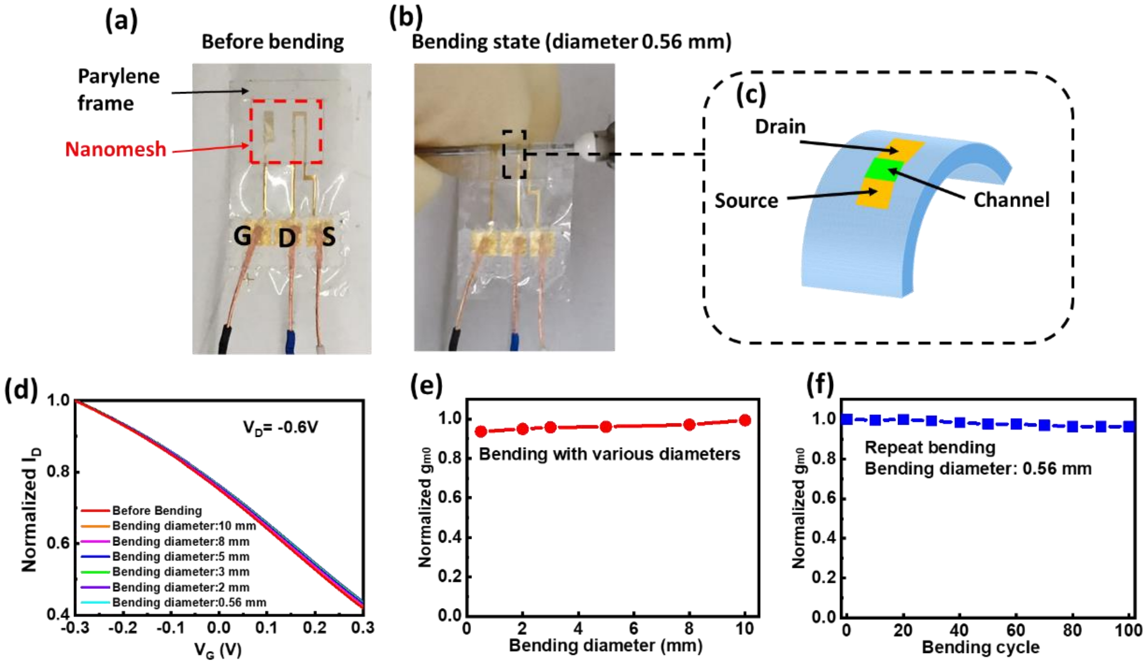

Figure 34. The mechanical bending characterization of the NMOECT with bending direction parallel to the channel. (a) The planer NMOECT with parylene frame before bending (scale bar: 5 mm). (b) The NMOECT is in bending state (The photo shows that the device is bent with a diameter of 0.56 mm). (c) The schematic of the bending state of the OECT. (d-e) The normalized transfer curves and transconductance at V_G*=0 V of the NMOECT in various bending diameter from 0.56 mm to 10 mm, respectively. (f) The normalized transconductances of NMOECT during 100 bending cycles at* V_G*=0 V, the transfer curves were measured after each 10 mechanical bend.*

An even more serious deformation was also implemented to the NMOECT, as shown in Figure 35 (a), the shape of the device can be recovered after crumping. The transfer curves before and after the crumping were measured, as shown in Figure 35 (b), revealing that the degradation of the transfer curves can be neglected after the crumpling deformation. The results suggest that the NMOECT is in excellent flexibility against the mechanical bending, rendering it suitable as the on-skin electrode.

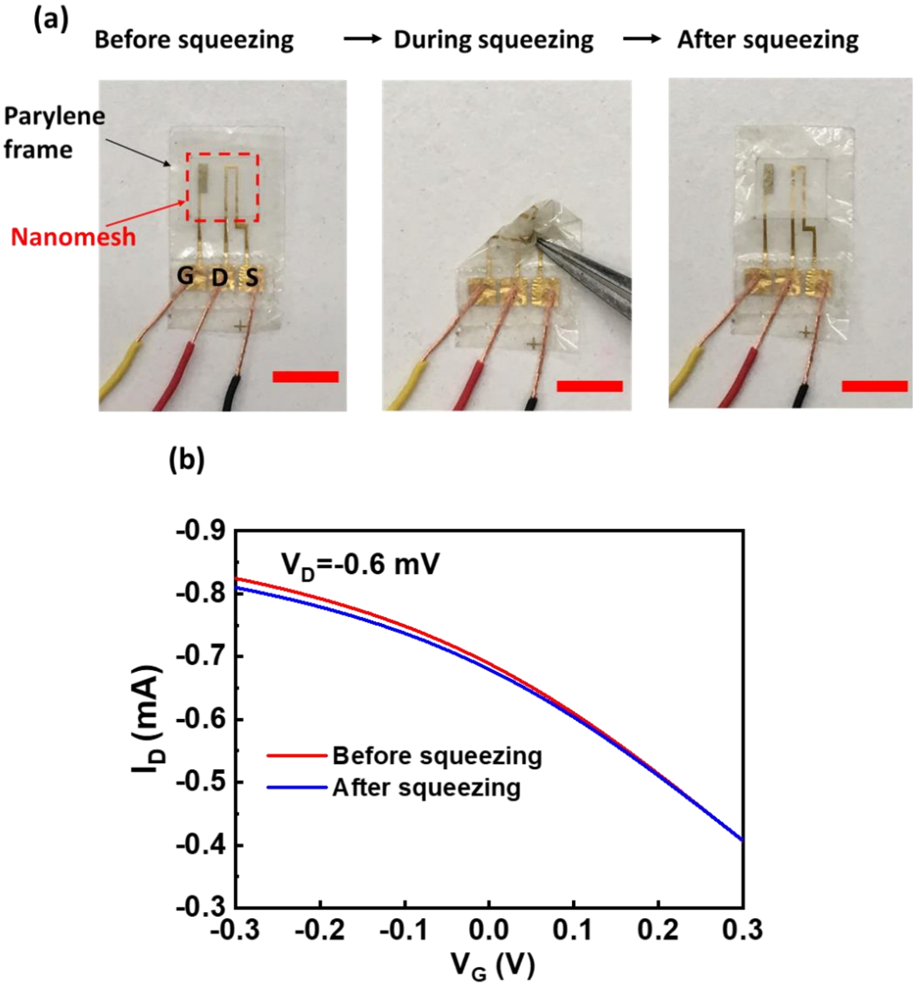

Figure 35. Electrical performance of a four-cycle-spray-coating NMOECT before and after crumpling. (a) The planer NMOECT with parylene frame before, during, and after crumpling, respectively (scale bar: 5 mm). (b) The transfer curves at V_D= -0.6 V of the NMOECT before and after crumpling, respectively.

2.4 Models of the NMOECT

To more deeply understanding the performance of the NMOECTs and properly design the circuit and connection during the application, the mathematical equations that describe the channel currents under the controlling of gate voltage and drain voltages are utilized to fit the experimental data of electrical performance. The model can be used to fit the experimental data. The parameters used in the model, such as the threshold voltage, can be used to explain the characteristics of the NMOECT.

The conventional models used to fit the steady-state of NMOECT was originally proposed by Daniel Bernards and George Malliaras[63] , as shown in the following equation:

$$\mathrm{I_D} = \begin{cases} 0, & \text{for } \mathrm{V_G} > \mathrm{V_T} \\ \mu \mathrm{C} \dfrac{\mathrm{Wd}}{\mathrm{L}} \left[1 - \dfrac{\mathrm{V_G} - \frac{1}{2}\mathrm{V_D}}{\mathrm{V_T}} \right] \mathrm{V_D}, & \text{for } \mathrm{V_G} < \mathrm{V_T}, \quad \text{and } \mathrm{V_D} > \mathrm{V_G} - \mathrm{V_T} \\ -\mu \mathrm{C} \dfrac{\mathrm{Wd}}{\mathrm{L}} \dfrac{(\mathrm{V_G} - \mathrm{V_T})^2}{2\mathrm{V_T}}, & \text{for } \mathrm{V_G} < \mathrm{V_T}, \quad \text{and } \mathrm{V_D} < \mathrm{V_G} - \mathrm{V_T} \end{cases} \tag{3}$$

Three regions are used, cut-off region, linear region, and saturation region, as described following.

(1) $\mathrm{V_G} > \mathrm{V_T}$: In the cut-off region, all the anions in the PEDOT:PSS channel are compensated by the doping of cations in the electrolyte, so there is very little holes in the PEDOT:PSS channel, the OECT can be regarded as off state.

(2) $\mathrm{V_G} < \mathrm{V_T}$, and $\mathrm{V}_D > V_G - V_T$. In this region, because $\mathrm{V_G} < \mathrm{V_T}$, the coupling between anions in the PEDOT:PSS and cations in the electrolyte released, the PEDOT:PSS becomes more conductive, OECT goes to on state. In this case, $\mathrm{V}_D > V_G - V_T$, or $V_G - V_D < V_T$, the whole channel is in on-state. The drain current is linear with the drain voltage. This region is called linear region.

(3) $\mathrm{V_G} < \mathrm{V_T}$, and $\mathrm{V}_D > V_G - V_T$. In this region, the channel is in on state due to $\mathrm{V_G} < \mathrm{V_T}$. While, the difference is $\mathrm{V}_D < V_G - V_T$, or $V_G - V_D > V_T$, some parts of the channel will be in pinch-off state, then the drain currents will be saturated. This region is called saturation region.

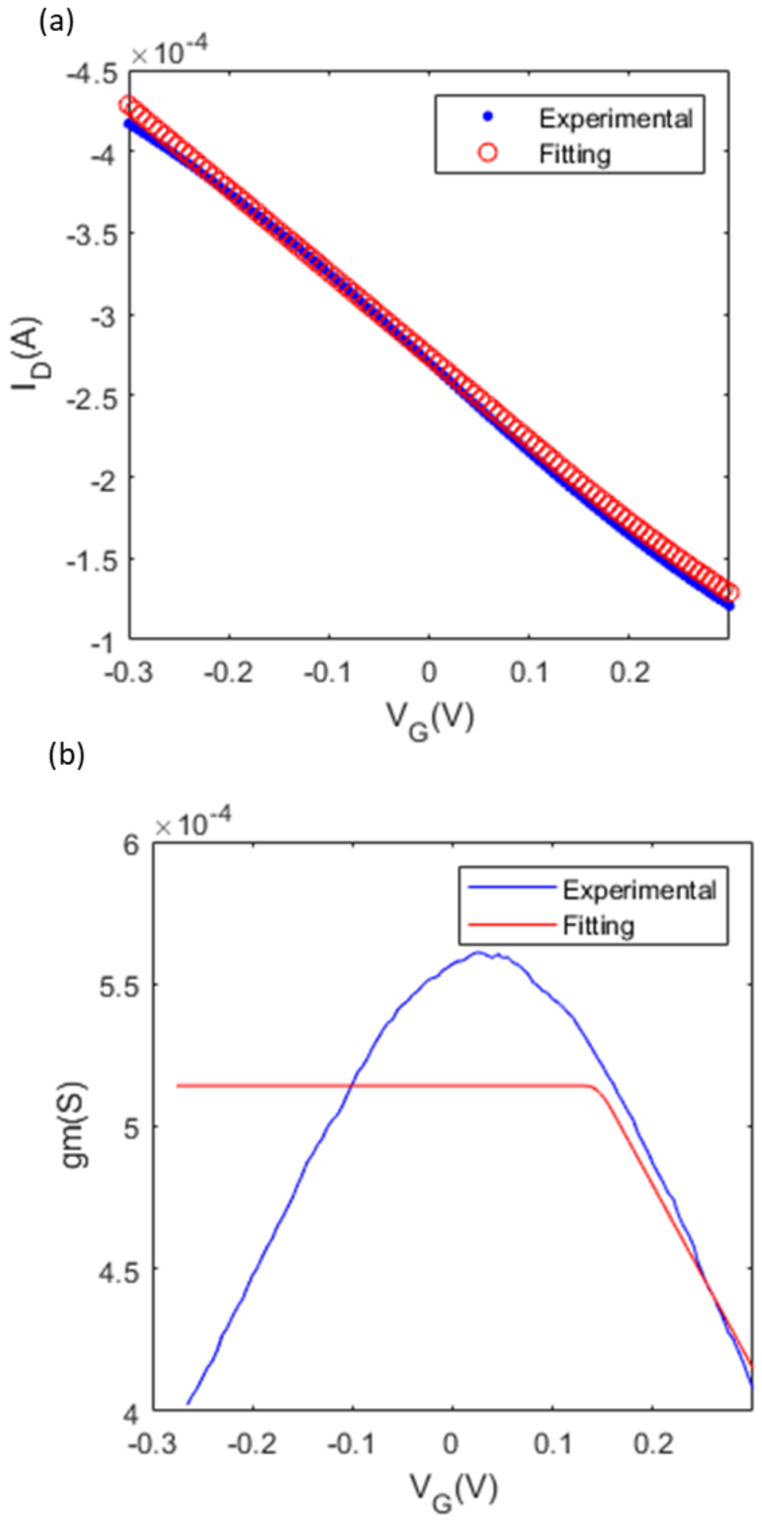

Figure 36. The experiments and fitting results of a NMOECT using the conventional OECT model. (a) transfer curve and (b) transconductance curve.

Based to this model, according to the definition of transconductance, it can be derived from the channel currents equation using $\mathrm{g_m} = \frac{\partial I_D}{\partial V_G}$, the results are shown as following:

$$g_m = \frac{\partial I_D}{\partial V_G} = \begin{cases} 0, & \text{for } \mathrm{V_G > V_T} \\ -\mu\mathrm{C}\frac{\mathrm{Wd}}{\mathrm{L}}\frac{V_D}{V_T}, & \text{for } \mathrm{V_G < V_T}, \quad \text{and } \mathrm{V_D > V_G - V_T} \\ -\mu\mathrm{C}\frac{\mathrm{Wd}}{\mathrm{L}}\frac{(\mathrm{V_G - V_T})}{\mathrm{V_T}}, & \text{for } \mathrm{V_G < V_T}, \quad \text{and } \mathrm{V_D < V_G - V_T} \end{cases} \tag{4}$$

This model can be used to roughly fit the transfer curve and output curve of experimental results. However, the transconductance results do not have a good similarity with experimental results. According to this model, when $\mathrm{V_D > V_G - V_T}$ and $\mathrm{V_G < V_T}$, the $\mathrm{g_m}$ should be a constant value of $(-\mu\mathrm{C}\frac{\mathrm{Wd}}{\mathrm{L}}\frac{V_D}{V_T})$ that is not related to the $\mathrm{V_G}$, but in experimental results in both previous reports[41] and this research, the transconductance curve is not showing the constant value. As the fitting results and experimental results shown in Figure 36, in the fitting curve, the $\mathrm{g_m}$ decrease when the $\mathrm{V_G}$ goes towards the negative direction.

Even the OECT has been investigated for many years, the precise explanation and modeling of the OECT has not been reported in the literature[63, 66-68]. Nissa and the coauthors proposed using several regions to describe the characteristics of the OECT [66], however, the calculated results are discrete and still have some gap to the experimental results.

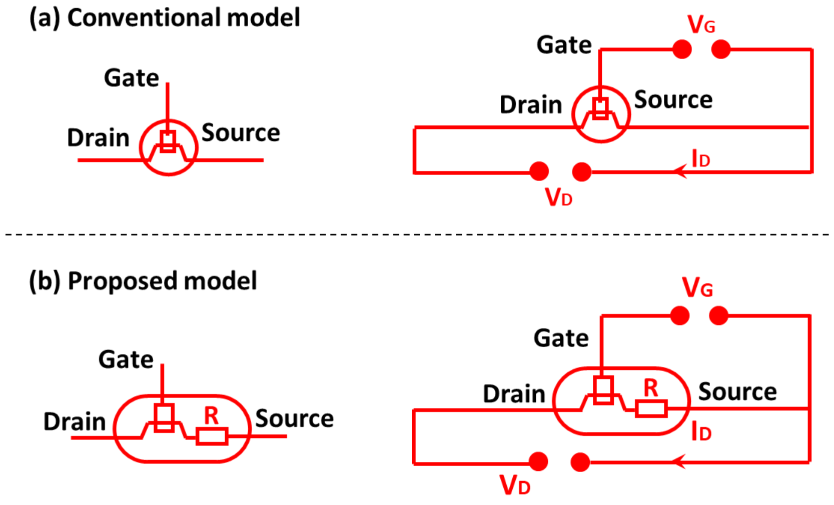

Figure 37. (a) The schematic of the conventional OECT model. (b) The propose OECT model in this study, a serial resistance is implemented.

In this study, we made an assumption that the decrease of the transconductance is caused by a serial resistance in the channel part. Usually, the serial resistance between the channel and electrodes can be ignored because the channel resistance is much higher. However, for the OECT, its PEDOT:PSS channel is in a very low resistance, which is comparable with the contact resistance and the serial resistance. The contact resistance is occupying some part of the applied drain voltage, resulting in the actual voltage applied to the channel is less than $\mathrm{V_D}$. Especially when the $\mathrm{V_G}$ is going towards the negative direction, the channel resistance is further decreased, the channel resistance is much close to the contact resistance. To better fit the electrical characteristics of the NMOECT, a new model that implement a serial resistance with the channel is build, as shown in Figure 37.

The characteristics of a OECT can be described by the following two equations:

$$\mathrm{I_D} = \begin{cases} 0, & \text{for } \mathrm{V_G} > \mathrm{V_T} \\ \mu C \dfrac{\mathrm{Wd}}{\mathrm{L}} \left[1 - \dfrac{\mathrm{V_G} - \frac{1}{2}\mathrm{V_{D0}}}{\mathrm{V_T}} \right] \mathrm{V_{D0}}, & \text{for } \mathrm{V_G} < \mathrm{V_T}, \quad \text{and } \mathrm{V_D} > \mathrm{V_G} - \mathrm{V_T} \\ -\mu C \dfrac{\mathrm{Wd}}{\mathrm{L}} \dfrac{(\mathrm{V_G} - \mathrm{V_T})^2}{2\mathrm{V_T}}, & \text{for } \mathrm{V_G} < \mathrm{V_T}, \quad \text{and } \mathrm{V_D} < \mathrm{V_G} - \mathrm{V_T} \end{cases} \tag{5}$$

$$\mathrm{I_D} R + V_{D0} = V_D \tag{6}$$

Here, $\mathrm{V_{D0}}$ is the voltage drop on the OECT, R is the serial resistance. The equations can be solved using the numerical method.

Figure 38 shows the experimental and fitting results of a NMOECT using the proposed model. The fitting result is showing better overlap with the experimental results, and the trends of the transconductance curve are more similar than the conventional model, revealing that by implementing a serial resistance in the channel, the model can better fit the experimental data. The proposed model also shows better fitting for the output curves, as shown in Figure 39. The model can be utilized to help the circuit design based on the OECTs.

The proposed model used a constant resistance to improve the fitting of the transfer curve, however, the fitting results still need to be improved. The serial resistance could be mainly from the contact between the PEDOT:PSS and the Au drain/source electrodes, and it will change with the change of channel resistance. A more precise model to estimate the contact resistance between the PEDOT:PSS and Au can be utilized in the OECT model and gives better fitting for experimental results.

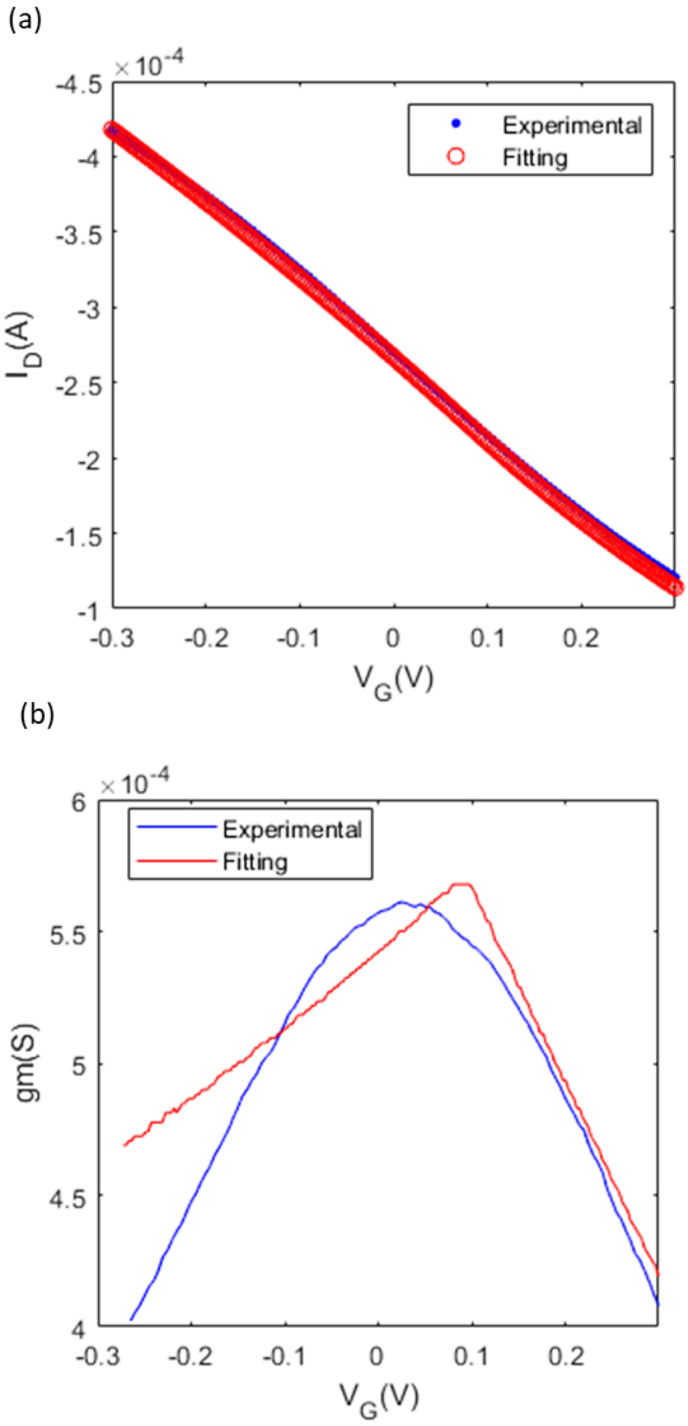

Figure 38. The experiments and fitting results of (a) transfer curve and (b) transconductance curve, using the proposed OECT model.

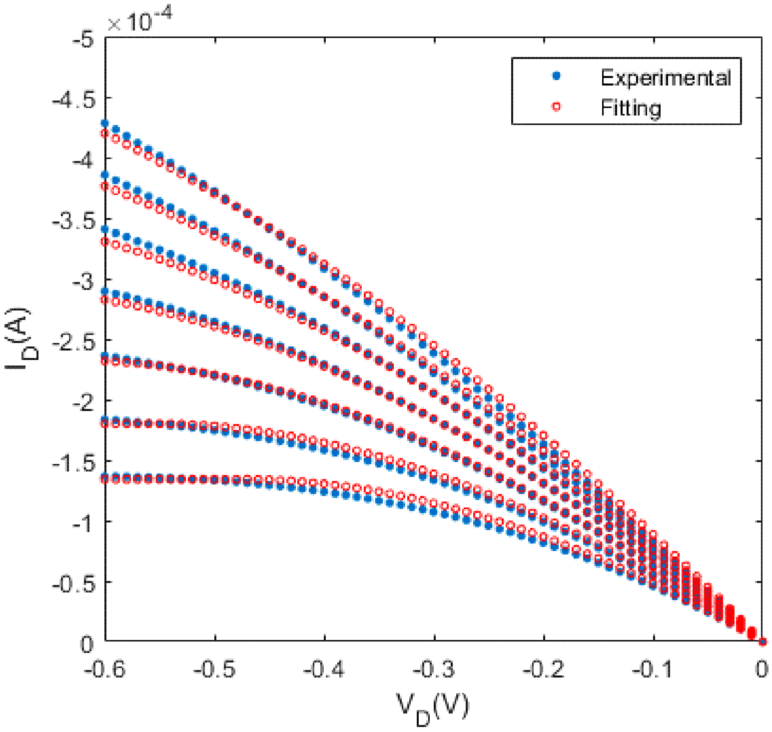

Figure 39. Experimental and fitting data of the output curves.

Chapter 3: NMOECT works as on-skin active electrodes

The Chapter 2 discussed about the fabrication process and characteristics of the NMOECT. In this chapter, the configuration of utilizing the NMOECT as on-skin active electrophysiological electrodes are discussed. The setup to make the signal read by NMOECT readable by the conventional equipment is designed. The ECG signals read by NMOECT electrodes are presented and analyzed. A feasible setup for wireless reading the electrophysiological signals acquired by the NMOECT is also proposed.

3.1 Signal converting and filtering

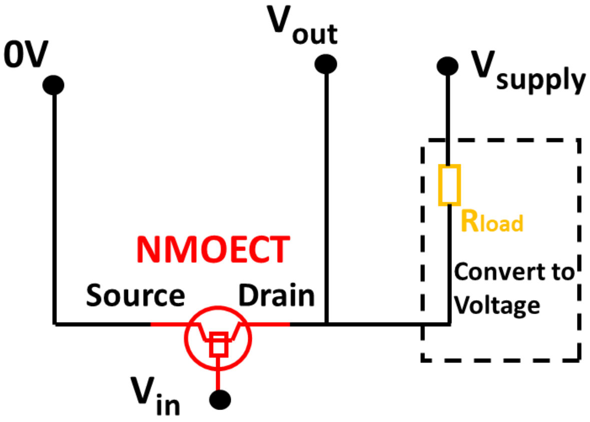

Figure 40. The schematic of configuration for converting the current signal to voltage signal using loading resistor.

In this study, the NMOECTs were developed as the active on-skin electrodes for electrophysiological signal acquiring, its high transconductance makes it a powerful amplifier that outputs high-amplitude current signals. However, the commonly used existing electrophysiological monitoring equipment is recording the voltage signals instead of current signals. Especially for some minimized portable signal reading microcontroller board. To make the signals acquired by NMOECT compatible with the existing electrophysiology recording equipment, it is necessary to convert its outputting current signals into voltage signals, as discussed in the literature. For this purpose, we connected the NMOECT in series with a loading resistor (R_{load}) to a supply voltage (V_{supply}), as shown in Figure 40. For used as on-skin electrophysiological electrodes, the small signals are the target signals. In this circuit, for the small signal, the change of voltage at the output terminal can be expressed using following equation:

$$\Delta \mathrm{V}_{\mathrm{out}} = \Delta I_D \cdot R_{laod} \tag{7}$$

Using the transconductance g_m to represent the change of output currents, we have:

$$\Delta \mathrm{I}_{\mathrm{D}} = g_m \cdot \Delta V_{in} \tag{8}$$

The above two equations can be used to build the relationship between the change of input voltage to the change of output voltage, which is also described as voltage gain:

$$\mathrm{gain} = \frac{\Delta \mathrm{V}_{\mathrm{out}}}{\Delta \mathrm{V}_{\mathrm{in}}} = \frac{\Delta I_D \cdot R_{laod}}{\frac{\Delta \mathrm{I}_{\mathrm{D}}}{g_m}} = g_m R_{laod} \tag{9}$$

So the voltage gain is related to both the transconductance of the NMOECT and the loading resistor.

To investigate the voltage converting performance, the voltage experimental transfer characteristics were measured by measuring the output voltage ($\mathrm{V}_{\mathrm{out}}$) while sweeping the input voltages (V_{in}). Figure 41(a) show the voltage transfer curves in a voltage supply of -1.5 V, with loading resistors of various resistances. To avoid the breakdown of the NMOECTs, we controlled the sweeping range of the V_{in} to ensure that the voltages between the gate and drain electrodes were less than 0.9 V ($|\mathrm{V}_{\mathrm{in}} - \mathrm{V}_{\mathrm{out}}| \leq 0.9$ V), and the dashed line in the figures represent this limitation.

Bases on the data in Figure 41 (a), we extracted the voltage gain using the following equation:

$$\mathrm{gain} = \frac{\Delta \mathrm{V}_{\mathrm{out}}}{\Delta \mathrm{V}_{\mathrm{in}}} \tag{10}$$

The voltage gain is plotted in Figure 41 (b). From Figure (b), we can see that in a certain supply voltage and a certain input voltage bias, a smaller resistor brings higher voltage gain. The reason is that loaded with a smaller resistor gives a larger absolute value of V_{DS} to the NMOECT, which increased the g_{m}. As discussed in the last section, the NMOECT usually works in the linear region, in the linear region, the transconductance of the OECT is proportional to the absolute value of the drain voltage. Increasing of g_{m} leads to the increase of the voltage gain.

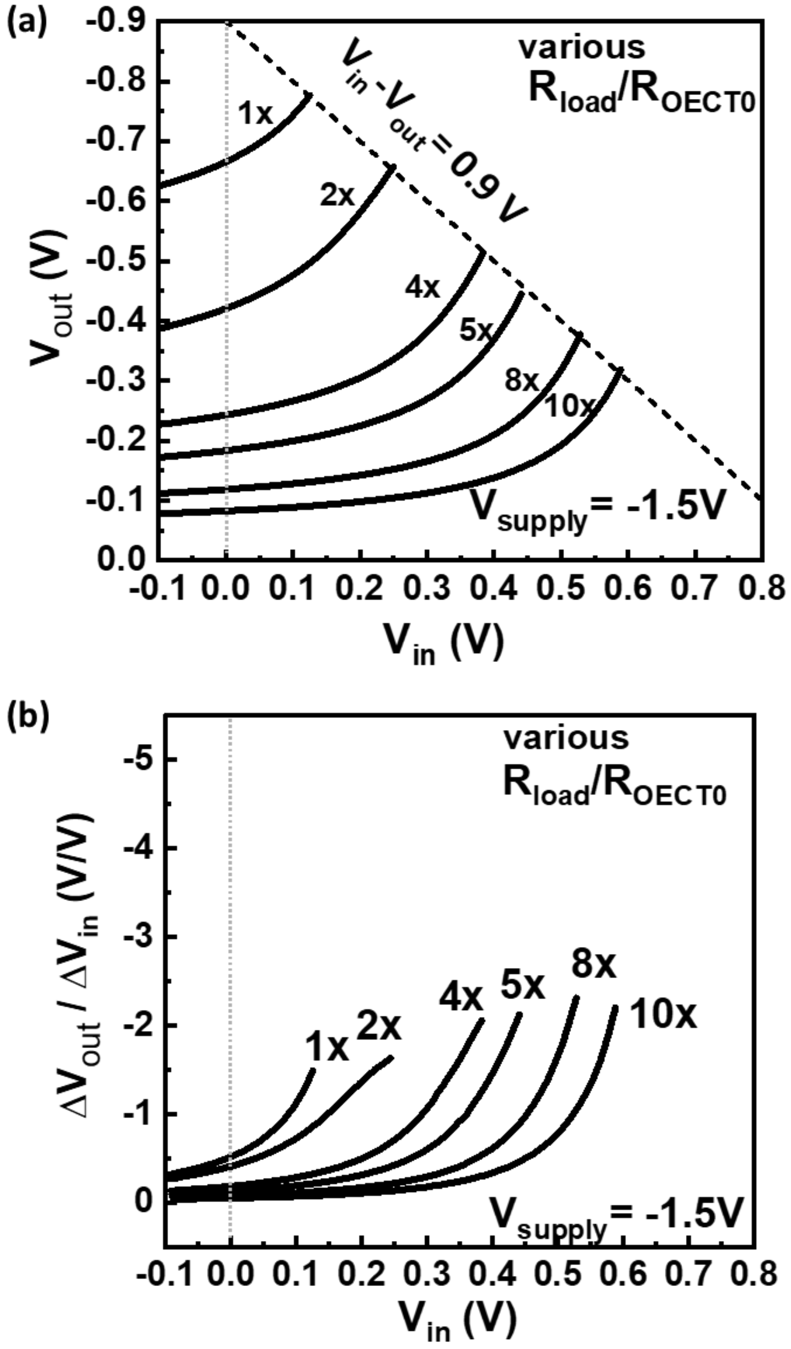

Figure 41. The voltage transfer curve and corresponding voltage gain with various resistance of loading resistors with supplying voltage of -1.5 V. (a) Voltage transfer curves. (b) Voltage gain extracted from the voltage transfer curves.

To improve the V_{DS} of the NMOECT, a relatively larger supply voltage is needed, as the results shown in Figure 42, a higher supplying voltage of -6 V is applied. With the increasing of supplying voltage, the voltage drop on the NMOECT can be larger, which keeps a larger g_m. A voltage gain about 2 can be achieved around $V_G = 0$ V. In a certain supply voltage, the same as supply voltage of -1.5V, a smaller loading resistor also results in a higher V_{DS}.

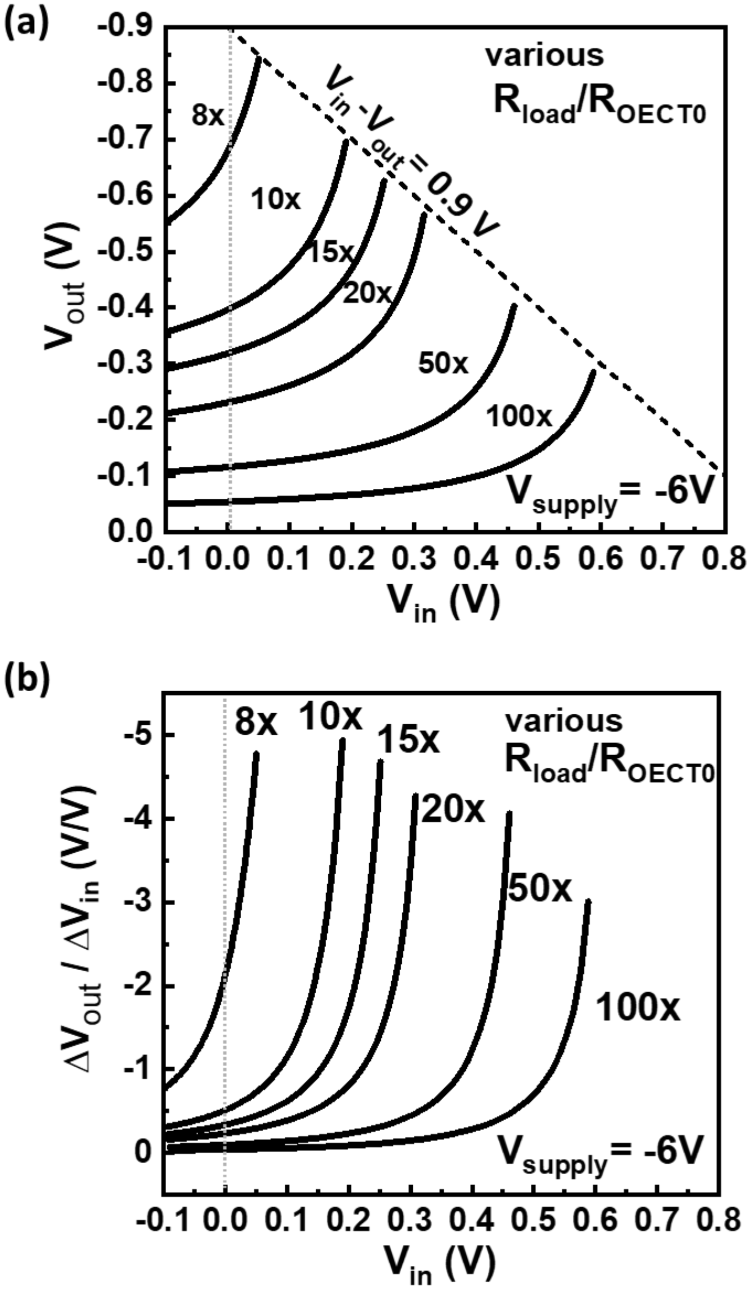

Figure 42. The voltage transfer curve and corresponding voltage gain with various resistance of loading resistors with supplying voltage of -1.5 V. (a) Voltage transfer curves. (b) Voltage gain extracted from the voltage transfer curves.

For full characterization, various supply voltages and loading resistors were connected, and the voltage transfer characteristics were measured. A supply voltages of -2 , -3, and -4.5 V were loaded with various loading resistors, respectively. Then, we extracted the voltage gain at $V_G =$ 0 V (the biopotentials are approximately 0 V) from the measurement data and plotted it in a color map, as shown in Figure 43. The color represents the voltage gain of each measuring point, which reveals that at $V_{supply} = -6$ V and $R_{load}/R_{OECT0} = 8$, the circuits achieved the highest gain. The high supplying voltage (-6 V) and a smaller loading resistor confirmed the high voltage drop on the channel of NMOECT for the high transconductance. However, the supply voltage cannot be too large and the loading resistor should not be too small, otherwise, the voltage drop on the NMOECT will be too large, which will break down the electrolyte and the PEDOT:PSS channel.

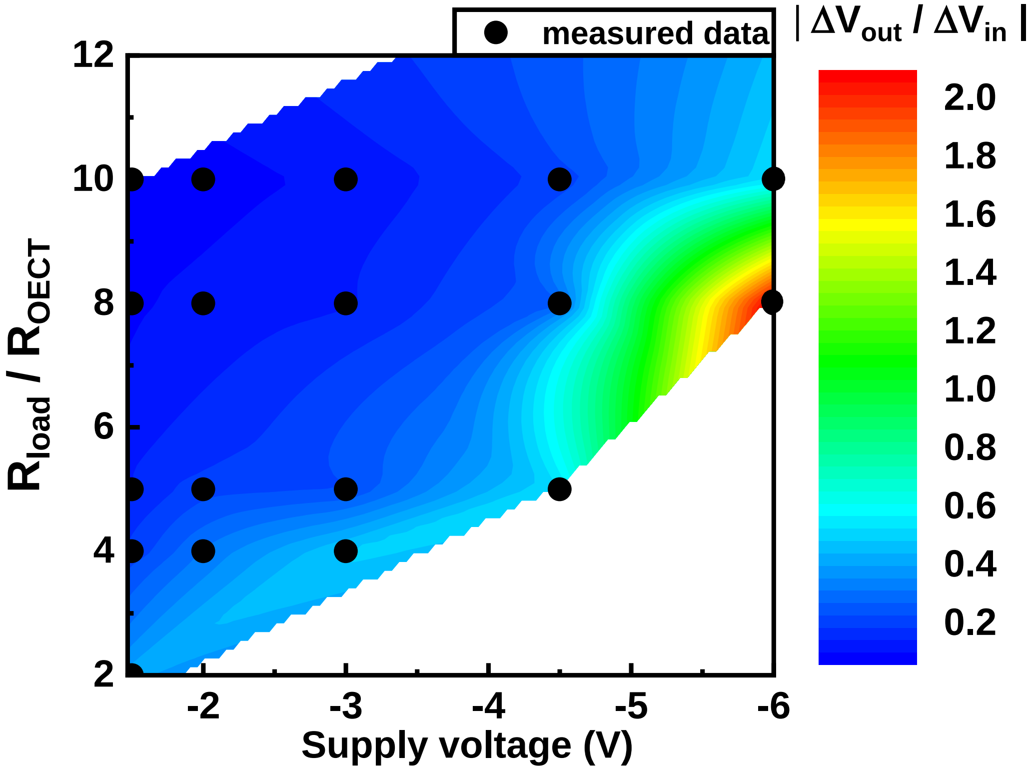

Figure 43. The color map of the voltage converting circuit at $V_G = 0$ V, with various resistance of loading resistor and various supplying voltage.

Table 3 compares the basic performance of the amplifiers consisting of a transistor and a resistor. From Table 3, we can see that because of the high transconductance and low voltage characteristics of the NMOECT. The NMOECT based amplifier can use a relatively smaller resistor and supply voltage to achieve a bigger voltage gain. By incorporating with more complex circuitry design, such as complementary circuits with N-type OECT, an even higher voltage gain can be expected.

Table 3. The performance comparison between resistor-load amplifiers.

	CNT-TFT[69]	**OTFT[70]**	**OECT (this work)**
Semiconductor	CNT	Pentacene	PEDOT:PSS
Mechanism	Field effect	Field effect	Electrochemical
V_{DD}	15 V	60 V	6 V
Loading resistor	10,000 kΩ	40, 000 kΩ	12 kΩ
Gain $\left(\frac{\Delta V_{out}}{\Delta V_{in}}\right)$	2	1.92	4.5

As discussed above, a higher supply voltage is preferable to achieve a higher gain; however, this results in a higher DC level in the output signals, which is not necessary for the electrophysiological graph, such as the electrocardiogram. Meanwhile, higher DC levels in the signals will waste the accuracy of the analog to digital converter (ADC) module, resulting in less accuracy and less signal-to-noise ratio. To reduce the DC levels in the output signals, in this work, an electronic high-pass filter is used for the NMOECT circuits.

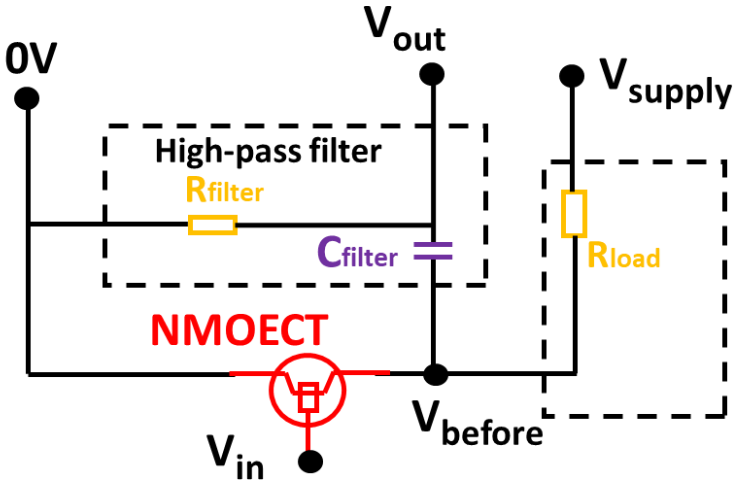

Figure 44. The schematic of the NMOECT circuits with loading resistor and high-pass filter.

The high-pass filter consisting of the series combination of a capacitor and a resistor, and the voltage across the resistor is used as an output. Before laminating the NMOECT on the skin, we first demonstrated the performance of the filter using the circuits shown in Figure 44.

In the frequency domain, the relationship between the voltage signals before and after the filter can be expressed using the following equation:

$$\mathrm{V_{out}} = V_{before}\frac{R_{filter}}{R_{filter}+\frac{1}{j\omega C_{filter}}} = V_{before}\frac{1}{1+\frac{1}{j\omega R_{filter}C_{filter}}} \tag{11}$$

If we set $\mathrm{f_0} = \frac{1}{2\pi R_{filter}C_{filter}}$, and $\mathrm{f} = \frac{\omega}{2\pi}$, then we have:

$$\mathrm{V_{out}} = V_{before}\frac{1}{1-j\frac{f_0}{f}} \tag{12}$$

The absolute value of the $\mathrm{V_{out}}$ can be represented as following:

$$\mathrm{V_{out}} = \frac{V_{before}}{\sqrt{1+\left(\frac{f_0}{f}\right)^2}} = \frac{V_{before}\frac{f}{f_0}}{\sqrt{1+\left(\frac{f}{f_0}\right)^2}} \tag{13}$$

At high frequency, $\mathrm{f} \gg \mathrm{f_0}$, then $\mathrm{v_{out}} \approx V_{before}$. While at low frequency, $\mathrm{f} \ll \mathrm{f_0}$, $\mathrm{V_{out}} \approx 0$, and the signal is cut-off. The $\mathrm{f_0}$ is defined as the cut-off voltage of the high-pass filter.

For demonstrating the characteristics of the configuration. The output voltage ($\mathrm{V_{out}}$) was measured while a 5-Hz sine wave of 20-mV amplitude was input. The experiments were performed in various supply voltages from –2 to –6 V respectively. Figure 45 shows the signals before the filter ($\mathrm{V_{before}}$), demonstrating that a higher voltage gain ($\Delta\mathrm{V_{out}}/\Delta\mathrm{V_{in}}$) could be achieved with a higher supply voltage. But the higher supply voltage also results in higher DC levels. As the output signals ($\mathrm{V_{out}}$) shown in Figure 46, the DC levels in the signals were cut off after the 1-Hz high-pass electronic filter ($\mathrm{R_{filter}} = 82\ \mathrm{k\Omega}$, and $\mathrm{C_{filter}} = 2.15\ \mu\mathrm{F}$), and a high gain with a higher $\mathrm{V_{supply}}$ was maintained, which shows the feasibility of using RC filters for cutting the DC signal output by NMOECT.

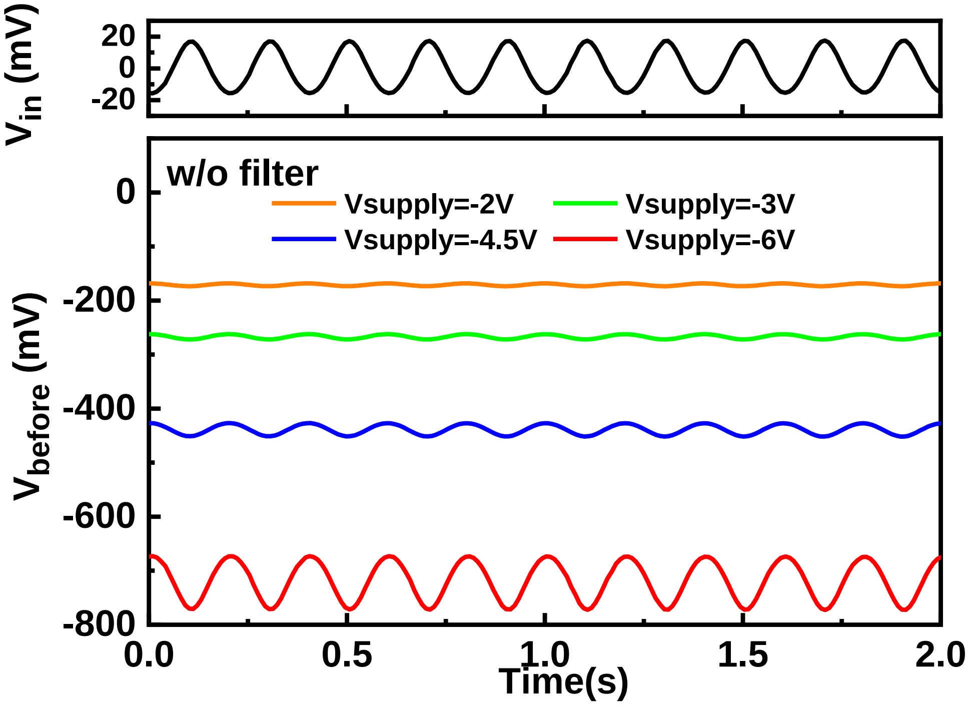

Figure 45. The input signal and output signal with various supplying voltages.

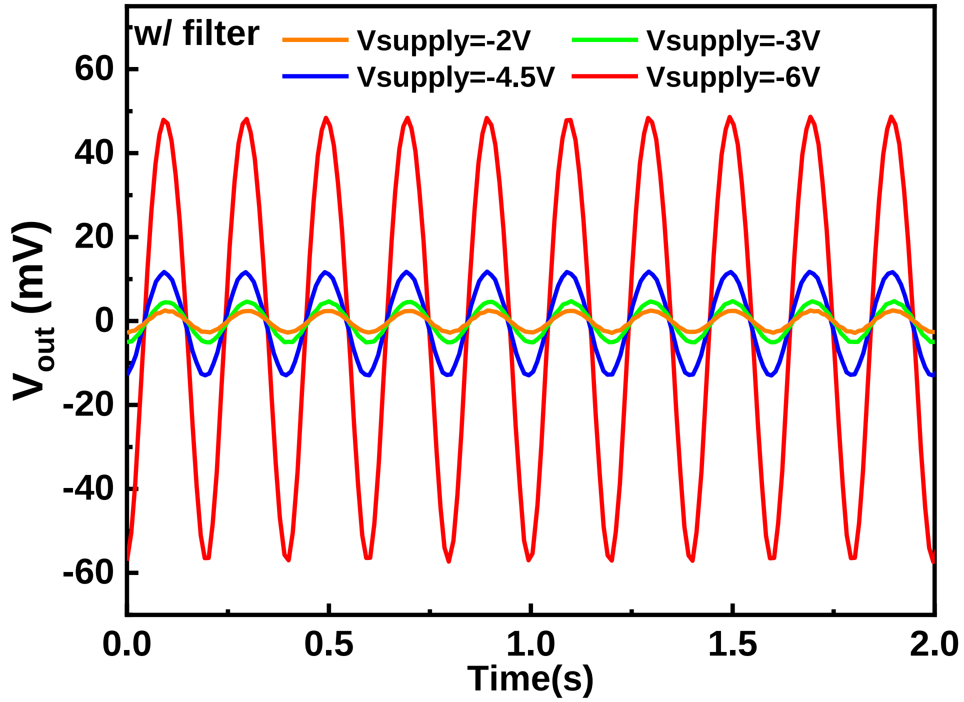

Figure 46. The output signals after the high-pass filter.

3.2 Electrocardiographic signal acquired by NMOECT

This section discussed implement the NMOECT as on-skin electrophysiological signal, the in-vivo ECG acquisition was demonstrated. The NMOECTs electrodes with only channel parts were fabricated as described in last chapter. Then, the electrodes were laminated on the skin of a healthy human volunteer (27 years old, male) to acquire the electrocardiography (ECG) signals.

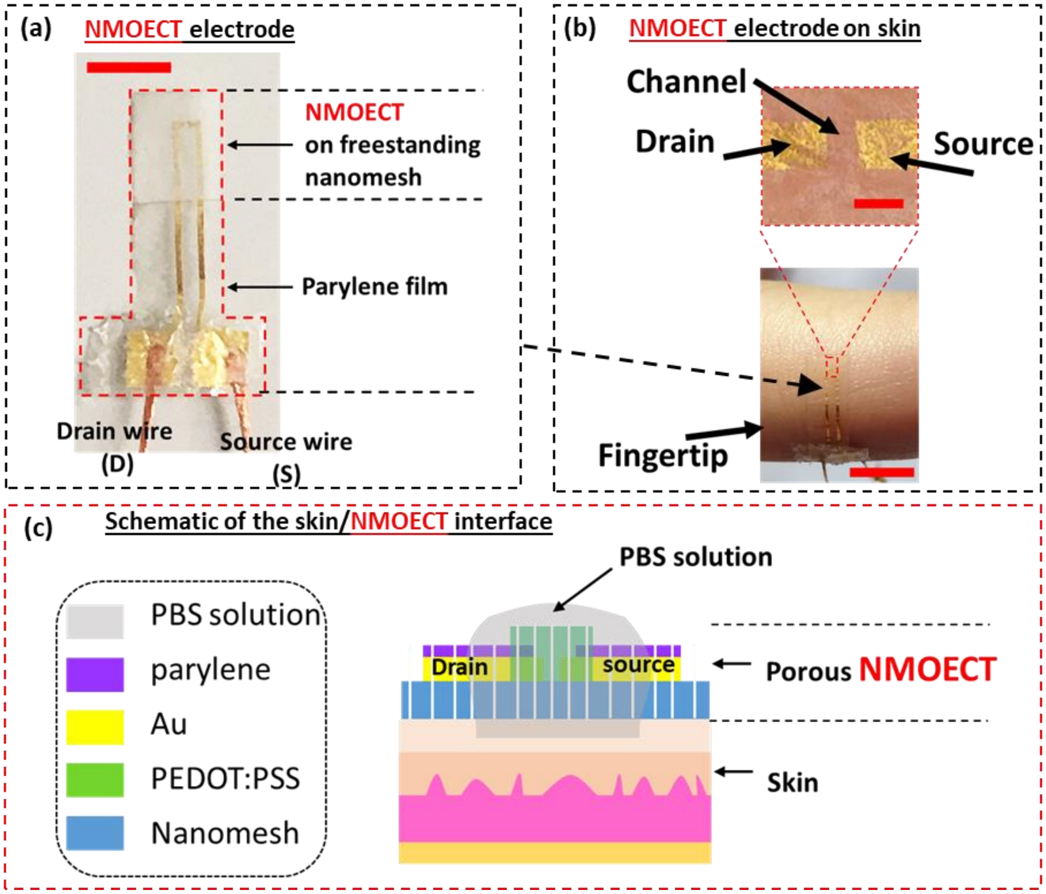

Figure 47. (a) Photograph of a NMOECT electrode prepared for on-skin ECG signal acquiring (Scale bar: 3 mm). (b) Photographs of the NMOECT electrode on the skin of a fingertip with a scale bar of 200 µm (top) and 5 mm (bottom) respectively. (c) Schematic of the interface between skin and NMOECT.

As shown in Figure 47. The electrodes are wired out to the measurement equipment using cables. Figure 47 (a) shows a freestanding NMOECT electrode connected with the Au pads. The Au pads are on the parylene film for wire bonding. The process flow of device fabrication is the same as that described in the device fabrication section. Figure 47 (b) shows the on-skin NMOECT electrodes; only the NMOECT nanomesh parts are necessary to be laminated on the skin. The ultrathin NMOECT conformably contacted and attached to the skin surface even though its surface is not adhesive. In Figure 47 (c), a schematic of the interface between NMOECT and skin is depicted; the PBS solution was used to provide ions for doping and dedoping PEDOT:PSS; the human skin works as the gate of the NMOECT, and the potential signals from the skin surface are directly loaded to the PEDOT:PSS channel via the PBS electrolyte. Before ECG acquiring, the channel part of NMOECT was laminated onto one left-hand fingertip. Then, 5μL PBS solution was dripped onto the channel part of the OECT, and the PBS penetrated to the skin/NMOECT interface due to the porous structure of nanomesh. After the configuration shown in Figure 47 (d) was set, the signals were measured by a semiconductor analyzer (Keysight B1500) using a SMU module. The sampling rate for measuring was set to 100 Hz. The measured signals were processed by digital fast Fourier transform filtering, with a band-pass filter (1-100 Hz) and a notch filter (45-55 Hz). The study protocol was thoroughly reviewed and approved by the ethical committee of the University of Tokyo (approval number KE19-33)

The schematic of circuits configuration for ECG acquiring is shown in Figure 48, where the 0-V terminal was connected to the other position on the skin using the gel electrode as the 0-V reference, which follows the lead 1 connection method in clinical applications.

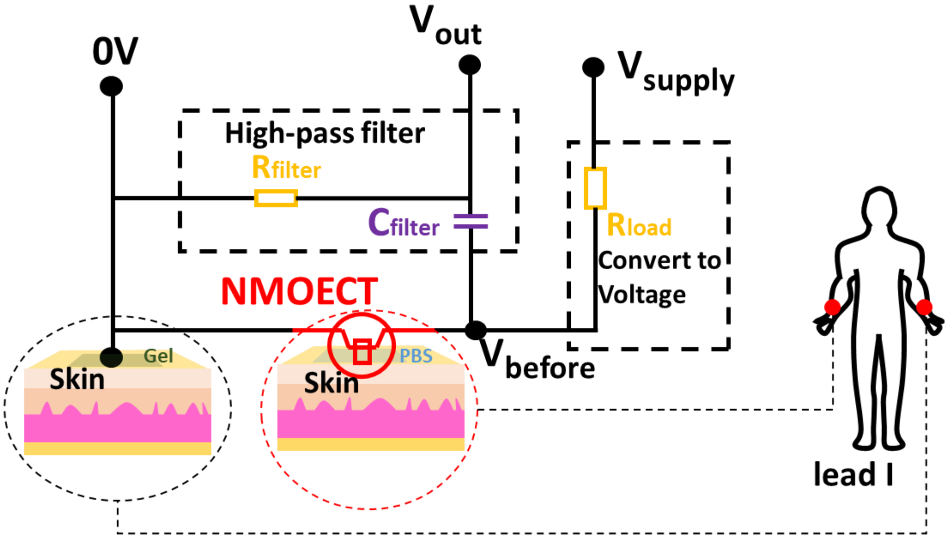

Figure 48. The schematic of the circuits configuration used for ECG signal acquiring.

To compare the signal before and after the filter, the signals before the filter was also monitored by connecting the node with the semiconductor analyzer. As characterizing results in last section, the amplitude of the small signals is dependent on the supply voltage. With a larger supply voltage, the NMOECT circuit has a higher voltage gain. The same performance was also verified when the NMOECT was used as on-skin electrodes, while the skin working as the gate electrode. As shown in the Figure 49, different supply voltage of -2 V, -3 V, -4.5 V, and -6 V were applied to the setup. In each case, the small ECG signals can be observed. The DC levels in the signals are increased with increasing of absolute value of the supply voltage, the amplitude of the small ECG signals were also increased.

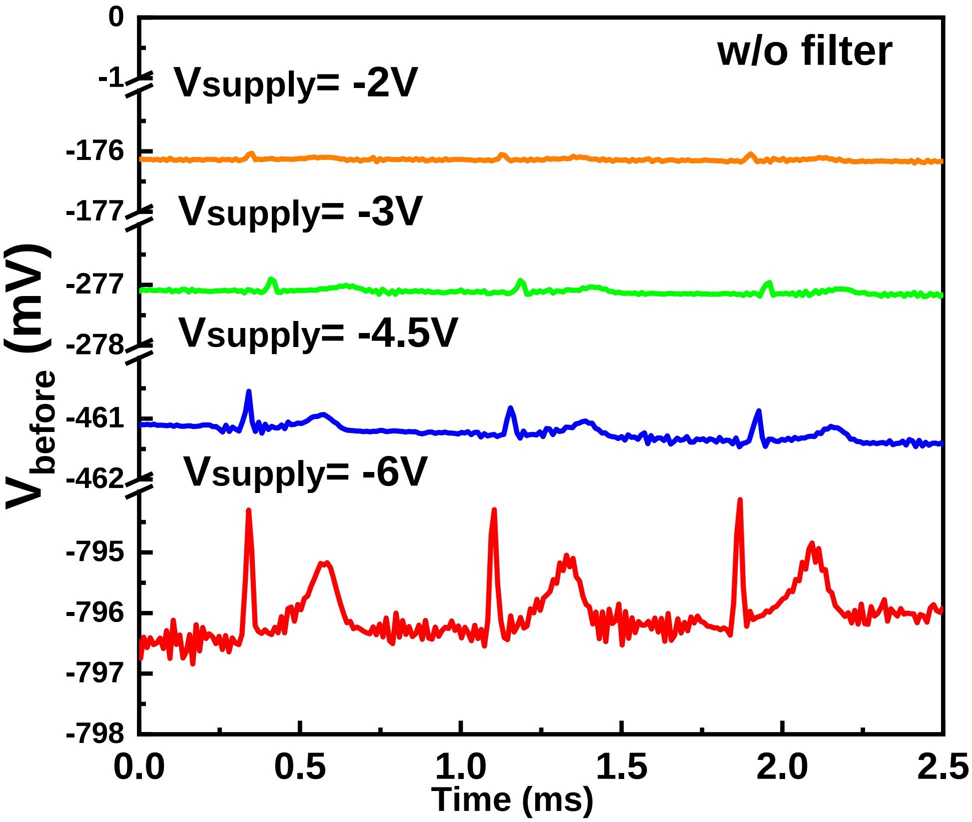

Figure 49. The acquired ECG signals with various supplying voltages before the high-pass filter.

Figure 50 shows the ECG signals after the 1 Hz filter. All the ECG peaks are around 0 V, without containing of the DC levels. The ECG signals acquired using higher supply voltage has a higher amplitude, revealing the filter is effective for cutting the DC signals. The signals after the filter shows higher signal to noise ratio. This is because without the DC signals, more digits of ADC can be used to read more accurate signals, and the noise comes from the accuracy error was suppressed.

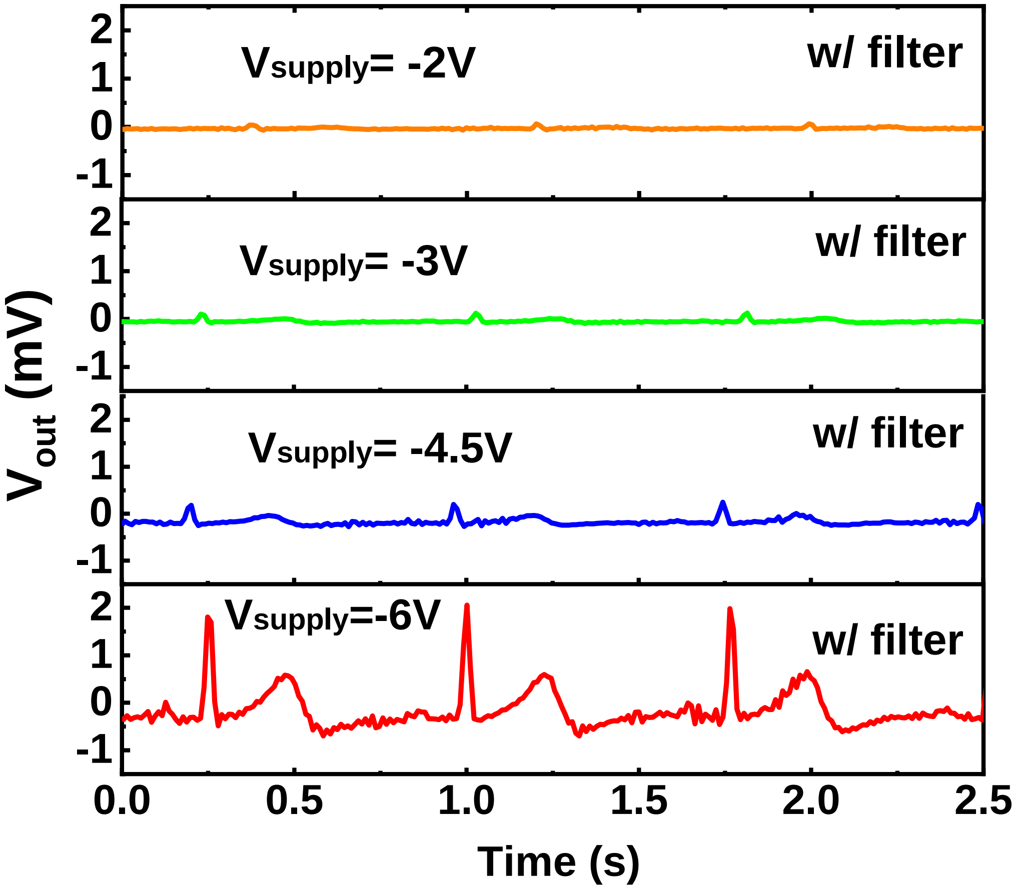

Figure 50. The acquired ECG signals with various supplying voltages after the high-pass filter.

Another benefit of using the active electrodes is the signal can be locally processed. We demonstrated the signal processing using the filters with various cut-off frequencies. The signals in different frequency ranges can be utilized to extract the features of the signals, which is widely used for diagnosis using the machine learning[71]. The filters with various cutoff frequencies (1, 10, 20, and 50 Hz) were also demonstrated by varying the resistance of R_{filter} (82, 8.2, 4.3, and 1.6 kΩ), as shown in Figure 51. According to the literature, the frequencies of the ECG wave are different, the P and T waves are 3 Hz, and the QRS wave is 20 Hz[72]. The results in Figure 51 show that, by using a 10-Hz filter, the P and T waves were suppressed, and with 20- and 50-Hz filters, the QRS peaks were also significantly suppressed. The analog RC filter was proven to effectively process the ECG signals during signal acquisition.

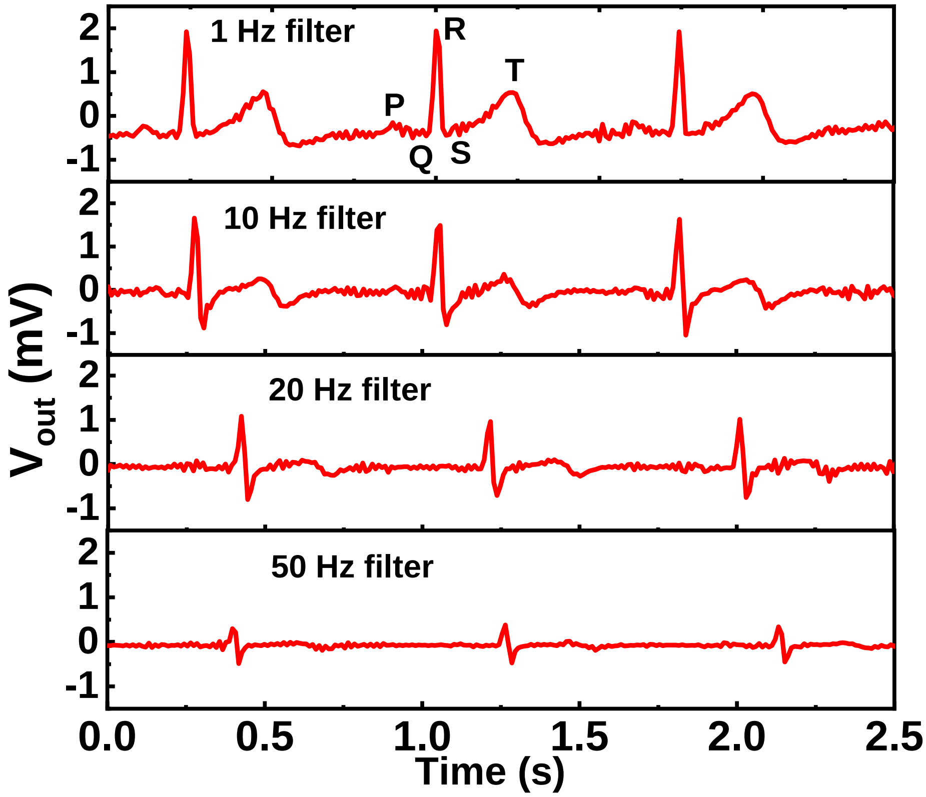

Figure 51. The acquired ECG signals with various high-pass filters with various cur-off frequencies.

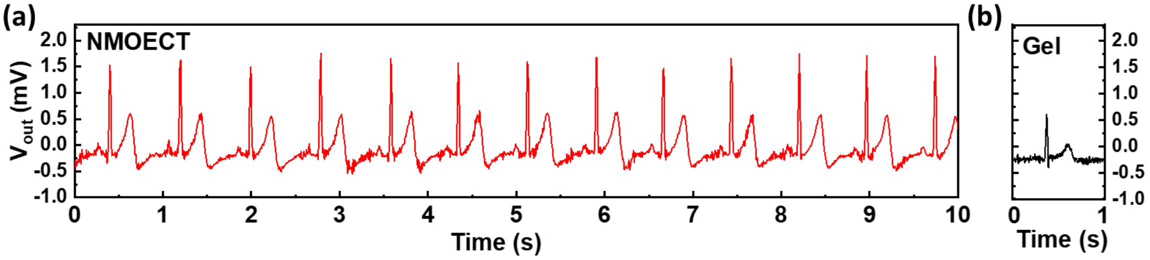

Figure 52. ECG signals acquired by the NMOECT configuration and the original signal measured by gel electrodes.

Figure 52 are the ECG signal acquired by NMOECT circuits and conventional methods using passive electrodes respectively, revealing that the ECG acquired by the NMOECT had a higher amplitude of peaks. In the case of NMOECTs, the amplitude of the QRS peak was 2.14 mV, and the standard deviation of the signal was 0.1 mV, resulting in a calculated SNR of 25.896 dB, which is higher than previously reported results. A signal with high amplitude is easier for the signal reading system; the reading speed is related to the accuracy of the analog to digital converter. Signal with higher amplitude allows less digits of the converter to read the signal.

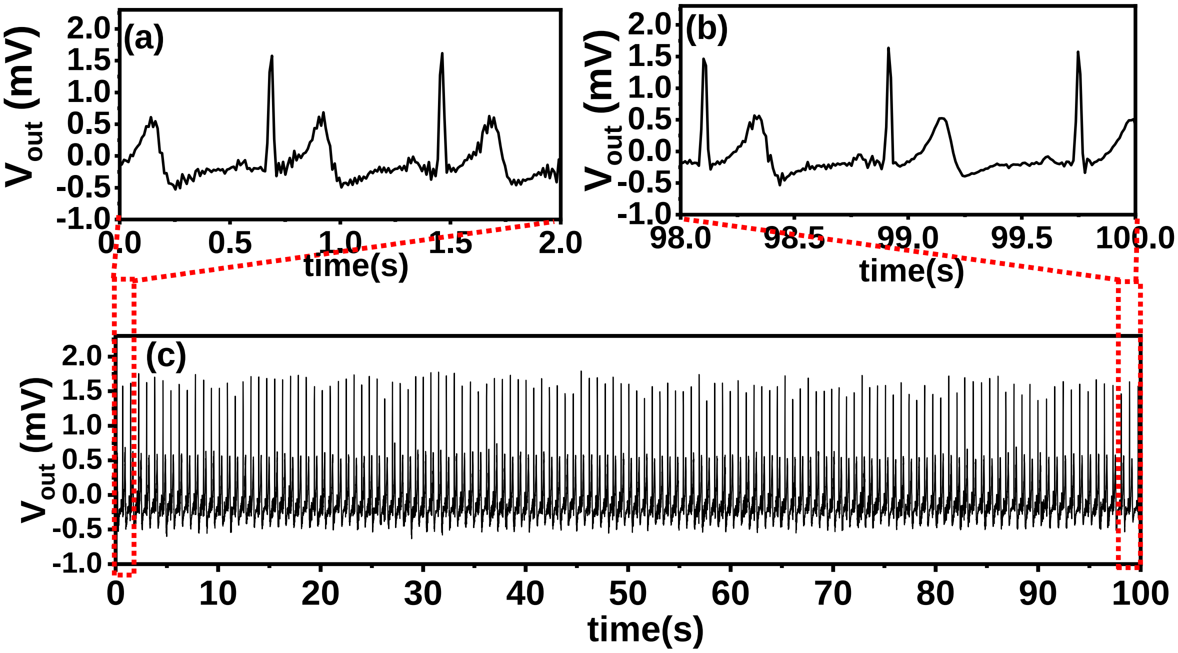

Figure 53. Continuous 100-second ECG signals measured by NMOECT. (a) The ECG signals of first two seconds, (b) The ECG signals of the last two seconds, and (c) total 100 seconds ECG signals.

The NMOECT circuit configuration can repeatable acquire high-quality signals, as shown in Figure 53; the signals remained stable after more than hundreds of ECG peaks.

3.3 Wireless signal measurement of the NMOECT

The wireless signal monitoring is the necessary for the daily life wearable healthcare system[1, 65, 73]. The wireless signal transmission eliminated the burden of wearing the monitoring equipment and cables. Using wireless signal transmission, the users can monitor the signals using a mobile device, such as smartphone, pad, and so on. In this study, a simple solution for wireless transferring the electrophysiological signal acquired by NMOECT electrodes to the mobile device is introduced. A microcontroller platform and Bluetooth module was used for the signal control and data transmission. A high accurate analog to digit converter (ADC) with 14-bit accuracy. The general schematic of the configuration is shown in Figure 54.

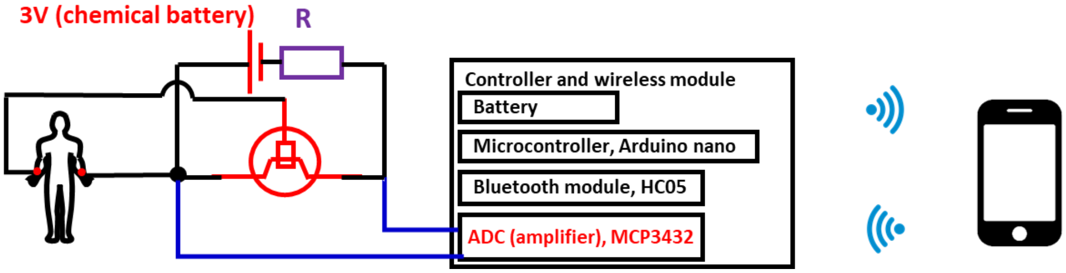

Figure 54. The schematic of the equivalent setup for wireless transmission of the electrophysiological signal acquired by NMOECT.

In this setup, as we discussed in previous section, most of the microcontrollers can only read the voltage signals. To convert the currents signals of NMOECT to the voltage signal, the NMOECT is connected with a serial resistor. The circuit is powered by two chemical batteries, which provides 3 V voltage supply. The chemical battery was used because of its stable voltage output with ultra-low noise. It is very important for our setup, otherwise the noise comes from the voltage supply will overwhelm the electrophysiological signal acquired by the NMOECT. The microcontroller used in this study is Arduino Nano, which has a small size. The Arduino Nano is connected with the ADC module (MCP3424) and the Bluetooth module (HC-05), and controlling the signal reading and transmission. A mobile charger can be used to provide a USB power supply for the Arduino board.

The high accuracy ADC module (MCP3424) was used for signal reading, which can provide a programmable differential amplification of the signal and a maximum 18-bit reading resolution. The resolution is dependent on the sampling speed. Higher resolution results in low sampling rate. Considering the sampling rate and accuracy for the electrophysiological signals, 14-bit resolution with a sampling rate of 60 samples per seconds is used. In this setup, a minimum signal amplitude of 15.6 µV can be acquired. The ADC module communicate with the microcontroller using the Inter-Integrated Circuit (I2C) bus.

A simple procedure of signal reading is described here. First, the voltage signal comes from the NMOECT is read by the MCP3424 module. Then the microcontroller read the signal read by the MCP3424, and stored as variable. Then the data is transmitted from the Arduino Nano to HC-05 module using serial port protocol (SSP). The HC-05 module then send the signal to the smartphone device that was paired with the HC-05 module using the Bluetooth protocol.

In the future, a printed circuit board on the flexible substrate can integrate all these elements together and make the recording system more compact.

Chapter 4: Porous solid-state polymer electrolyte (SPE) for organic electrochemical transistor

4.1 Introduction of the solid-state polymer electrolyte

Electrolyte is a media that contains the ions. The ions can move inside the electrolyte and support the function of the ionic devices. The ionic devices are widely used in the energy storage devices such as batteries[74, 75], solar cells[76, 77], and super capacitors[78, 79]. Ions have high mobility in the liquid solutions, the conventional electrolyte for the applications are usually liquid electrolyte. However, the using of liquid electrolyte will cause some hazard such as electrolyte leak, the production of harmful gases, reaction with the electrode materials, and so on[80]. The solid-state polymer electrolyte is nonvolatile, and stable, which attracts the attention of researchers. The solid-state polymer electrolyte (SPE) is one kind of solid state electrolyte. The use of polymer materials enables the electrolyte with flexibility, transparency, and light-weight [81]. Another advantage of the SPE is the easy fabrication process. Thin film can be formed by the solution process, and a wide electrochemical windows can be utilized[80].

Electrolyte is key component for the OECT, providing ions for doping and de-doping of the semiconductor channels. Using the SPE for OECT enables the application of OECT in the dry environments[49, 56, 58, 82-89]. The OECT embedded with SPE can eliminate dysfunction when the liquid solution is evaporated. Researchers have demonstrated the active on-skin electrode using the OECT embedded with bio-degradable SPE materials; the continuous ECG monitoring was successfully achieved [42] as shown in Figure 55(a). The tactile sensor that uses the OECT to sense the distribution change of ions caused by the loaded pressure has also been demonstrated[85]; high sensitivity of the sensor enables it to detect the subtle pressure signals, rendering a high precise machine-environment interface, as shown in Figure 55 (b). The easy processability of SPE and OECT enables the large-scale printing, the customized and quick device fabrication can be possible.

Usually, the SPE is formed by dissolving the salt into polymer. Both the synthetic and natural polymers have been developed to be the polymer of the SPE. Compared with the liquid electrolyte, the crystallized solid polymer reduces the mobility of the ions, which results in lower ion conductivity of the SPE. The SPE based devices usually have lower performance[82]. A proper choose of SPE materials is important to get sufficient performance of the target application.

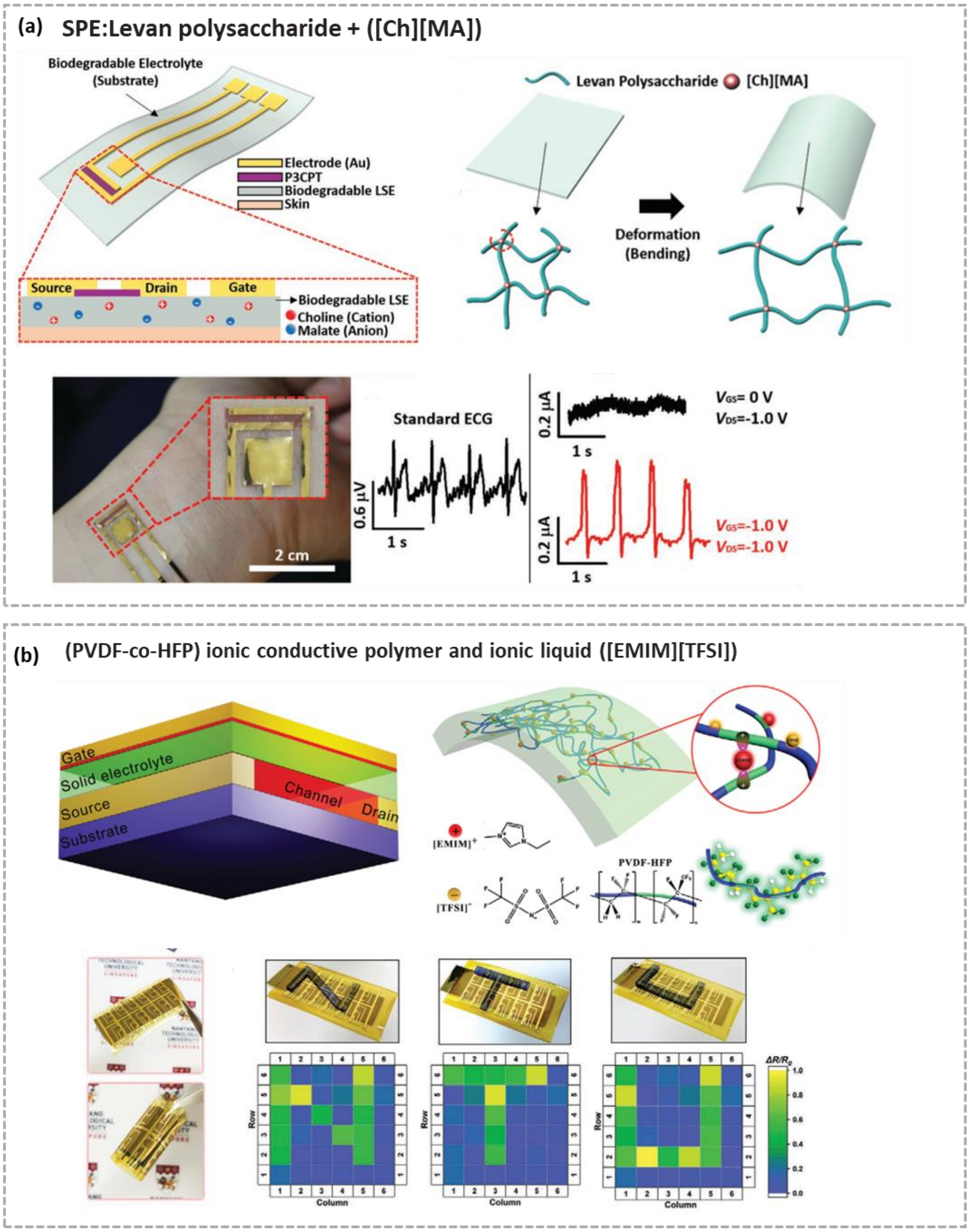

Figure 55. (a) OECT embedded with solid electrolyte for electrophysiological signal monitoring (copied from reference[42]). (b) OECT embedded with solid electrolyte, used as tactile sensor(copied from reference[85])

There are many candidates of polymer materials and salt that can be used to form SPE with high ion conductivity. Considering using the SPE materials for the on-skin application, the bio-compatibility and the possible degradation caused by the SPE materials is concerned. As shown in Table 4, the PVA/KOH is in high ion conductivity[90-92]. It is the most commonly used materials system as the SPE. However, the KOH will cause the significant degradation of the PEDOT:PSS. The conductance of the PEDOT:PSS channel degraded several orders after the contact with the PVA/KOH solution, which reduced the transconductance of OECT and makes it not suitable as SPE materials for OECT.

Table 4. The comparison of typical SPE materials.

Materials	**PVA/KOH[93]**	**PEO/LiN(CF_3SO2)$_2$[74]**	**Chitosan/$NaCF_3SO_2$[94]**
Flexibility	Yes	Yes	Yes
Ion conductivity	10^{-2} S cm^{-1}	2.6×10^{-4} S cm^{-1}	2.4×10^{-4} S cm^{-1}
Not damage OECT	No	/	Yes
Biocompatibility	No	No	Yes
Gas-permeability	No	No	No

Usually, the lithium based salts are commonly used as salt for the SPE due to its small atomic mass, and it has made a lot progress for the Li-battery[74, 75, 95]. But it is dangerous of using the lithium salt for human skin interface, because the reaction of lithium salt might produce toxic products, which is dangerous for the human. The natural materials based polymer can also be used for building the SPE with sufficient electrolyte properties. As shown in Table 4, the chitosan based SPE[96, 97] shows comparable performance with other SPE materials. Chitosan is a kind of natural polymer synthesized from chitin shells of shrimp and other crustaceans[98]. The chemical structure of the chitosan is shown in Figure 56. Its high bio-compatibility renders the application for many medical use, such as scaffold of medicine[99].

However, gas-permeability, is also limiting the application of these devices to the practical on-skin application. Developing the gas-permeable NMOECT embedded with gas-permeable SPE can be a possible candidate for future wearable or on-skin applications based on OECT.

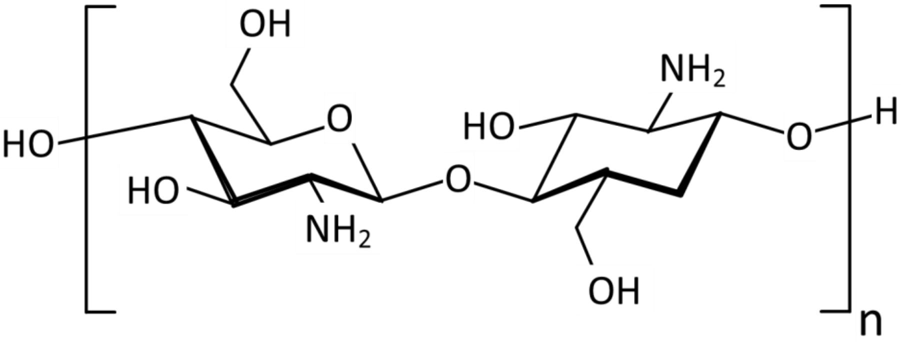

Figure 56. The chemical structure of the chitosan.

In this study, the porous chitosan based electrolyte was developed to be embedded with the NMOECT, to make the gas-permeable electrolyte embedded OECT. We developed the porous chitosan SPE based on the material composition proposed by Aziz et al.[96, 97]. The sodium based salt, sodium trifluoromethanesulfonate (NaTf) was used as the salt in the chitosan polymer. In this study, the fabrication process to form the porous structure of the SPE and the NMOECT embedded with the porous SPE was developed, enabling the gas-permeability of solid electrolyte embedded OECT as on-skin active electrodes. The fabrication method of the porous chitosan/NaTf SPE will be discussed in the following parts.

4.2 Formation of porous solid-state polymer electrolyte film

The freeze-drying process [100] was utilized to form the porous structure of SPE film. The freeze-drying process utilizes the low temperature to freeze the sample, and then sublimate the ice-state solvent in low pressure[101]. Under the low pressure environment, the ice-state solvent directly transferred from solid state to gas-state, then the original shape of the solute can be maintained[99].

The formation processes of the porous SPE is shown in Figure 57. First, the SPE solution was made by mix 3%wt chitosan powder into 2%wt acetic acid solution. Higher weight concentration of chitosan results in high viscosity, which is difficult to process. The solution was stirred using magnetic stirrer for 24 hours for fully dissolving the chitosan. After that, the solution was standing for another 15 hours to eliminate the air bubbles, and a uniform and transparent chitosan solution was made. Then the 3%wt NaTf and 3%wt glycerol were added into the chitosan solution and stirred for another 6 hours to totally dissolve the solute. Finally, the solution was standing for another 15 hours to remove the air bubbles in the solution.

After the solution was made, the solution was coated onto the substrate by using a syringe with a 18G needle. The sample was placed in a freezer (-20°C) for 15 hours right after coating. The low temperature can change the liquid solution to the solid state.

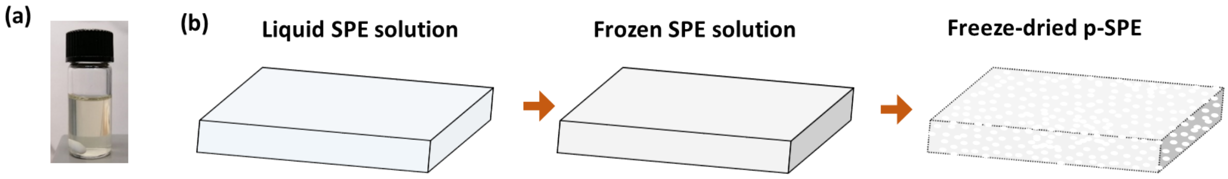

Figure 57. The freeze dry process to make porous SPE film. (a) The SPE solution. (b) The freeze dry process.

After the solution was frozen, the sample was transferred into the chamber of a freeze dryer. The chamber was quickly vacuumed to less than 5 Pascal within 5 minutes. A heater beneath the holder of the sample increased the temperature of the sample in low pressure environment, which directly change the solid-state solvent to the gaseous state, meanwhile, the chitosan was kept in its shape in the low-pressure environment. After 15-hours freeze-dry process, the solvent was totally dried and the porous SPE film was formed.

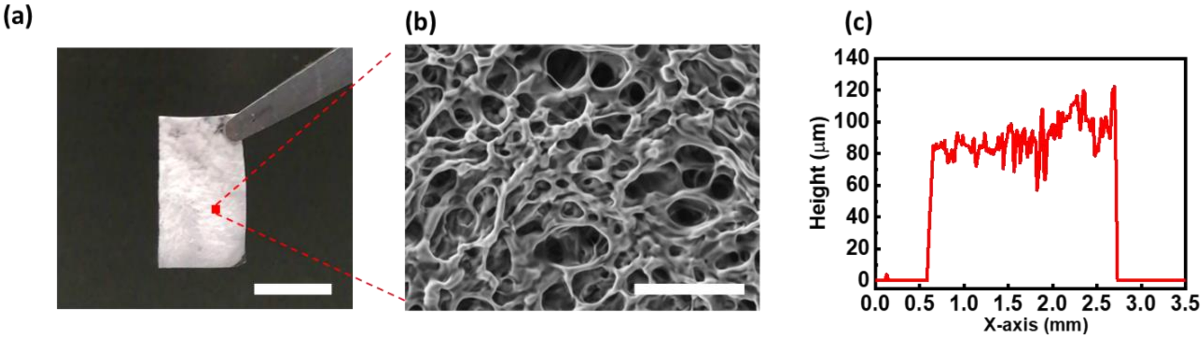

Figure 58. (a) The fabricated free-standing SPE film (scale bar: 5 mm). (b) The SEM image of the SPE film, showing the porous structure (scale bar: 50 µm). (c) The profile data of the SPE film.

Figure 58 (a) shows a free-standing freeze-dried porous SPE film, which shows white color. Figure (b) shows the SEM image of the porous SPE film, a porous structure can be observed, which allows the gas-permeability. The thickness of the film was checked by a profiler, as the results shown in Figure 58 (c), the average thickness of the porous SPE is 90.5 μm, with a standard variation of 11.6 μm.

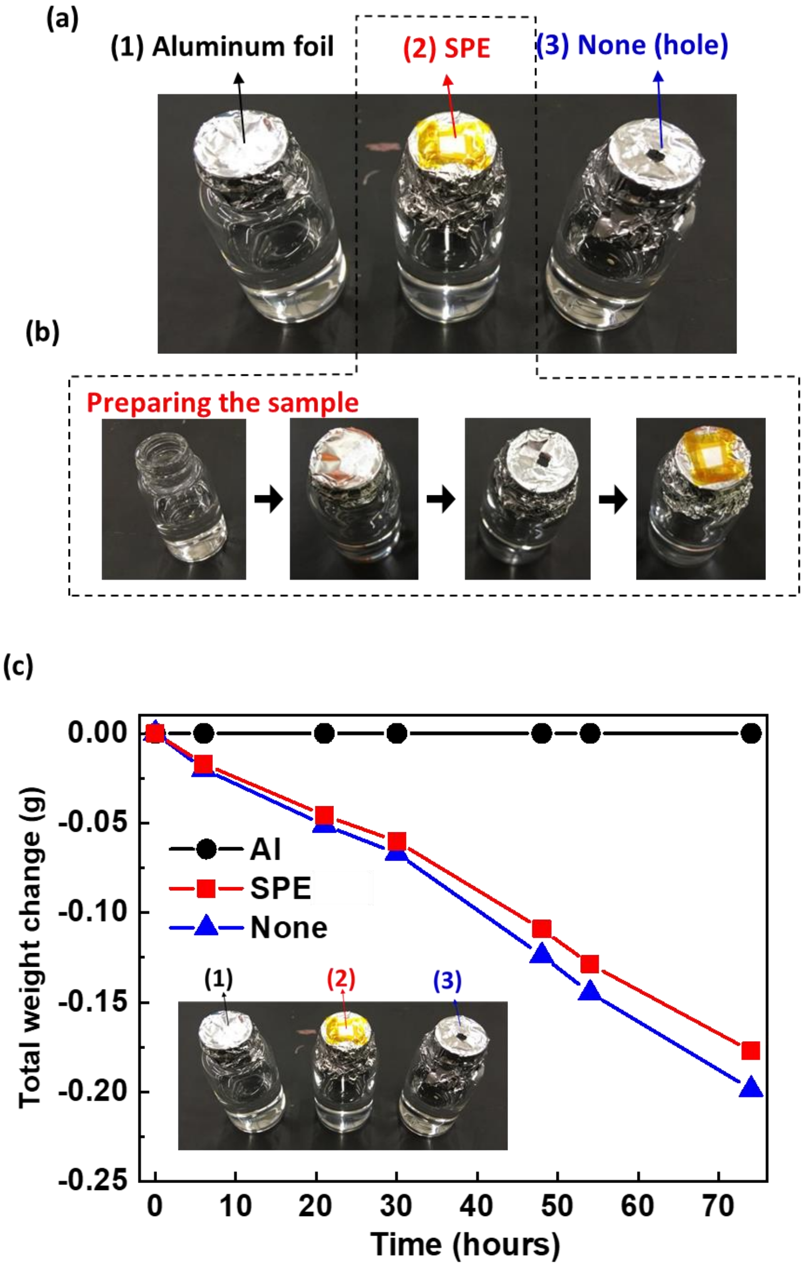

Figure 59. The vapor penetration experiments. (a) The photo of three bottles containing water and covered with (1) aluminum film (2) porous SPE and (3) nothing. (b) The total weight loss versus the time.

To check the gas-permeability of the porous SPE film. The vapor penetration experiments were performed. As shown in Figure 59 (a), three bottles containing with same amount of water were covered with aluminum foil, porous SPE, and nothing respectively. The bottle covered with porous SPE was made as shown in Figure 59 (b), the porous SPE was covered on the aluminum foil with a hole and sealed by polyimide tape. Figure 59 (c) shows the total weight change of each bottle against the time. Bottle (2) and (3) shows similar amount of water loss due to the water vapor penetrate to the open atmosphere. The results suggest that the porous SPE is in good gas-permeability as the open bottle.

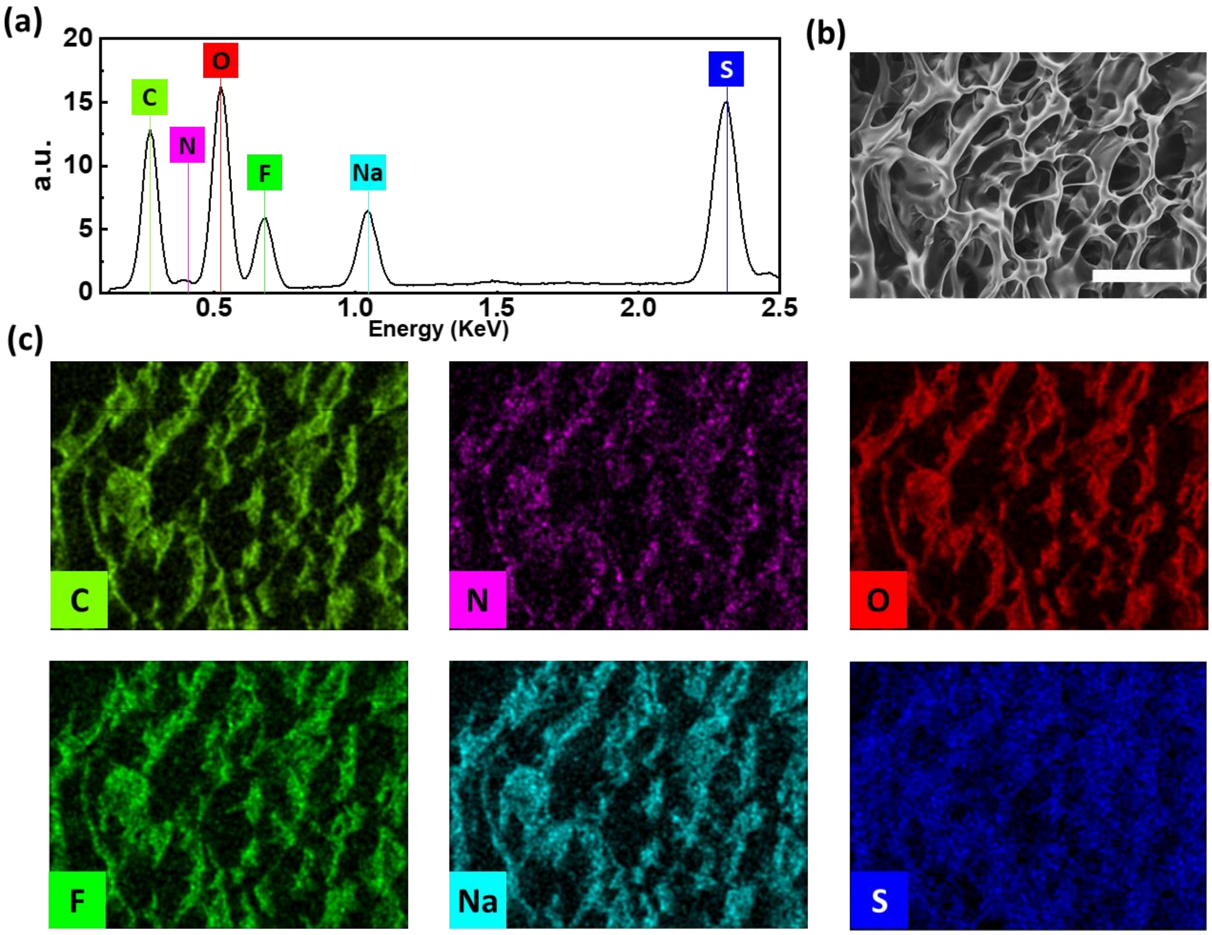

Figure 60. (a) EDX spectrum of the porous SPE film. (b) The observed sample area. (Scale bar: 100 µm). (c) The distribution of each element in the observing area.

To characterize the chemical composition of the porous SPE, SEM-EDX (energy-dispersive X-ray spectroscopy) mapping was performed. Figure 60 (a) is SEM photo of the characterizing region. The spectrum in Figure 60 (b) shows the existence of Na, F, S, which is the main element of the NaTf. The N comes from the chitosan. The C, O comes from both the chitosan and NaTf, as well as the glycerol. The color mapping of each element in Figure 60 (c) shows the elements are homogeneously distributed in the porous SPE.

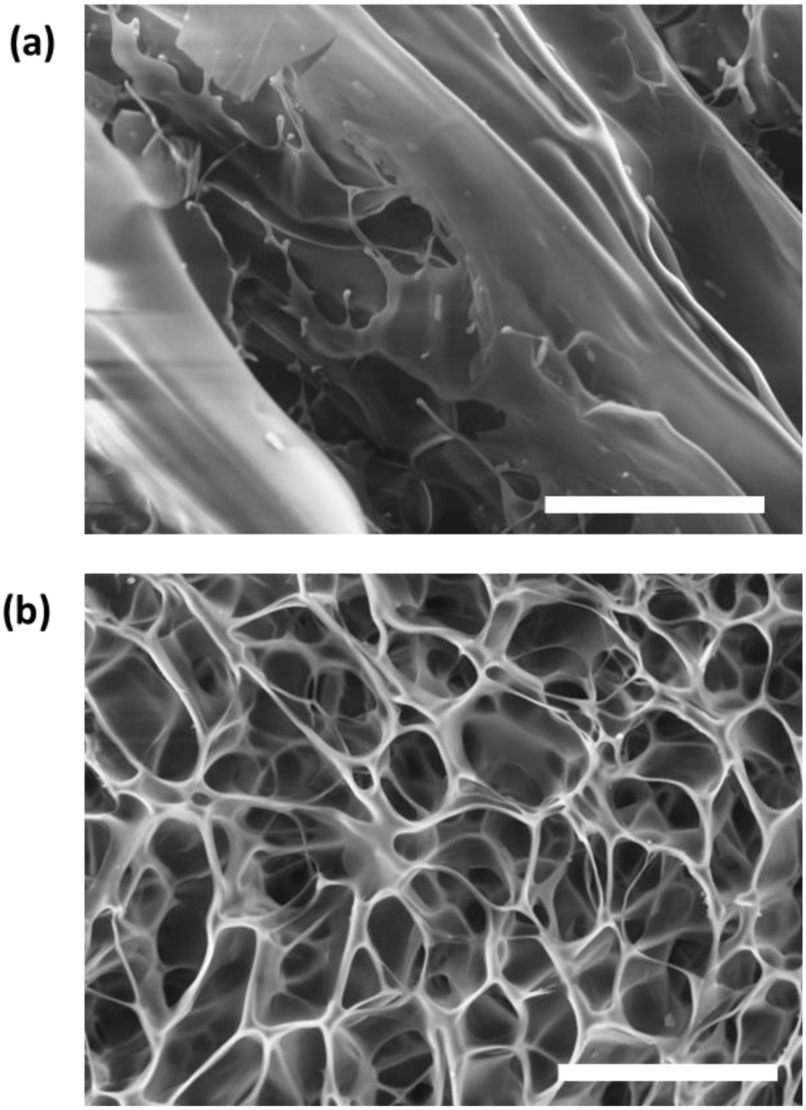

Figure 61. SEM images of (a) freeze-dried 1%wt chitosan, and (b) freeze-dried 3%wt chitosan (Scale bar: 100 µm).

The composition of the SPE solution in above results has been optimized to make the film in enough porosity and ion conductivity that can support the function of OECT. In this study, before we got the optimized results, the study to compare the morphology of the SPE film with various concentration of chitosan, ion, and glycerol were investigated. The following parts will discuss the optimizing experiments of the porous SPE by checking the SEM morphologies.

Figure 61 shows the SEM image of the porous SPE film with a concentration of chitosan of 1%wt and 3%wt, respectively. The 3%wt chitosan porous SPE film shows more uniformed distribution of the porous structure. Meanwhile, high chitosan concentration provides more amount of polymer skeleton for ion, which is better to be used as electrolyte for OECT. However, a higher concentration of chitosan makes the solution in high viscosity, which is difficult to coat and transfer. In this study, 3% chitosan solution was chosen for SPE solution preparation.

The ion concentration of the SPE solution also has effect on the morphology of the porous SPE film. According to the literature[96], relative high concentration of the doping salt provides better ion conductivity of the SPE. However, with too high salt concentration, the properties of SPE is closer to the salt crystal, which conversely reduces the ion conductivity of the SPE. To optimize the performance of the porous SPE, the SPE solution with various concentration of NaTf were made. And the identical fabrication process using these solutions were processed to make the porous SPE film. The SEM microscopic was utilized to check the structures. The morphologies of the SPE with various NaTf concentration from 0%wt to 6%wt are shown in the Figure 62. The results suggest that SPE with higher NaTf concentration maintains porous structure, however, the diameters of the chitosan skeleton expended comparing with the less salt concentration cases.

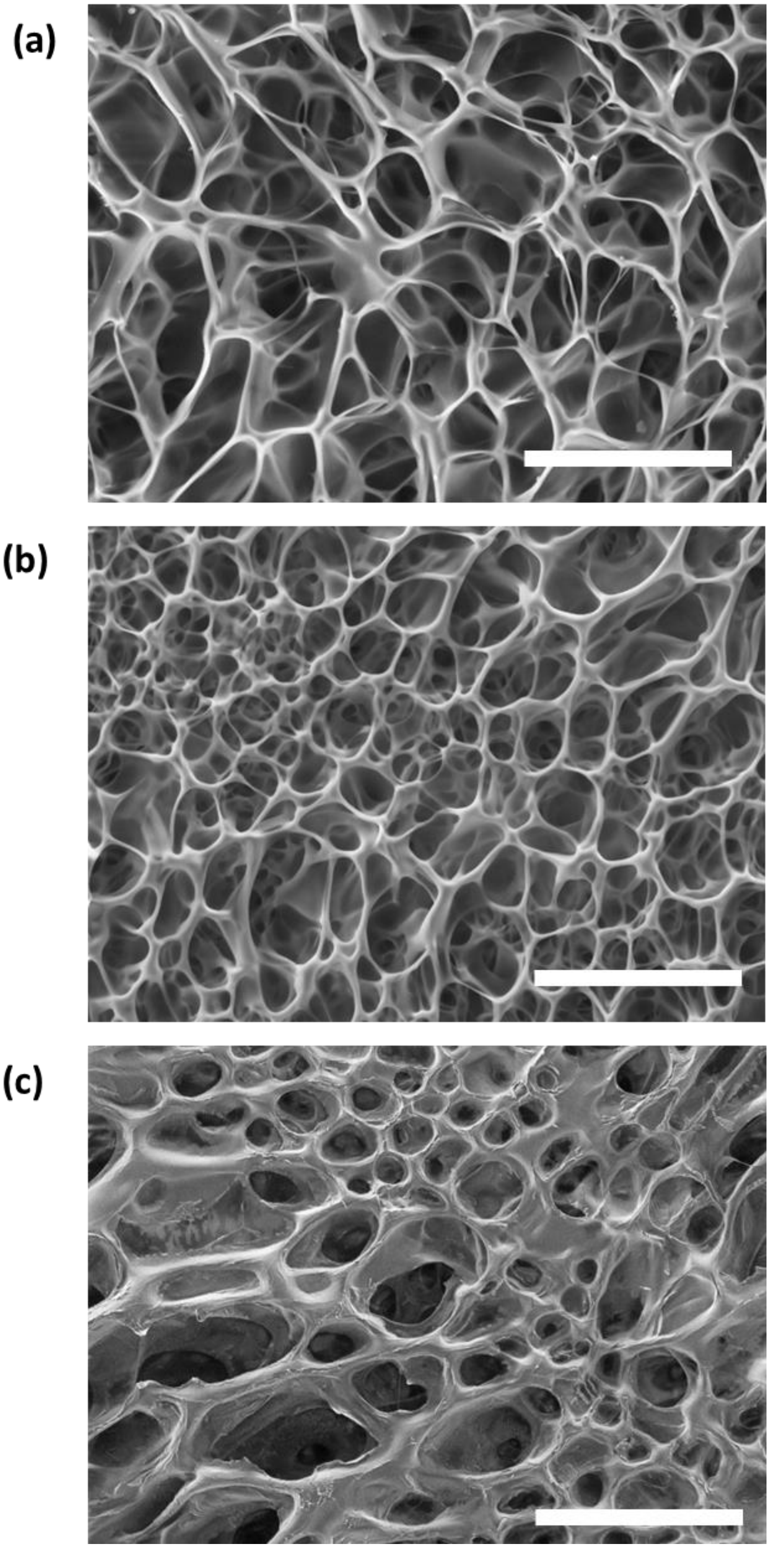

Figure 62. SEM images of freeze-dried 3%wt chitosan with (a) 0%wt NaTf, (b) 3%wt NaTf, and (c) 6%wt NaTf. (Scale bar: 100 µm)

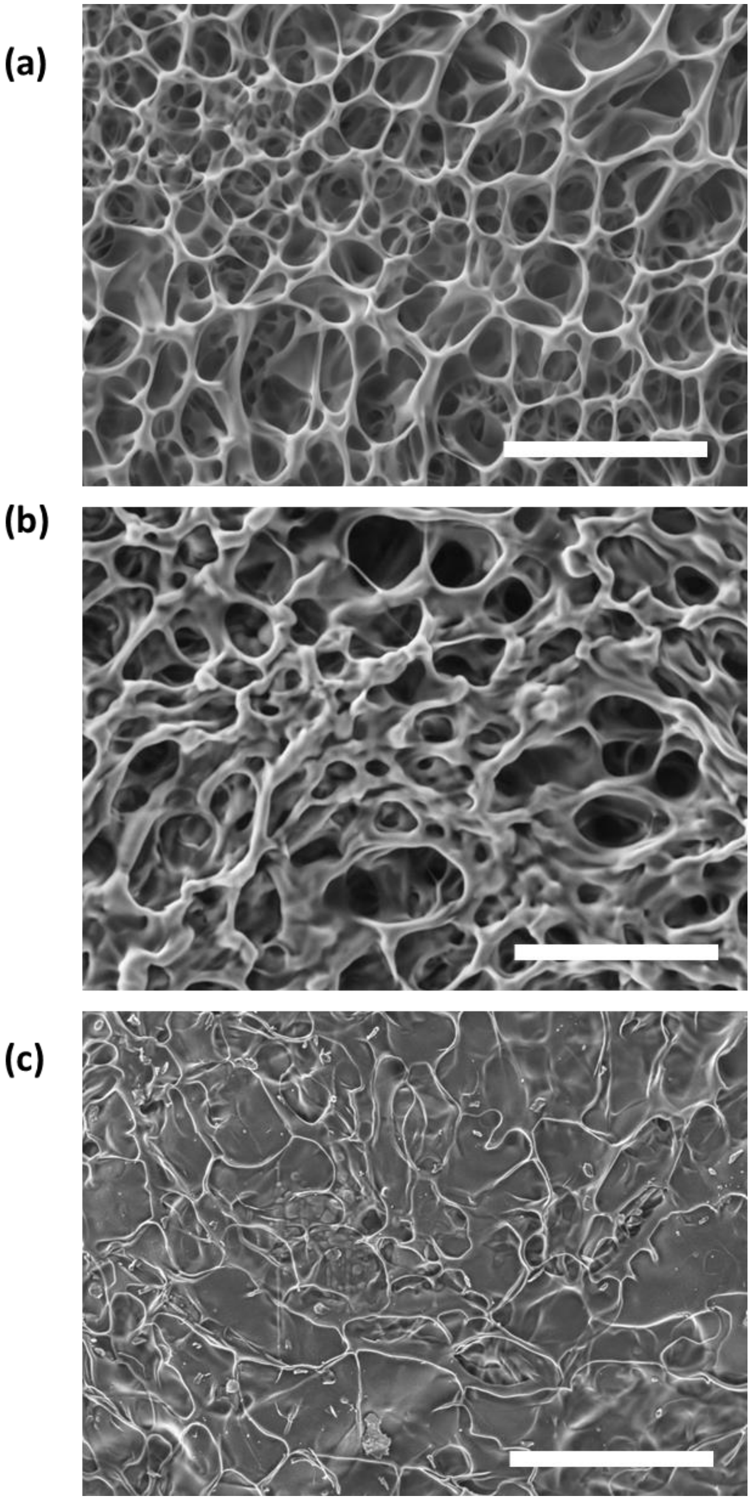

Figure 63. SEM images of freeze-dried 3%wt chitosan mixed with 3%wt NaTf with (a) 0%wt glycerol, (b) 3%wt glycerol, and (c) 6%wt glycerol. (Scale bar: 100 µm)

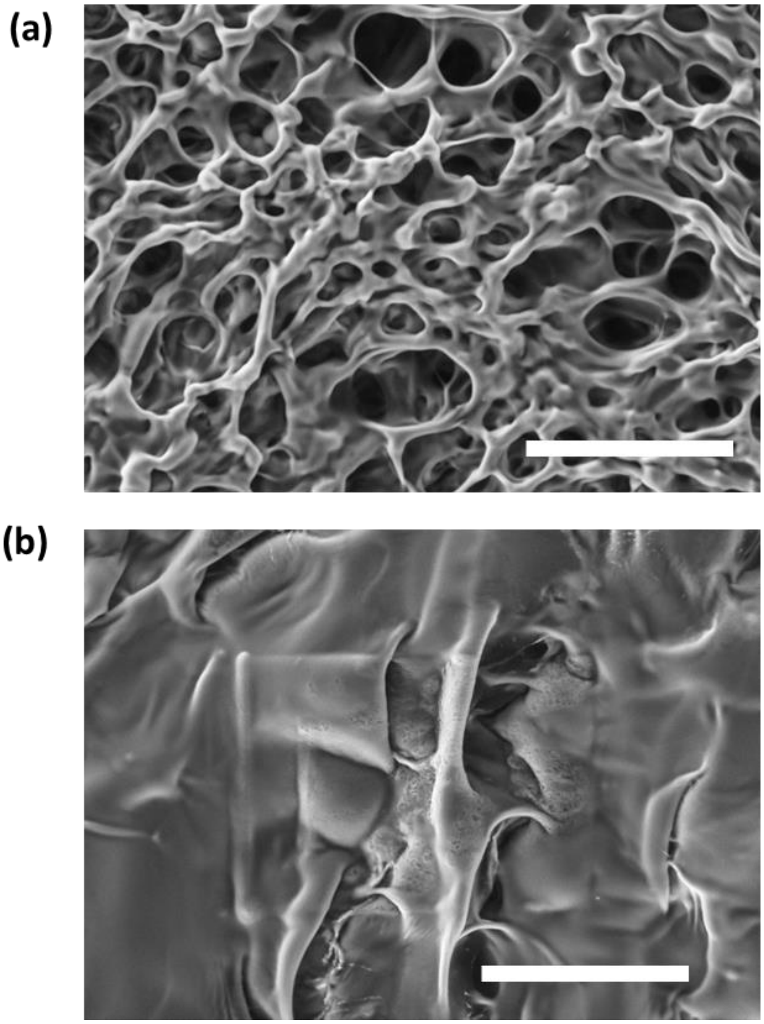

Figure 64. SEM images of freeze-dried 3%wt chitosan with 3% glycerol with various amount of NaTf. (a) With 3%wt NaTf. (b) With 6%wt NaTf. (Scale bar: 100 µm)

In this study, the glycerol is added to the SPE solution to enhance the ion conductivity of the SPE film in the low humidity environment, as well as improve the softness of the SPE film[98]. Glycerol kept stored in the SPE during the freeze-dry process. So the glycerol in the SPE system working as non-volatile solute after the dry of water[98]. A proper amount of glycerol can make the SPE works for a long-term period. Figure 63 shows the SEM morphology of the porous SPE film with various amount of glycerol from 0% to 6%wt respectively. A 3%wt glycerol makes a little deformation of the porous SPE film, and the porous structure can be maintained. However, a higher glycerol concentration of 6%wt makes the porous structure degraded, the structure is more close to the continuous film. The reason is that during the freeze dry process, the chitosan and NaTf kept being dissolved in the glycerol, so the porous chitosan scaffold cannot be formed even the water was freeze dried. To keep the porous structure and confirm good ion conductivity of the SPE film after freeze dry, 3%wt glycerol was added to the SPE solution for other experiments.

As mentioned above, the higher concentration of NaTf broke the structure of chitosan, making the system more similar to crystal salt, which also leads to the failure of forming porous chitosan scaffold. The phenomenon is more obvious when the glycerol was added to the SPE solution. After the implement of glycerol, higher concentration of NaTf results in worse morphology of the SPE film, as shown in Figure 64. The 6% wt NaTf SPE solution with 3%wt glycerol shows almost no porous structure. To keep the porous structure, the concentration of NaTf was kept to be 3%wt in the application of being embedded with NMOECT.

4.3 NMOECT embedded with porous SPE

To fabricated the whole gas-permeable solid-state polymer electrolyte embedded OECT, the porous SPE formation process is implemented onto the NMOECT, as the schematic illustrated in Figure 65 (a), which can be dissected to be two parts, the NMOECT and the porous SPE. The fabrication process of the porous SPE discussed in previous sections is implemented using the NMOECT as substrate. First, the NMOECT was firstly fabricated as described in the chapter 2. The channel part of the OECT with PEDOT:PSS channel, Au drain/source electrode, and parylene encapsulated wire are formed on the fibrous nanomesh substrate. For the NMOECT for electrical characterization, an in-plane gate in the structure of PEDOT:PSS/Au nanomesh was also fabricated, used as the electrode to load the signals from the gate. Then, the SPE solution (3%wt chitosan, 3%wt NaTf, 3% wt glycerol) was made and coated onto the front side of the NMOECT. The NMOECT coated with SPE solution was placed in the refrigerator with -20 ℃ for 15 hours. After the SPE was frozen on the NMOECT. It was transferred to the chamber of the freeze dryer quickly. The device was freeze dried for another 15 hours in the pressure of less than 5 Pa, and the temperature is -90 ℃.

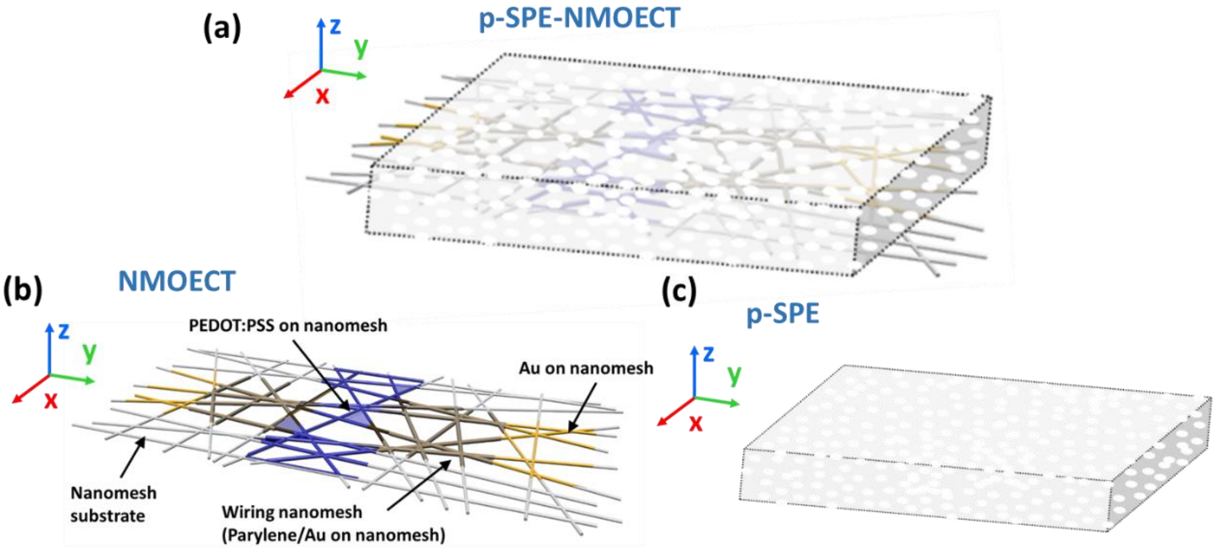

Figure 65. Schematic of the OECT embedded with porous SPE. (a) The illustration of the whole device, which can be dissected into two parts: (b) The NMOECT, and (c) The porous SPE.

Figure 66 (a) show a NMOECT with an in-plane gate. The gate is used for loading signals during the transistor characterization. Figure 66(b) shows the NMOECT embedded with the porous SPE. As described in Chapter 2, the parylene frame was utilized as supporting frame for manipulating the fibrous device during the fabrication and characterization. The white part on the device is the porous SPE. The supporting parylene frame was also cut to make the channel and gate parts gas-permeable, which will be attached to the skin surface.

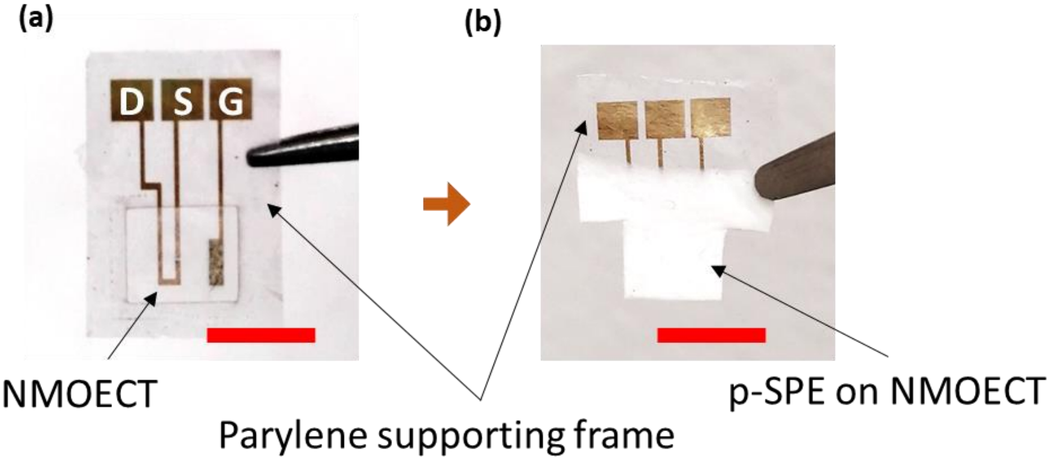

Figure 66. (a) NMOECT with parylene as supporting frame (scale bar: 5 mm). (b) porous SPE embedded NMOECT (scale bar: 5 mm)..

The same electrical characterization method discussed in Chapter 2 was also performed on the NMOECT embedded with porous SPE. Cadilha et al.[102] reported that the transistor gated by SPE shows humidity dependent characteristics. In higher humidity environment, the moisture absorbed by the SPE builds pathway for the movement of ions, the ions in the polymer have higher mobility, resulting in better ion conductivity[102]. The SPE embedded device shows better performance in the higher humidity. The humidity dependent characteristics was also observed in the pour SPE embedded NMOECT.

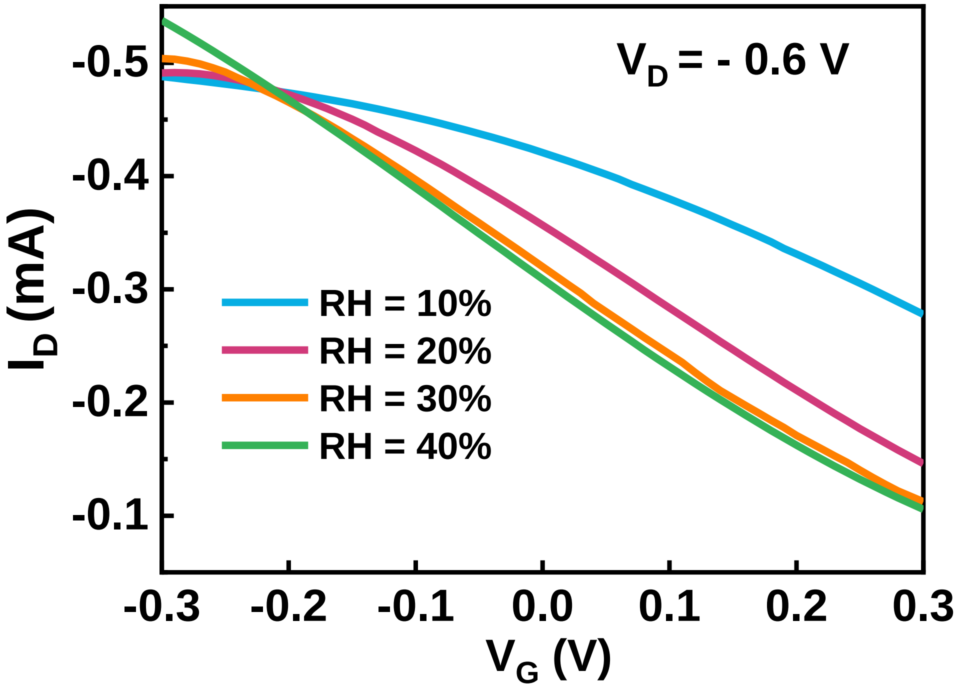

Figure 67. Transfer curve of a pour SPE embedded NMOECT

Figure 67 shows the transfer ($I_D - V_G$) curve of an pour SPE embedded NMOECT in various relative humidity (RH) environment. The OECT was placed in an isolated chamber with a humidity meter. The humidity of the chamber was controlled either by desiccant or water in a dishes, which can decrease the humidity or increase humidity respectively. The humidity level was monitored by the humidity meter. In a low humidity environment of 10%, the change of drain current (ΔI_D) is small. When the humidity increased, the ΔI_D becomes larger. The improvement of transfer curve saturated when the humidity is higher than 40%.

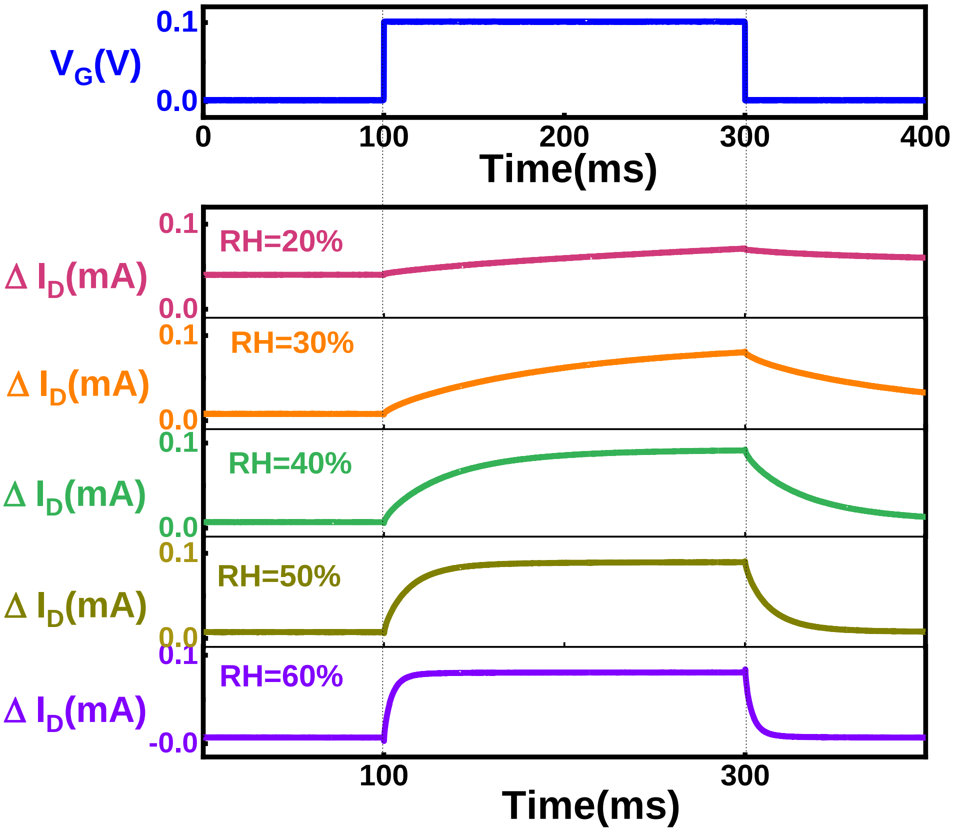

Figure 68. Response speed experiment results of the OECT in various RH environments.

The RH level also affects the response speed of the pour SPE embedded NMOECT. The response speed experiments were performed by applying a voltage pulse to the gate electrode and measuring the change of the channel current (ΔI_D). As shown in the Figure 68. In a higher RH environment, the response of the drain current becomes steep in the rising edge, as well as the falling edge. The time constant of the response current is utilized to reflect the speed of the OECT. Figure 69 shows the time constant extracted from the ΔI_D curves in Figure 68. The time constant decrease with increase of relative humidity, meaning the OECT becomes fast. The electrophysiological signals from human skin are in the range of less than 50 Hz[72], which means a response time of less than 10 ms is necessary to fully acquire the whole waveform of the signals. As shown in Figure 69, the OECT in the environment with a humidity higher than 60% has a response time less than 1 ms, which can ensure the full acquisition of electrophysiological signals.

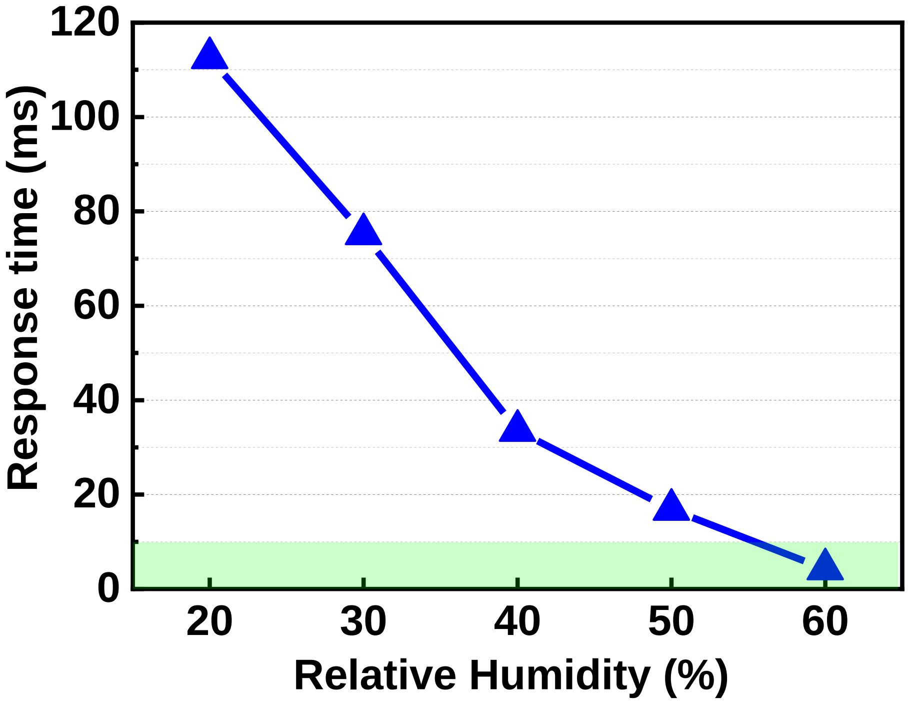

Figure 69. The response time constant of the OECT versus relative humidity.

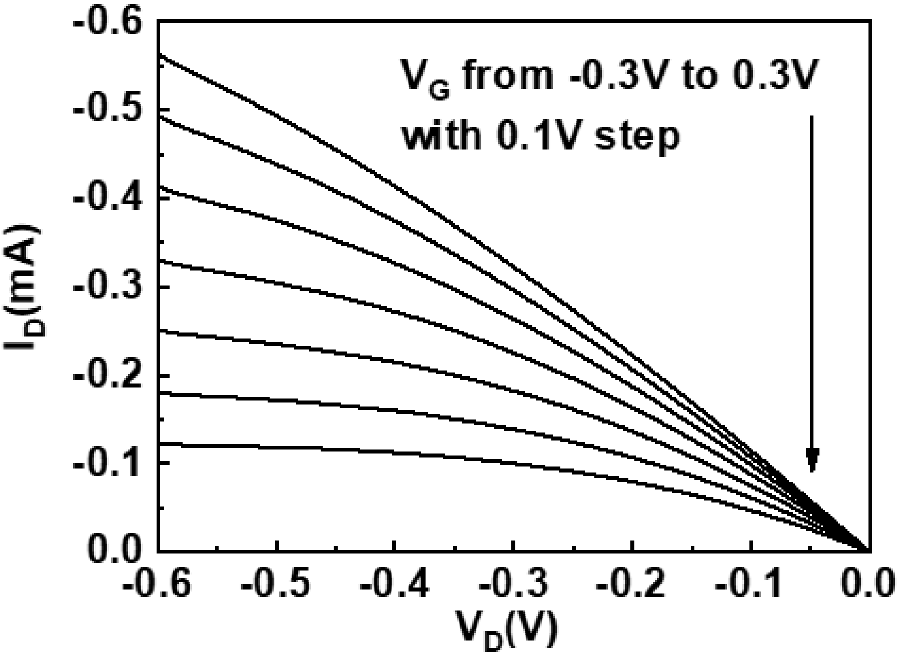

Figure 70. The output curve of the OECT in the 60% RH environment.

Figure 70 shows the output curve of the OECT in the 60% RH environment. It shows a good ohmic contact when the drain voltage V_D is small, while the drain current shows saturation phenomenon when the V_D is large.

As discussed above, a higher relative humidity is needed for the performance of the porous SPE embedded NMOECT. Interestingly, the surface of human skin is a high humidity environment. Several researches demonstrated that the relative humidity level of human skin surface is more than 60%[103, 104], which is suitable for the OECT to work in a response speed that can fully acquire the electrophysiological signals even the atmosphere humidity is low.

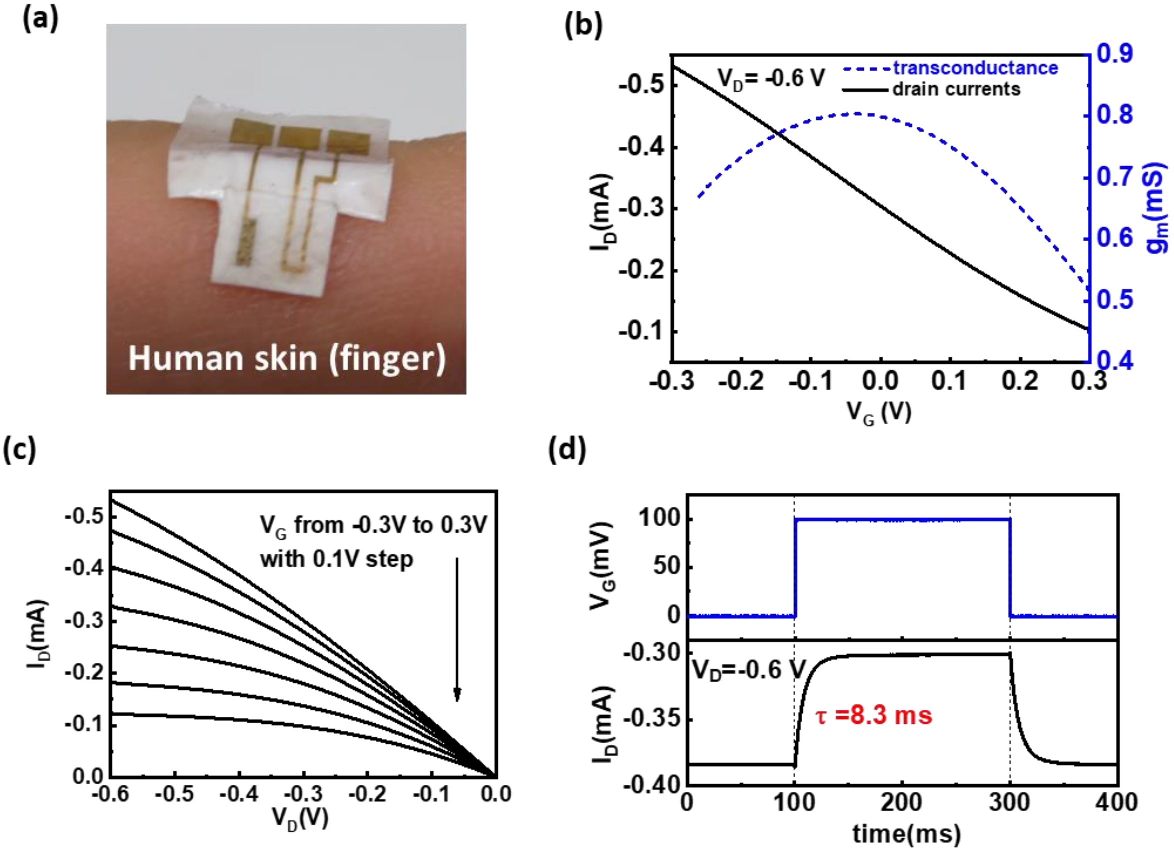

Figure 71. (a) A NMOECT embedded with porous SPE attached the skin of a finger. (b-d) The transfer curve (b), output curve (c), and response speed (d) of the OECT on the skin surface.

Figure 71 shows a OECT embedded with porous SPE that is attached to the skin surface and its electrical characteristics. The electrical characteristics were measured in a 30% RH atmosphere.

In the 30% RH environment, if the OECT is not loaded onto the skin surface, it shows poor performance as discussed above. However, after the OECT attached to the skin for more than 2 minutes, the electrical performance of the OECT improved a lot. As she data shown in Figure 71 (b) and (c), which is the characteristics after the OECT attached to skin. A good controllability of the gate voltage signal was achieved, with a maximum transconductance of 0.8 mS. Figure 71 (d) is the response speed experiments results of the OECT on skin, revealing that the response time is 8.3 ms while attaching the OECT on the skin surface. From the results, we can see that the relative humidity level around the skin surface can satisfy the OECT for electrophysiological signal acquiring.

4.4 Electrocardiographic signal acquired by NMOECT embedded with porous SPE

The ECG signal recording was performed to demonstrate the electrophysiological signal recording. Before attached the porous SPE embedded OECT to the skin, we first placed the it to the humidity controllable isolated chamber and load the ECG signals to the OECT using cables. A setup was built as shown in the Figure 72 (a).

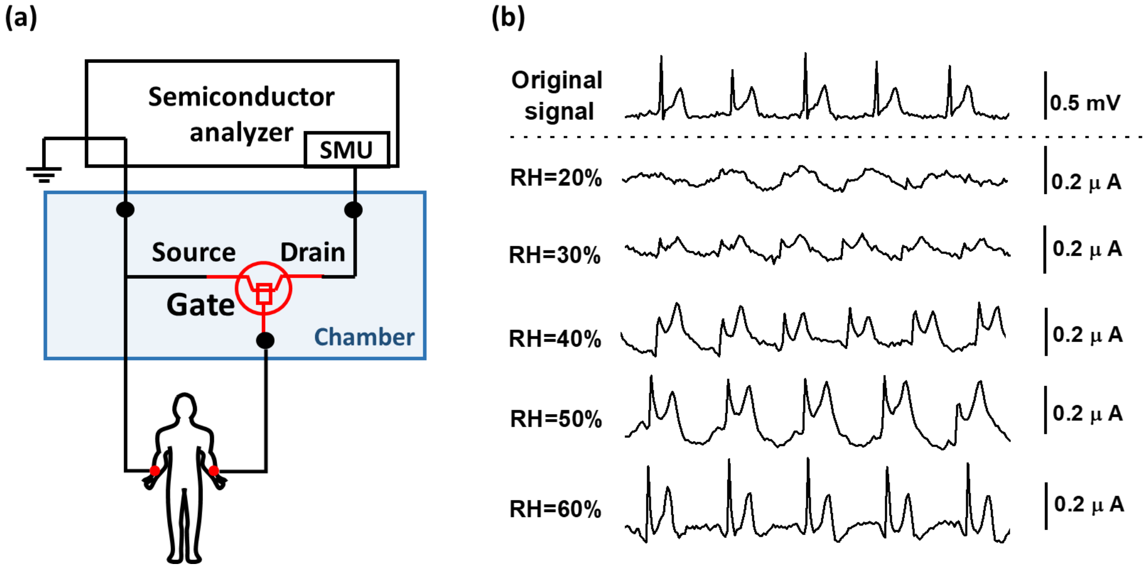

Figure 72. Recording of ECG signals with OECT. (a) Schematic of the setup. (b) The recorded signals while the OECT in various humidity.

The ECG signals were recorded in various chamber humidity from 20% to 60 %. Figure 72 (b) shows the recorded signals. In a low humidity of 20%, the ECG signals is rarely seen, because the low response speed of the OECT is slow. When with the RH level increased, the recorded signal is more clear and with higher signal amplitude. In the low humidity environment, the OECT cannot response to the high-frequency peaks, such as QRS peak. With the humidity increased, the response of OECT becomes faster, as discussed in last section, then the amplitude of the QRS peak becomes more obvious.

The actual electrode without the gate electrodes was fabricated and attached to the skin surface, using the skin as the gate electrode, as shown in the Figure 73 (a). The acquired ECG signals is shown in Figure 73 (b), which is in same amplitude level with the signal acquired in a 60% RH environment. From the results, we can see that the RH level on the skin surface can satisfy the requirement of OECT, and the ECG signals can be acquired.

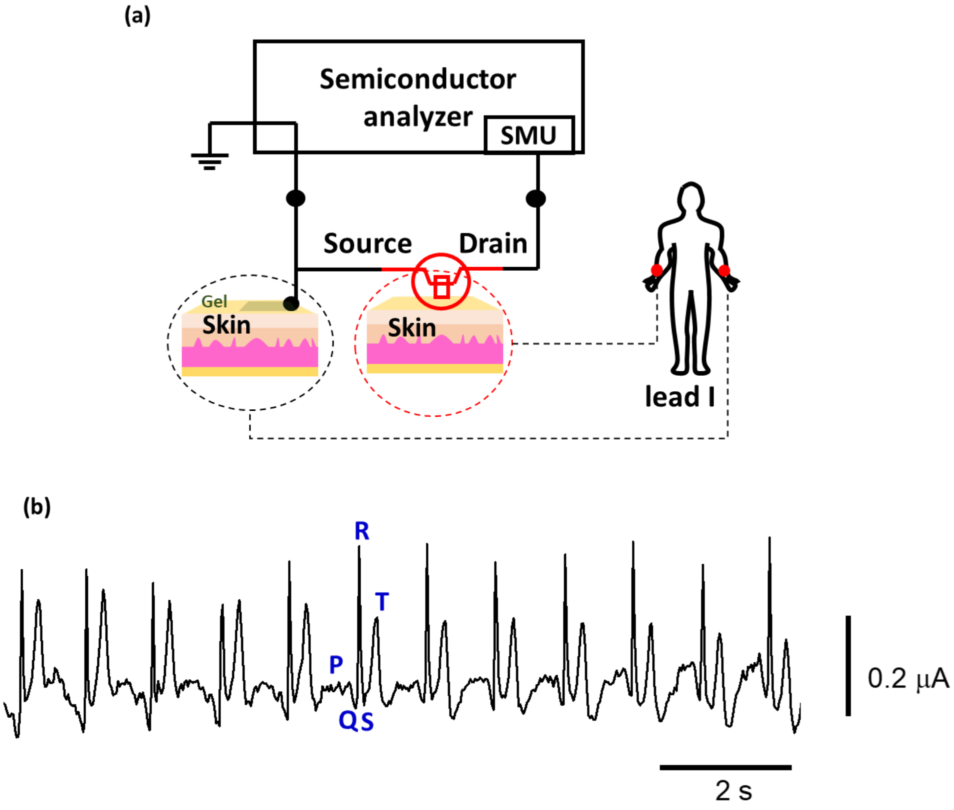

Figure 73. (a) The schematic of the setup for contacting the OECT on the skin surface as the active electrode. (b) The ECG signals acquired by the OECT.

Here, the feasibility of using the porous SPE embedded NMOECT as on-skin ECG electrode has been demonstrated. As an active element with low channel resistance, the signal amplified by the OECT contains extremely low output impedance, rendering the signals stable against the environmental noise. On the other hand, the signal amplified by the active electrode is easier for locally signal processing, such as using filter to extract the signal in target frequency range.

Chapter 5: Summary and prospect

5.1 Summary

The gas-permeability is critical for the device that directly contact with human skin. Even the on-skin electronics have been developed for years, the research focusing on developing the gas-permeable active on-skin components can rarely be seen, which limited the function and performance of the on-skin electronic system. In this study, for the first time, we successfully developed the porous solid-state polymer electrolyte embedded nanomesh organic electrochemical transistor that can be used as on-skin active electrodes for electrophysiological signal acquiring and local amplification. The gas-permeable on-skin OECT can eliminate the risk of accumulated moisture between the skin and the device, rendering the long-term wearing and health monitoring.

The ultrathin and flexible nanomesh was utilized as substrate for the device fabrication. We explored the process of fabricating the active transistor device onto the irregular and soft naomesh substrate. The electric performance of the NMOECT were systematically studied. For deeply understanding the performance of the NMOECT, a more accurate model was proposed for fitting the electrical characteristics of the NMOECT, which makes the prediction and design of circuit based on NMOECT easier.

The NMOECT used as on-skin electrodes for ECG signal acquiring and amplifying were demonstrated. The converting and filtering of the signal acquired by the NMOECT was proposed and discussed. The superior performance of the NMOECT enables the electrodes working in a low voltage and outputting a low impedance signals. The high-quality signals make the health monitoring more stable and safe. A simple prototype for wirelessly transmitting the signal of NMOECT electrode to mobile device were proposed. The feasibility of using NMOECT as active on-skin ECG electrodes was proved.

The solid-state polymer electrolyte with porous structure was proposed and to be embedded with NMOECT for the first time. The composition of the porous SPE was optimized to get sufficient porosity and ion conductivity that can support the function of OECT. Acquiring of the ECG signals using the gas-permeable OECT was also demonstrated.

This study firstly developed the nanomesh type gas-permeable transistor device. The transistor devices enlarged the function and freedom of the design of the on-skin electronic system, which advanced the research and development of the ultra-comfortable on-skin electronics.

5.2 Prospect

The OECT has been well recognized with high electric performance, easy fabrication process, and high biocompatibility. Researchers have utilized the superior characteristics of OECT to acquire high-quality signals for many different applications, such as electrophysiological sensors, chemical sensors, printing circuits, and so on. It is promising to use OECT for in-vivo signal monitoring. However, using OECT for on-skin application is facing challenges, including the softness of the device, the gas-permeability while wearing on the skin, the signal recording, and some issues related to the stability of the organic materials.

This study targets at the application of OECT for on-skin application, using the ultra-soft nanomesh as the substrate for fabrication, and embedded the porous SPE with it, successfully made the OECT in the porous structure, which is the first gas-permeable transistor-type device for on-skin application. On the other hand, the porous OECT device also expanded the type of device for nanomesh electronics, which has been proved as a feasible structure of on-skin electronics. The methodologies discussed in this study, including the device fabrication, the characterization, the signal reading, will give an adequate reference for future research and development of the complex on-skin electronics.

In this study, we mainly focus on the structure of the OECT and the application of on-skin electrophysiological electrodes, the mature materials are used for fabrication. In the future, the more advanced materials with better performance will enhance the performance of the NMOECT. On the other hand, the more complicated design of OECT based circuits can further improve the signal quality acquired by the OECT electrode. For example, incorporate with n-type channel materials of the OECT, to build complementary circuits with higher voltage gain.

Another possible issue that limit the further application of the organic materials based sensors is the stability of the material, which reduced the stability of the devices. The OECT also shows the degradation after continuously working. In the future, the development of stable and robust materials will facilitate the application of organic electronics. The other possibilities will also be expanded, such as chemical sensor, which requires a better stability.

Gas-permeable electrode is one of the components of the health monitoring system. The NMOECT can acquire high quality signals, however, the whole system also need other components, such as power supply, data storage, transmission, and processing, and so on. For ultimate comfortable on-skin patch that can harmonized with human, the investigating of other components and system-level design needs further study.

Reference

1. Liu, Y.; Pharr, M.; Salvatore, G. A., Lab-on-Skin: A Review of Flexible and Stretchable Electronics for Wearable Health Monitoring. *ACS Nano* **2017,** *11* (10), 9614-9635.

2. Someya, T.; Amagai, M., Toward a new generation of smart skins. *Nat. Biotechnol.* **2019,** *37* (4), 382-388.

3. Kim, J. J.; Wang, Y.; Wang, H.; Lee, S.; Yokota, T.; Someya, T., Skin Electronics: Next‐Generation Device Platform for Virtual and Augmented Reality. *Adv. Funct. Mater.* **2021**, 2009602.

4. Xu, K.; Lu, Y.; Takei, K., Multifunctional Skin-Inspired Flexible Sensor Systems for Wearable Electronics. *Advanced Materials Technologies* **2019,** *4* (3), 1800628.

5. Li, S.; Zhang, Y.; Wang, Y.; Xia, K.; Yin, Z.; Wang, H.; Zhang, M.; Liang, X.; Lu, H.; Zhu, M.; Wang, H.; Shen, X.; Zhang, Y., Physical sensors for skin‐inspired electronics. *InfoMat* **2019,** *2* (1), 184-211.

6. Wang, S.; Xu, J.; Wang, W.; Wang, G. N.; Rastak, R.; Molina-Lopez, F.; Chung, J. W.; Niu, S.; Feig, V. R.; Lopez, J.; Lei, T.; Kwon, S. K.; Kim, Y.; Foudeh, A. M.; Ehrlich, A.; Gasperini, A.; Yun, Y.; Murmann, B.; Tok, J. B.; Bao, Z., Skin electronics from scalable fabrication of an intrinsically stretchable transistor array. *Nat.* **2018,** *555* (7694), 83-88.

7. Cai, S.; Han, Z.; Wang, F.; Zheng, K.; Cao, Y.; Ma, Y.; Feng, X., Review on flexible photonics/electronics integrated devices and fabrication strategy. *Science China Information Sciences* **2018,** *61* (6), 1-27.

8. Zeng, W.; Shu, L.; Li, Q.; Chen, S.; Wang, F.; Tao, X. M., Fiber-based wearable electronics: a review of materials, fabrication, devices, and applications. *Adv. Mater.* **2014,** *26* (31), 5310-5336.

9. Kim, D. H.; Lu, N.; Ma, R.; Kim, Y. S.; Kim, R. H.; Wang, S.; Wu, J.; Won, S. M.; Tao, H.; Islam, A.; Yu, K. J.; Kim, T. I.; Chowdhury, R.; Ying, M.; Xu, L.; Li, M.; Chung, H. J.; Keum, H.; McCormick, M.; Liu, P.; Zhang, Y. W.; Omenetto, F. G.; Huang, Y.; Coleman, T.; Rogers, J. A., Epidermal electronics. *Science* **2011,** *333* (6044), 838-843.

10. Wu, H.; Yang, G.; Zhu, K.; Liu, S.; Guo, W.; Jiang, Z.; Li, Z., Materials, Devices, and Systems of On-Skin Electrodes for Electrophysiological Monitoring and Human-Machine Interfaces. *Adv. Sci.* **2021,** *8* (2), 2001938.

11. Park, S. H.; Lee, H. B.; Yeon, S. M.; Park, J.; Lee, N. K., Flexible and Stretchable Piezoelectric Sensor with Thickness-Tunable Configuration of Electrospun Nanofiber Mat and Elastomeric Substrates. *ACS Appl. Mater. Interfaces* **2016,** *8* (37), 24773-24781.

12. Dhakar, L.; Pitchappa, P.; Tay, F. E. H.; Lee, C., An intelligent skin based self-powered finger motion sensor integrated with triboelectric nanogenerator. *Nano Energy* **2016,** *19*, 532-540.

13. Amjadi, M.; Yoon, Y. J.; Park, I., Ultra-stretchable and skin-mountable strain sensors using carbon nanotubes-Ecoflex nanocomposites. *Nanotechnology* **2015,** *26* (37), 375501.

14. Nakata, S.; Arie, T.; Akita, S.; Takei, K., Wearable, Flexible, and Multifunctional Healthcare Device with an ISFET Chemical Sensor for Simultaneous Sweat pH and Skin Temperature Monitoring. *ACS Sens* **2017,** *2* (3), 443-448.

15. Lorwongtragool, P.; Sowade, E.; Watthanawisuth, N.; Baumann, R. R.; Kerdcharoen, T., A novel wearable electronic nose for healthcare based on flexible printed chemical sensor array. *Sensors* **2014,** *14* (10), 19700-19712.

16. Khodagholy, D.; Doublet, T.; Quilichini, P.; Gurfinkel, M.; Leleux, P.; Ghestem, A.; Ismailova, E.; Herve, T.; Sanaur, S.; Bernard, C.; Malliaras, G. G., In vivo recordings of brain activity using organic transistors. *Nat. Commun.* **2013,** *4*, 1575.

17. Nagamine, K.; Chihara, S.; Kai, H.; Kaji, H.; Nishizawa, M., Totally shape-conformable electrode/hydrogel composite for on-skin electrophysiological measurements. *Sensors and Actuators B: Chemical* **2016,** *237*, 49-53.

18. Pani, D.; Achilli, A.; Bonfiglio, A., Survey on Textile Electrode Technologies for Electrocardiographic (ECG) Monitoring, from Metal Wires to Polymers. *Advanced Materials Technologies* **2018,** *3* (10), 1800008.

19. Takeshita, T.; Yoshida, M.; Takei, Y.; Ouchi, A.; Hinoki, A.; Uchida, H.; Kobayashi, T., Relationship between Contact Pressure and Motion Artifacts in ECG Measurement with Electrostatic Flocked Electrodes Fabricated on Textile. *Sci Rep* **2019,** *9* (1), 5897.

20. Miyamoto, A.; Lee, S.; Cooray, N. F.; Lee, S.; Mori, M.; Matsuhisa, N.; Jin, H.; Yoda, L.; Yokota, T.; Itoh, A.; Sekino, M.; Kawasaki, H.; Ebihara, T.; Amagai, M.; Someya, T., Inflammation-free, gas-permeable, lightweight, stretchable on-skin electronics with nanomeshes. *Nat. Nanotechnol.* **2017,** *12* (9), 907-913.

21. Xu, B.; Akhtar, A.; Liu, Y.; Chen, H.; Yeo, W. H.; Park, S. I.; Boyce, B.; Kim, H.; Yu, J.; Lai, H. Y.; Jung, S.; Zhou, Y.; Kim, J.; Cho, S.; Huang, Y.; Bretl, T.; Rogers, J. A., An Epidermal Stimulation and Sensing Platform for Sensorimotor Prosthetic Control, Management of Lower Back Exertion, and Electrical Muscle Activation. *Adv. Mater.* **2016,** *28* (22), 4462-4471.

22. Kabiri Ameri, S.; Ho, R.; Jang, H.; Tao, L.; Wang, Y.; Wang, L.; Schnyer, D. M.; Akinwande, D.; Lu, N., Graphene Electronic Tattoo Sensors. *ACS Nano* **2017,** *11* (8), 7634-7641.

23. Jeong, J. W.; Yeo, W. H.; Akhtar, A.; Norton, J. J.; Kwack, Y. J.; Li, S.; Jung, S. Y.; Su, Y.; Lee, W.; Xia, J.; Cheng, H.; Huang, Y.; Choi, W. S.; Bretl, T.; Rogers, J. A., Materials and optimized designs for human-machine interfaces via epidermal electronics. *Adv. Mater.* **2013,** *25* (47), 6839-6846.

24. Lee, S.; Sasaki, D.; Kim, D.; Mori, M.; Yokota, T.; Lee, H.; Park, S.; Fukuda, K.; Sekino, M.; Matsuura, K.; Shimizu, T.; Someya, T., Ultrasoft electronics to monitor dynamically pulsing cardiomyocytes. *Nat. Nanotechnol.* **2019,** *14* (2), 156-160.

25. Nayeem, M. O. G.; Lee, S.; Jin, H.; Matsuhisa, N.; Jinno, H.; Miyamoto, A.; Yokota, T.; Someya, T., All-nanofiber-based, ultrasensitive, gas-permeable mechanoacoustic sensors for continuous long-term heart monitoring. *Proc. Natl. Acad. Sci. U. S. A.* **2020,** *117* (13), 7063-7070.

26. Gray, M.; Weir, D., Prevention and treatment of moisture-associated skin damage (maceration) in the periwound skin. *Journal of Wound Ostomy & Continence Nursing* **2007,** *34*, 153-157.

27. Sun, B.; McCay, R. N.; Goswami, S.; Xu, Y.; Zhang, C.; Ling, Y.; Lin, J.; Yan, Z., Gas-Permeable, Multifunctional On-Skin Electronics Based on Laser-Induced Porous Graphene and Sugar-Templated Elastomer Sponges. *Adv. Mater.* **2018,** *30* (50), e1804327.

28. Lee, S.; Franklin, S.; Faezeh Arab Hassani; Yokota, T.; Md Osman Goni Nayeem; Wang, Y.; Leib, R.; Cheng, G.; Franklin, D. W.; Someya, T., Nanomesh pressure sensor for monitoring finger manipulation without sensory interference. *Science* **2020,** *370* (6519), 966-970.

29. Maji, S.; Burke, M. J., Establishing the Input Impedance Requirements of ECG Recording Amplifiers. *IEEE Transactions on Instrumentation and Measurement* **2020,** *69* (3), 825-835.

30. Campana, A.; Cramer, T.; Simon, D. T.; Berggren, M.; Biscarini, F., Electrocardiographic recording with conformable organic electrochemical transistor fabricated on resorbable bioscaffold. *Adv. Mater.* **2014,** *26* (23), 3874-3878.

31. Lee, W.; Someya, T., Emerging Trends in Flexible Active Multielectrode Arrays. *Chem. Mater.* **2019,** *31* (17), 6347-6358.

32. Koo, J. H.; Jeong, S.; Shim, H. J.; Son, D.; Kim, J.; Kim, D. C.; Choi, S.; Hong, J. I.; Kim, D. H., Wearable Electrocardiogram Monitor Using Carbon Nanotube Electronics and Color-Tunable Organic Light-Emitting Diodes. *ACS Nano* **2017,** *11* (10), 10032-10041.

33. Sugiyama, M.; Uemura, T.; Kondo, M.; Akiyama, M.; Namba, N.; Yoshimoto, S.; Noda, Y.; Araki, T.; Sekitani, T., An ultraflexible organic differential amplifier for recording electrocardiograms. *Nat. Electron.* **2019,** *2* (8), 351-360.

34. Park, S.; Heo, S. W.; Lee, W.; Inoue, D.; Jiang, Z.; Yu, K.; Jinno, H.; Hashizume, D.; Sekino, M.; Yokota, T.; Fukuda, K.; Tajima, K.; Someya, T., Self-powered ultra-flexible electronics via nano-grating-patterned organic photovoltaics. *Nat.* **2018,** *561* (7724), 516-521.

35. Grubb, P. M.; Mokhtari Koushyar, F.; Lenz, T.; Asghari, A.; Gan, G.; Xia, W.; Dalir, H.; Subbaraman, H.; Chen, R. T., High Speed Roll-to-Roll Printable Transistor Enabled by a Pulsed Light Curable CNT Ink. *Journal of Manufacturing and Materials Processing* **2019,** *3* (2), 33.

36. Zhang, H.; Xiang, L.; Yang, Y.; Xiao, M.; Han, J.; Ding, L.; Zhang, Z.; Hu, Y.; Peng, L. M., High-Performance Carbon Nanotube Complementary Electronics and Integrated Sensor Systems on Ultrathin Plastic Foil. *ACS Nano* **2018,** *12* (3), 2773-2779.

37. Mohammad Ali Zanjani, S.; Dousti, M.; Dolatshahi, M., High-precision, resistor less gas pressure sensor and instrumentation amplifier in CNT technology. *AEU - International Journal of Electronics and Communications* **2018,** *93*, 325-336.

38. Chen, C. M.; Anastasova, S.; Zhang, K.; Rosa, B. G.; Lo, B. P. L.; Assender, H. E.; Yang, G. Z., Towards Wearable and Flexible Sensors and Circuits Integration for Stress Monitoring. *IEEE J Biomed Health Inform* **2020,** *24* (8), 2208-2215.

39. Sekine, T.; Gaïtis, A.; Sato, J.; Miyazawa, K.; Muraki, K.; Shiwaku, R.; Takeda, Y.; Matsui, H.; Kumaki, D.; Domingues Dos Santos, F.; Miyabo, A.; Charbonneau, M.; Tokito, S., Low Operating Voltage and Highly Pressure-Sensitive Printed Sensor for Healthcare Monitoring with Analogic Amplifier Circuit. *ACS Appl. Electron. Mater.* **2019,** *1* (2), 246-252.

40. Braendlein, M.; Lonjaret, T.; Leleux, P.; Badier, J. M.; Malliaras, G. G., Voltage Amplifier Based on Organic Electrochemical Transistor. *Adv. Sci.* **2017,** *4* (1), 1600247.

41. Leleux, P.; Rivnay, J.; Lonjaret, T.; Badier, J. M.; Benar, C.; Herve, T.; Chauvel, P.; Malliaras, G. G., Organic electrochemical transistors for clinical applications. *Adv. Healthc. Mater.* **2015,** *4* (1), 142-147.

42. Jo, Y. J.; Kim, H.; Ok, J.; Shin, Y. J.; Shin, J. H.; Kim, T. H.; Jung, Y.; Kim, T. i., Biocompatible and Biodegradable Organic Transistors Using a Solid‐State Electrolyte Incorporated with Choline‐Based Ionic Liquid and Polysaccharide. *Adv. Funct. Mater.* **2020,** *30* (29), 1909707.

43. Khodagholy, D.; Rivnay, J.; Sessolo, M.; Gurfinkel, M.; Leleux, P.; Jimison, L. H.; Stavrinidou, E.; Herve, T.; Sanaur, S.; Owens, R. M.; Malliaras, G. G., High transconductance organic electrochemical transistors. *Nat. Commun.* **2013,** *4*, 1-6.

44. Steudel, S.; De Vusser, S.; De Jonge, S.; Janssen, D.; Verlaak, S.; Genoe, J.; Heremans, P., Influence of the dielectric roughness on the performance of pentacene transistors. *Appl. Phys. Lett.* **2004,** *85* (19), 4400-4402.

45. Virkar, A. A.; Mannsfeld, S.; Bao, Z.; Stingelin, N., Organic semiconductor growth and morphology considerations for organic thin-film transistors. *Adv. Mater.* **2010,** *22* (34), 3857-3875.

46. Friedlein, J. T.; Donahue, M. J.; Shaheen, S. E.; Malliaras, G. G.; McLeod, R. R., Microsecond Response in Organic Electrochemical Transistors: Exceeding the Ionic Speed Limit. *Adv. Mater.* **2016,** *28* (38), 8398-8404.

47. Lee, W.; Kim, D.; Matsuhisa, N.; Nagase, M.; Sekino, M.; Malliaras, G. G.; Yokota, T.; Someya, T., Transparent, conformable, active multielectrode array using organic electrochemical transistors. *Proc. Natl. Acad. Sci. U.S.A.* **2017,** *114* (40), 10554-10559.

48. Venkatraman, V.; Friedlein, J. T.; Giovannitti, A.; Maria, I. P.; McCulloch, I.; McLeod, R. R.; Rivnay, J., Subthreshold Operation of Organic Electrochemical Transistors for Biosignal Amplification. *Adv Sci (Weinh)* **2018,** *5* (8), 1800453.

49. Currano, L. J.; Sage, F. C.; Hagedon, M.; Hamilton, L.; Patrone, J.; Gerasopoulos, K., Wearable Sensor System for Detection of Lactate in Sweat. *Sci Rep* **2018,** *8* (1), 1-11.

50. Tang, H.; Lin, P.; Chan, H. L.; Yan, F., Highly sensitive dopamine biosensors based on organic electrochemical transistors. *Biosens. Bioelectron.* **2011,** *26* (11), 4559-4563.

51. Mariani, F.; Gualandi, I.; Tessarolo, M.; Fraboni, B.; Scavetta, E., PEDOT: Dye-Based, Flexible Organic Electrochemical Transistor for Highly Sensitive pH Monitoring. *ACS Appl. Mater. Interfaces* **2018,** *10* (26), 22474-22484.

52. Bihar, E.; Deng, Y.; Miyake, T.; Saadaoui, M.; Malliaras, G. G.; Rolandi, M., A Disposable paper breathalyzer with an alcohol sensing organic electrochemical transistor. *Sci Rep* **2016,** *6*, 27582.

53. Gualandi, I.; Marzocchi, M.; Scavetta, E.; Calienni, M.; Bonfiglio, A.; Fraboni, B., A simple all-PEDOT:PSS electrochemical transistor for ascorbic acid sensing. *J Mater Chem B* **2015,** *3* (33), 6753-6762.

54. Gualandi, I.; Tonelli, D.; Mariani, F.; Scavetta, E.; Marzocchi, M.; Fraboni, B., Selective detection of dopamine with an all PEDOT:PSS Organic Electrochemical Transistor. *Sci. Rep.* **2016,** *6*, 35419.

55. Rivnay, J.; Inal, S.; Salleo, A.; Owens, R. M.; Berggren, M.; Malliaras, G. G., Organic electrochemical transistors. *Nat. Rev. Mater.* **2018,** *3* (2), 1-14.

56. Stritesky, S.; Markova, A.; Vitecek, J.; Safarikova, E.; Hrabal, M.; Kubac, L.; Kubala, L.; Weiter, M.; Vala, M., Printing inks of electroactive polymer PEDOT:PSS: The study of biocompatibility, stability, and electrical properties. *J. Biomed. Mater. Res. A* **2018,** *106* (4), 1121-1128.

57. Liu, J.; Wang, X.; Li, D.; Coates, N. E.; Segalman, R. A.; Cahill, D. G., Thermal Conductivity and Elastic Constants of PEDOT:PSS with High Electrical Conductivity. *Macromolecules* **2015,** *48* (3), 585-591.

58. Lee, H.; Lee, S.; Lee, W.; Yokota, T.; Fukuda, K.; Someya, T., Ultrathin Organic Electrochemical Transistor with Nonvolatile and Thin Gel Electrolyte for Long ‐ Term Electrophysiological Monitoring. *Adv. Funct. Mater.* **2019,** *29* (48), 1906982.

59. Kondo, M.; Uemura, T.; Matsumoto, T.; Araki, T.; Yoshimoto, S.; Sekitani, T., Ultraflexible and ultrathin polymeric gate insulator for 2 V organic transistor circuits. *Applied Physics Express* **2016,** *9* (6), 061602.

60. Zabihi, F.; Xie, Y.; Gao, S.; Eslamian, M., Morphology, conductivity, and wetting characteristics of PEDOT:PSS thin films deposited by spin and spray coating. *Appl. Surf. Sci.* **2015,** *338*, 163-177.

61. Zhang, M.; Lin, P.; Yang, M.; Yan, F., Fabrication of organic electrochemical transistor arrays for biosensing. *Biochim Biophys Acta Mol Basis Dis* **2013,** *1830* (9), 4402-4406.

62. Tarabella, G.; Santato, C.; Yang, S. Y.; Iannotta, S.; Malliaras, G. G.; Cicoira, F., Effect of the gate electrode on the response of organic electrochemical transistors. *Appl. Phys. Lett.* **2010,** *97* (12), 123304.

63. Bernards, D. A.; Malliaras, G. G., Steady-State and Transient Behavior of Organic Electrochemical Transistors. *Adv. Funct. Mater.* **2007,** *17* (17), 3538-3544.

64. Lingstedt, L. V.; Ghittorelli, M.; Lu, H.; Koutsouras, D. A.; Marszalek, T.; Torricelli, F.; Crăciun, N. I.; Gkoupidenis, P.; Blom, P. W. M., Effect of DMSO Solvent Treatments on the Performance of PEDOT:PSS Based Organic Electrochemical Transistors. *Adv. Electron. Mater.* **2019,** *5* (3), 1800804.

65. Heikenfeld, J.; Jajack, A.; Rogers, J.; Gutruf, P.; Tian, L.; Pan, T.; Li, R.; Khine, M.; Kim, J.; Wang, J.; Kim, J., Wearable sensors: modalities, challenges, and prospects. *Lab Chip* **2018,** *18* (2), 217-248.

66. Nissa, J.; Janson, P.; Simon, D. T.; Berggren, M., Expanding the understanding of organic electrochemical transistor function. *Appl. Phys. Lett.* **2021,** *118* (5), 053301.

67. Friedlein, J. T.; McLeod, R. R.; Rivnay, J., Device physics of organic electrochemical transistors. *Org. Electron.* **2018,** *63*, 398-414.

68. Faria, G. C.; Duong, D. T.; Salleo, A., On the transient response of organic electrochemical transistors. *Org. Electron.* **2017,** *45*, 215-221.

69. Cai, L.; Zhang, S.; Miao, J.; Yu, Z.; Wang, C., Fully Printed Foldable Integrated Logic Gates with Tunable Performance Using Semiconducting Carbon Nanotubes. *Adv. Funct. Mater.* **2015,** *25* (35), 5698-5705.

70. Na, H.; Cho, H.; Sim, K.; Shim, H.; Kim, S.-J.; Pyo, S., Electrical responses of short-channel organic transistor prepared by solution-processed organic crystal wire mask. *Org. Electron.* **2014,** *15* (11), 2728-2733.

71. Celin, S.; Vasanth, K., ECG Signal Classification Using Various Machine Learning Techniques. *J. Med. Syst.* **2018,** *42* (12), 241.

72. Abedin, Z.; Carbajal, E. V., Frequency analysis of the PQRST complex of the normal electrocardiogram. *J. Clin. Eng.* **1983,** *8*, 297-300.

73. Chi, Y. M.; Jung, T. P.; Cauwenberghs, G., Dry-contact and noncontact biopotential electrodes: methodological review. *IEEE Rev Biomed Eng* **2010,** *3*, 106-119.

74. Wang, C.; Wang, T.; Wang, L.; Hu, Z.; Cui, Z.; Li, J.; Dong, S.; Zhou, X.; Cui, G., Differentiated Lithium Salt Design for Multilayered PEO Electrolyte Enables a High-Voltage Solid-State Lithium Metal Battery. *Adv Sci (Weinh)* **2019,** *6* (22), 1901036.

75. Lin, Y.; Li, J.; Liu, K.; Liu, Y.; Liu, J.; Wang, X., Unique starch polymer electrolyte for high capacity all-solid-state lithium sulfur battery. *Green Chem.* **2016,** *18* (13), 3796-3803.

76. Sonker, R. K.; Rahul; Sabhajeet, S. R., ZnO nanoneedle structure based dye-sensitized solar cell utilizing solid polymer electrolyte. *Mater. Lett.* **2018,** *223*, 133-136.

77. Rahul; Singh, S.; Singh, P. K.; Kakroo, S.; Hachim, D. M.; Dhapola, P. S.; Khan, Z. H., Eco-friendly dye sensitized solar cell using natural dye with solid polymer electrolyte as hole transport material. *Mater. Today* **2021,** *34*, 760-766.

78. Deka, B. K.; Hazarika, A.; Kwon, O.; Kim, D.; Park, Y.-B.; Park, H. W., Multifunctional enhancement of woven carbon fiber/ZnO nanotube-based structural supercapacitor and polyester resin-domain solid-polymer electrolytes. *Chem. Eng. J.* **2017,** *325,* 672-680.

79. Farah, N.; Ng, H. M.; Numan, A.; Liew, C.-W.; Latip, N. A. A.; Ramesh, K.; Ramesh, S., Solid polymer electrolytes based on poly(vinyl alcohol) incorporated with sodium salt and ionic liquid for electrical double layer capacitor. *Mater. Sci. Eng. B* **2019,** *251*.

80. Ngai, K. S.; Ramesh, S.; Ramesh, K.; Juan, J. C., A review of polymer electrolytes: fundamental, approaches and applications. *Ionics* **2016,** *22* (8), 1259-1279.

81. Fan, L.; Wei, S.; Li, S.; Li, Q.; Lu, Y., Recent Progress of the Solid-State Electrolytes for High-Energy Metal-Based Batteries. *Adv. Energy Mater.* **2018,** *8* (11), 1702657.

82. Afonso, M.; Morgado, J.; Alcácer, L., Inkjet printed organic electrochemical transistors with highly conducting polymer electrolytes. *J. Appl. Phys.* **2016,** *120* (16), 165502.

83. Sheliakina, M.; Mostert, A. B.; Meredith, P., An all-solid-state biocompatible ion-to-electron transducer for bioelectronics. *Materials Horizons* **2018,** *5* (2), 256-263.

84. Ko, J.; Wu, X.; Surendran, A.; Muhammad, B. T.; Leong, W. L., Self-Healable Organic Electrochemical Transistor with High Transconductance, Fast Response, and Long-Term Stability. *ACS Appl. Mater. Interfaces* **2020,** *12* (30), 33979-33988.

85. Chen, S.; Surendran, A.; Wu, X.; Leong, W. L., Contact Modulated Ionic Transfer Doping in All‐Solid‐State Organic Electrochemical Transistor for Ultra‐High Sensitive Tactile Perception at Low Operating Voltage. *Adv. Funct. Mater.* **2020,** *30* (51), 2006186.

86. Battista, E.; Lettera, V.; Villani, M.; Calestani, D.; Gentile, F.; Netti, P. A.; Iannotta, S.; Zappettini, A.; Coppedè, N., Enzymatic sensing with laccase-functionalized textile organic biosensors. *Org. Electron.* **2017,** *40*, 51-57.

87. Wang, Y.; Zhou, Z.; Qing, X.; Zhong, W.; Liu, Q.; Wang, W.; Li, M.; Liu, K.; Wang, D., Ion sensors based on novel fiber organic electrochemical transistors for lead ion detection. *Anal. Bioanal. Chem.* **2016,** *408* (21), 5779-5787.

88. Khodagholy, D.; Curto, V. F.; Fraser, K. J.; Gurfinkel, M.; Byrne, R.; Diamond, D.; Malliaras, G. G.; Benito-Lopez, F.; Owens, R. M., Organic electrochemical transistor incorporating an ionogel as a solid state electrolyte for lactate sensing. *J. Mater. Chem.* **2012,** *22* (10), 4440-4443.

89. Bernards, D. A.; Macaya, D. J.; Nikolou, M.; DeFranco, J. A.; Takamatsu, S.; Malliaras, G. G., Enzymatic sensing with organic electrochemical transistors. *J. Mater. Chem.* **2008,** *18* (1), 116-120.

90. Fan, L.; Wang, M.; Zhang, Z.; Qin, G.; Hu, X.; Chen, Q., Preparation and Characterization of PVA Alkaline Solid Polymer Electrolyte with Addition of Bamboo Charcoal. *Materials* **2018,** *11* (5), 679.

91. Mohamad, A. A.; Arof, A. K., Effect of storage time on the properties of PVA–KOH alkaline solid polymer electrolyte system. *Ionics* **2006,** *12* (1), 57-61.

92. Santos, F.; Tafur, J. P.; Abad, J.; Fernández Romero, A. J., Structural modifications and ionic transport of PVA-KOH hydrogels applied in Zn/Air batteries. *J. Electroanal. Chem.* **2019,** *850*, 113380.

93. Fan, X.; Liu, J.; Ding, J.; Deng, Y.; Han, X.; Hu, W.; Zhong, C., Investigation of the Environmental Stability of Poly(vinyl alcohol)-KOH Polymer Electrolytes for Flexible Zinc-Air Batteries. *Front Chem* **2019,** *7*, 678.

94. Aziz, S. B.; Abdullah, O. G.; Rasheed, M. A., Structural and electrical characteristics of PVA:NaTf based solid polymer electrolytes: role of lattice energy of salts on electrical DC conductivity. *J. Mater. Sci.: Mater. Electron.* **2017,** *28* (17), 12873-12884.

95. Long, L.; Wang, S.; Xiao, M.; Meng, Y., Polymer electrolytes for lithium polymer batteries. *Journal of Materials Chemistry A* **2016,** *4* (26), 10038-10069.

96. Aziz, S. B.; Abdullah, O. G.; Rasheed, M. A.; Ahmed, H. M., Effect of High Salt Concentration (HSC) on Structural, Morphological, and Electrical Characteristics of Chitosan Based Solid Polymer Electrolytes. *Polymers* **2017,** *9* (6), 187.

97. B. Aziz, S., The Study of Dielectric Properties and Conductivity Relaxation of Ion Conducting Chitosan:NaTf Based Solid Electrolyte. *Int. J. Electrochem. Sci.* **2018,** *13*, 10274-10288.

98. Rivero, S.; Damonte, L.; García, M. A.; Pinotti, A., An Insight into the Role of Glycerol in Chitosan Films. *Food Biosci.* **2016,** *11* (2), 117-127.

99. Chun, H. J.; Kim, G.-W.; Kim, C.-H., Fabrication of porous chitosan scaffold in order to improve biocompatibility. *J. Phys. Chem. Solids* **2008,** *69* (5-6), 1573-1576.

100. Yang, B.; Li, X.; Shi, S.; Kong, X.; Guo, G.; Huang, M.; Luo, F.; Wei, Y.; Zhao, X.; Qian, Z., Preparation and characterization of a novel chitosan scaffold. *Carbohydr. Polym.* **2010,** *80* (3), 860-865.

101. Ruprai, H.; Romanazzo, S.; Ireland, J.; Kilian, K.; Mawad, D.; George, L.; Wuhrer, R.; Houang, J.; Ta, D.; Myers, S.; Lauto, A., Porous Chitosan Films Support Stem Cells and Facilitate Sutureless Tissue Repair. *ACS Appl. Mater. Interfaces* **2019,** *11* (36), 32613-32622.

102. Cadilha Marques, G.; Weller, D.; Erozan, A. T.; Feng, X.; Tahoori, M.; Aghassi-Hagmann, J., Influence of Humidity on the Performance of Composite Polymer Electrolyte-Gated Field-Effect Transistors and Circuits. *IEEE Trans. Electron Devices* **2019,** *66* (5), 2202-2207.

103. Wu, J.; Sun, Y. M.; Wu, Z.; Li, X.; Wang, N.; Tao, K.; Wang, G. P., Carbon Nanocoil-Based Fast-Response and Flexible Humidity Sensor for Multifunctional Applications. *ACS Appl. Mater. Interfaces* **2019,** *11* (4), 4242-4251.

104. Dai, J.; Zhao, H.; Lin, X.; Liu, S.; Liu, Y.; Liu, X.; Fei, T.; Zhang, T., Ultrafast Response Polyelectrolyte Humidity Sensor for Respiration Monitoring. *ACS Appl. Mater. Interfaces* **2019,** *11* (6), 6483-6490.

Publications

Papers related to this thesis:

[1] **Jiabin Wang**, Sunghoon Lee, Tomoyuki Yokota, Yasutoshi Jimbo, Yan Wang, Md Osman Goni Nayeem, Masaya Nishinaka, Takao Someya. "Nanomesh Organic Electrochemical Transistor for Comfortable On-Skin Electrodes with Local Amplifying Function." ACS Applied Electronic Materials 2.11 (2020): 3601-3609.

[2] **Jiabin Wang**, Sunghoon Lee, Tomoyuki Yokota, Takao Someya. " Jiabin Wang, Sunghoon Lee, Tomoyuki Yokota, Yasutoshi Jimbo, Chihiro Okutani, Jae Joon Kim, Takao Someya. " Gas-permeable solid-state polymer electrolyte imbedded nanomesh organic electrochemical transistor as on-skin active electrode for electrophysiological signal acquiring.", Advanced Materials, under review.

Meetings related to this thesis:

[1] **Jiabin Wang**. “Nanomesh Organic Electrochemical Transistor(NMOECT) as active On-Skin Electrodes.” Young researchers society for flexible and stretchable electronics, online meeting, December, 2020.

Other publications

[1] Masaya Nishinaka, Hiroaki Jinno, Yasutoshi Jimbo, Sunghoon Lee, **Jiabin Wang**, Wonryung Lee, Tomoyuki Yokota, Takao Someya, "High-Transconductance Organic Electrochemical Transistor Fabricated on Ultra-Thin Films Using Spray Coating." Small Structures 2.3 (2020): 2000088.

[2] Yan Wang, Sunghoon Lee, Tomoyuki Yokota, Haoyang Wang, Zhi Jiang, **Jiabin Wang**, Mari Koizumi, Takao Someya, "A durable nanomesh on-skin strain gauge for natural skin motion monitoring with minimum mechanical constraints." Science advances 6.33 (2020): eabb7043.

[3] Yancong Qiao , Xiaoshi Li , **Jiabin Wang** , Shourui Ji , Thomas Hirtz , He Tian , Jinming Jian , Tianrui Cui , Ying Dong , Xinwei Xu , Fei Wang , Hong Wang , Yi Yang , Takao

Someya, and Tian-Ling Ren, “Sensation-Free and Sentient Graphene Electronic Skin”, Science advances, under review.

[4] Dongkai Cheng, **Jiabin Wang**, Tomoyuki Yokota, and Takao Someya, “Spatiotemporal processing in Photoplethysmography for skin microcirculation holographic visualization”, in preparation.

Acknowledgment

First and foremost, I would like to express my great appreciation and respect to my supervisor, Professor Takao Someya for continuous support, insightful guide, and invaluable help. He lets me know how a world-class scientist should be. My whole doctoral course is sponsored by The University of Tokyo Fellowship Special Scholarship Program for International Students. The international environment both in the UTokyo and my lab provides me a very enjoyable life period.

Dr. Tomoyuki Yokota and Dr. Sunghoon Lee provide give me the most meticulous help in my everywhere of my research journey. Their diligence and profound knowledge help me to deeply think about my research project and figure out the most exciting and frontier problems. Every time after the discussion with them, my brain feels recharged.

My research work cannot be finished without support from my lab members: Ms. Mari Koizumi, Mr. Ikue Kawashima, Mr. Akihito Miyamoto, Dr. Yan Wang, Dr. Jae Joon Kim, Dr. Chunya Wang, Dr. Chihiro Okutani, Dr. Binghao Wang, Dr. Zhi Jiang, Dr. Yasutoshi Jimbo, Dr. Hanbit Jin, Dr. Ren Shidachi, Dr. Yi-Lin Wu, Dr. Hiroaki Jinno, Mr. Ryotaro Matsukawa, Mr. Masaya Nishinaka, Mr. Md Osman Goni Nayeem, Mr. Haoyang Wang. The members of Riken team also give me a lot of precious inspiration, thanks to Dr. Kenjiro Fukuda, Dr. Wenchao Huang, Dr. Sixing Xiong, Dr. Steven Rich, Dr. Ruiyuan Liu, Dr. Kilho Yu. Many other people also helped me through, I am sorry that I cannot list all of you.

I would like to appreciate the support of my family. My parents gave me the most support of my choice, which is the most valuable fortune in my whole life.

The years at the University of Tokyo are my most important experience, from which I was learning how to think, how to identify what the most important things are, how to independently solve the problems, how to truly face the momentum deep inside me, and what my weaknesses are. I deeply appreciate all the time, the people I meet, and the things that happened here, which made my life more determined.